

FAST RESPONSE MODEL PREDICTIVE CONTROL
FOR OPEN-END WINDING INDUCTION MOTORS

by

Bohang Zhu

APPROVED BY SUPERVISORY COMMITTEE:

Kaushik Rajashekara, Chair

Babak Fahimi

Bilal Akin

Hoi Lee

Copyright © 2017

Bohang Zhu

All rights reserved

*This dissertation is dedicated to
My beloved parents*

FAST RESPONSE MODEL PREDICTIVE CONTROL
FOR OPEN-END WINDING INDUCTION MOTORS

by

BOHANG ZHU, BS, MS

DISSERTATION

Presented to the Faculty of
The University of Texas at Dallas
in Partial Fulfillment
of the Requirements
for the Degree of

DOCTOR OF PHILOSOPHY IN
ELECTRICAL ENGINEERING

THE UNIVERSITY OF TEXAS AT DALLAS

December 2017

ACKNOWLEDGMENTS

First and foremost, I would like to express my sincere gratitude towards my adviser, Professor Kaushik Rajashekara, for his constant help, availability, and efforts with the work. The confidence and dynamism with which Professor Rajashekara guided my research requires no elaboration. All I can write is that I am deeply indebted to him.

I would also like to take this opportunity to thank the respected members of the committee, Professor Babak Fahimi, Professor Bilal Akin, and Professor Hoi Lee for accepting to be members of my Supervisory Committee. I am so grateful for their time and support of my graduate studies.

I will always remember the warm moments I had with my colleagues and friends, Dr. U. R. Prasanna, Dr. Hajime Kubo, Dr. Sumit Kumar Pramanick, Dr. Xiong Li, Dr. Yijiang Jia, Dr. Robert Tang. I will always remain indebted to them for their support, cooperation, love and encouragement. Especially, I would like to stress my gratitude towards Dr. Hajime Kubo, without whose support and wide ranging expertise, it would never have been possible for me to complete this dissertation productively. I also convey my sincere thanks to Meidensha Corporation for all the support they provided throughout my research work.

My heartfelt gratitude goes out towards my loving parents and grandmother, all of whose affection, support, and continuous motivation has persistently driven me during this challenging academic voyage. I would also like to take this opportunity to express my gratefulness to my roommates, Kui Tan, and Xi Li, whose brotherly love and prayers give me great strength in my work. My acknowledgments would not be complete without a special mention of the wholehearted help and persistent prayer of all the saints in the Church in Plano and the Church in Richardson.

Above all, I would like to give my sincere gratitude to Lord Jesus Christ for giving me the opportunity, courage, patience, and the intellectual power to overcome all difficulties that I met during my graduate studies.

November 2017

FAST RESPONSE MODEL PREDICTIVE CONTROL
FOR OPEN-END WINDING INDUCTION MOTORS

Bohang Zhu, PhD
The University of Texas at Dallas, 2017

Supervising Professor: Kaushik Rajashekara, Chair

In automotive testing systems such as chassis dynamometers and engine dynamometers, induction motor is used to provide load torque and to emulate propulsion motors for electric vehicles. Fast current/torque response and low current/torque ripple are required to precisely evaluate the performance of the vehicle under test.

To reduce the torque ripple, it is necessary to operate the converters at high switching frequencies. A widely used method is to use the multilevel converters. Dynamometers fed by modular multilevel converter (MMC) or neutral point clamped (NPC) converters have been commercialized in industry. However, for MMC case, the individual modules need to be isolated using an input transformer, which is known to be costly and bulky; for NPC case, the capacitors need to be balanced, which results in increased complexity in the control. Another alternative is to use the open-end winding topology, which is obtained by disconnecting the neutral of wye-connected induction motor windings, and feeding both sides of the windings by two voltage source inverters (VSI). Due to the interleaved switching of these two inverters, the current ripple can be reduced so that the torque ripple is also reduced. In this topology, since no input transformer is required, the whole system can be cost-effective and of lower volume. And there is no need for capacitor balancing, resulting

in simplified control algorithm. However, if the two inverters share the same DC link, zero sequence current is inevitable and needs to be suppressed.

To provide fast torque response, numerous control methods have been proposed in the literature, among which field oriented control using PI controllers (FOC-PI) and direct torque control (DTC) have been successfully commercialized. In FOC-PI, the bandwidth is limited by the PI controllers, and gain scheduling is required if the operating point varies frequently. In DTC, although the structure of controller is simple, the resultant large torque ripple and steady state error limit the use of this method. As conventional control methods have several limitations, model predictive control (MPC) drew increased attention in recent years due to its intuitive concept, fast response, and easy inclusion of system constraints and nonlinearities. However, the heavy computation burden and vulnerable parameter sensitivity still remain as problems to be solved in the application of MPC.

This dissertation explores and evaluates the option of using open-end winding induction motor (OEWM) with model predictive control (MPC) to achieve fast current/torque responses. Four different MPC methods, i.e., linear predictive current control (Linear PCC), non-linear predictive current control (non-linear PCC), linear predictive torque control (linear PTC) and non-linear predictive torque control (non-linear PTC) are proposed. The proposed methods are verified in simulation and experiment. Compared with conventional control methods, the proposed methods achieve fast dynamic responses, better utilization of DC bus, and stronger zero-sequence current suppression.

Considering the heavy computation burden in conventional MPC methods, two computational efficient MPC schemes, i.e., predictive current control in A-B-C frame (PCC-ABC) and three-dimensional predictive current trajectory control (3DPCTC), are proposed. The feasibilities of proposed methods are illustrated in simulation and experiment. The results show that the proposed methods reduce the computation time by 61.05% and 64.24% respectively, and achieve stronger zero-sequence current suppression and faster dynamic responses.

To solve the parameter sensitivity issue in conventional MPC methods, a predictive current control with disturbance observer (PCC-DO) is proposed. Compared with conventional MPC methods, the proposed method can rapidly respond to sudden changes in motor parameter during steady state operation. During the transient tests, the proposed method can accurately compensate the disturbances introduced by stator resistance and magnetization inductance variations, and eliminate the resultant steady state errors.

The proposed OEWIM with MPC approach in this dissertation provides a systematic solution to achieve fast current/torque responses on electrical drives with reduced computation burden and enhanced robustness against parameter mismatches. Additionally, the proposed strategy also increases the cost-effective, fully utilizes the hardware resources, and improves the reliability of the overall system.

TABLE OF CONTENTS

ACKNOWLEDGMENTS	v
ABSTRACT	vii
LIST OF FIGURES	xiii
LIST OF TABLES	xvi
CHAPTER 1 INTRODUCTION	1
1.1 Research Background	1
1.2 Open-End Winding Machines	7
1.3 Control Methods for Induction Motor Drives	9
1.3.1 Conventional Control Methods	10
1.3.2 Model Predictive Control	13
1.4 Scope of the Dissertation	15
1.4.1 Fast Response Predictive Control for Open-End Winding Induction Motors	16
1.4.2 Computational Efficient Predictive Current Control for Open-End Wind- ing Induction Motors	16
1.4.3 Predictive Current Control with Disturbance Observer and Zero Steady State Error	17
1.5 Organization of the Dissertation	18
CHAPTER 2 OPEN-END WINDING INDUCTION MOTOR	20
2.1 Modeling of Open-End Winding Induction Motors	20
2.1.1 Electrical Model	20
2.1.2 Mechanical Model	23
2.2 PWM Strategies of Open-End Winding Induction Motors	24
2.2.1 Switching Patterns and Voltage Vectors	24
2.2.2 Zero-Sequence Current Suppression	25
2.2.3 PWM Generation of Open-End Winding Induction Motor Drives	29
2.3 Delay Compensation	31
2.4 Summary	33

CHAPTER 3	FAST RESPONSE PREDICTIVE CONTROL FOR OPEN-END WINDING INDUCTION MOTORS	35
3.1	Introduction	35
3.2	Theoretical Derivation	37
3.2.1	Predictive Current Control (PCC)	38
3.2.2	Predictive Torque Control (PTC)	40
3.3	Simulation Results	43
3.3.1	Transient State Operation	44
3.3.2	Steady State Operation	45
3.4	Experimental Results	46
3.4.1	Steady State Operation	50
3.4.2	Transient State Operation	55
3.5	Summary	57
CHAPTER 4	COMPUTATIONALLY EFFICIENT PREDICTIVE CURRENT CONTROL FOR OPEN-END WINDING INDUCTION MOTORS	59
4.1	Introduction	59
4.2	Predictive Current Control in A-B-C Frame (PCC-ABC)	61
4.2.1	System Model	61
4.2.2	Flux Estimation	63
4.2.3	Conventional PCC	63
4.2.4	Proposed PCC-ABC	65
4.2.5	Simulation Results	67
4.2.6	Experimental Results	68
4.3	Three-Dimensional Predictive Current Trajectory Control (3DPCTC)	74
4.3.1	Methodology	74
4.3.2	Experimental Results	77
4.4	Summary	81
CHAPTER 5	PREDICTIVE CURRENT CONTROL WITH DISTURBANCE OBSERVER AND ZERO STEADY STATE ERROR	83
5.1	Introduction	83

5.2	Indirect Field Oriented Control (IFOC)	85
5.3	Parameter Sensitivity Analysis	89
5.3.1	Parameter Sensitivity of Electrical Torque	89
5.3.2	Parameter Sensitivity of Rotor Flux Linkage	91
5.4	Proposed Deadbeat Predictive Current Control with Disturbance Observer (PCC-DO)	92
5.5	Design of Disturbance Observer	93
5.6	Stability Analysis of the Controller	98
5.7	Simulation Results	99
5.7.1	Steady State Performance	100
5.7.2	Transient State Performance	103
5.8	Summary	106
CHAPTER 6 CONCLUSIONS AND RECOMMENDATIONS FOR FUTURE WORK		108
6.1	Contributions of the Work	108
6.2	Recommendations for Future Work	109
REFERENCES		110
BIOGRAPHICAL SKETCH		119
CURRICULUM VITAE		

LIST OF FIGURES

1.1	Typical Setup of a Dynamometer System	2
1.2	Open-end Winding Configuration with Two Three-phase Inverters	8
1.3	Induction Motor Fed by Three Independent Single-phase Bridge Inverters	9
1.4	Open-end Winding Configuration with Two Isolated DC-links	9
1.5	Block Diagram of a Control System	11
1.6	FOC with PI Controller for Induction Motors	11
1.7	DTC with Hysteresis Controller for Induction Motors	13
1.8	Block Diagram of the Proposed MPC System	14
2.1	Open-End Winding Induction Motor Drives	21
2.2	Switching States of A Two-Level Inverter	25
2.3	Switching States of Two Inverters in Open-End Winding Induction Motors	27
2.4	2-D View of Voltage Vectors of Open-End Winding Induction Motors	28
2.5	3-D View of Voltage Vectors of Open-End Winding Induction Motors	29
2.6	Magnitude of Combined Voltage Vector under Different Phase Shift	30
2.7	Reference Signal Generation of SVPWM with 120° Phase Difference	32
2.8	Control Sequence of PTC for Open-End Winding Induction Motors	32
2.9	Flowchart of PTC with Delay Compensation for Open-End Winding Induction Motors	34
3.1	MPC Methods for Open-End Winding Induction Motor Drives	36
3.2	Open-end Winding Induction Motor Drives	37
3.3	Block Diagram of the Open-End Winding Induction Motor Drive	38
3.4	Block Diagram of Inner Controller Using Linear PCC	40
3.5	Block Diagram of Inner Controller Using Non-Linear PCC	41
3.6	Block Diagram of Inner Controller Using Linear PTC	42
3.7	Block Diagram of Inner Controller Using Non-Linear PTC	43
3.8	Torque Responses in Simulation	45
3.9	Frequency Responses in Simulation	46
3.10	Steady State Responses in Simulation (a) Linear PCC (b) Linear PTC (c) Non-Linear PCC (d) Non-Linear PTC	47

3.11	Block Diagram of the Experimental System	48
3.12	Experimental Setup (a) System Overview (b) Controller Board	49
3.13	Steady State responses in Experiment (a) Three-Phase Currents at 0.3 pu speed under no load (b) Zero-Sequence Current at 0.3 pu speed under no load (c) Three-Phase Currents at 1.0 pu speed under 0.8 pu load (d) Zero-Sequence Current at 1.0 pu speed under 0.8 pu load	51
3.14	FFT Spectrum of One Phase Current (a) Linear PCC (b) Non-Linear PCC (c) Linear PTC (d) Non-Linear PTC	53
3.15	Voltage Vector Selection in MPC Methods	54
3.16	Transient State A Phase Current in Experiment	56
3.17	Transient State Zero-Sequence Current in Experiment	57
4.1	An Open-End Winding Induction Motor Drive	62
4.2	Block Diagram of PCC-ABC for OEWIM	68
4.3	Simulation Transient Responses of PCC and PCC-ABC (a) Three-Phase Currents of PCC (b) Cost of PCC (c) Three-Phase Currents of PCC-ABC (d) Cost of PCC-ABC	69
4.4	Experimental System Setup (a) Block Diagram (b) System Overview	70
4.5	Experiment: Steady State Performance at 447 rpm with No Load	71
4.6	Experiment: Steady State Performance at 1470 rpm with No Load	72
4.7	Experiment: Steady State Performance at 1470 rpm with 0.8 pu Load	73
4.8	Experiment: A Phase Current during Speed Reversal	73
4.9	(a) Voltage Vectors in Two Dimensional Plane (b) Voltage Vectors in Three-Dimensional Space	75
4.10	Voltage Vectors in: (a) Inner Triangle (b) Intermediate Triangle (c) Outer Triangle	76
4.11	Block Diagram of the Controller	77
4.12	Steady State Response at 0.3pu Speed with No Load	79
4.13	Steady State Response at 1.0 pu Speed with 0.8 pu Load	80
4.14	Transient State Response 0.2 pu to 1.0 pu Speed Change	80
4.15	Transient State Response 0.8pu Torque Step at 1.0 pu Speed	81
5.1	An Open-End Winding Induction Motor Drive	85
5.2	IFOC schematic with Slip Calculation 1	88

5.3	IFOC schematic with Slip Calculation 2	88
5.4	Relationship between Flux-Producing Current and Torque-Producing Current .	89
5.5	Block Diagram of Proposed Linear Predictive Current Control with Disturbance Observer	94
5.6	Proposed Sliding-Mode Disturbance Observer in d-axis	97
5.7	Proposed Sliding-Mode Disturbance Observer in q-axis	98
5.8	Steady-State Response with No Disturbance (a) Conventional Linear PCC (b) Proposed PCC-DO	100
5.9	Steady-State Response with Disturbance $R_s = 0.5R_s^*$ (a) Conventional Linear PCC (b) Proposed PCC-DO	101
5.10	Steady-State Response with Disturbance $R_s = 2R_s^*$ (a) Conventional Linear PCC (b) Proposed PCC-DO	101
5.11	Steady-State Response with Disturbance $R_s = 5R_s^*$ (a) Conventional Linear PCC (b) Proposed PCC-DO	102
5.12	Steady-State Response with Disturbance $L_m = 0.5L_m^*$ (a) Conventional Linear PCC (b) Proposed PCC-DO	102
5.13	Steady-State Response with Disturbance $L_m = 1.5L_m^*$ (a) Conventional Linear PCC (b) Proposed PCC-DO	103
5.14	Transient Response with No Disturbance (a) Conventional Linear PCC (b) Proposed PCC-DO	104
5.15	Transient Response with Disturbance $R_s = 0.1R_s^*$ (a) Conventional Linear PCC (b) Proposed PCC-DO	104
5.16	Transient Response with Disturbance $R_s = 10R_s^*$ (a) Conventional Linear PCC (b) Proposed PCC-DO	105
5.17	Transient Response with Disturbance $L_m = 0.5L_m^*$ (a) Conventional Linear PCC (b) Proposed PCC-DO	105
5.18	Transient Response with Disturbance $L_m = 1.5L_m^*$ (a) Conventional Linear PCC (b) Proposed PCC-DO	106

LIST OF TABLES

1.1	Comparison between Dynamometers	3
1.2	Comparison of Requirements of Dynamometers in Transient Tests	4
1.3	Comparison of Possible Techniques	6
2.1	Switching States and Voltage Vectors in Open-End Winding Induction Motors .	26
3.1	Motor Ratings and Parameters	44
3.2	Inverter and Motor Specifications	49
3.3	Computation Time Comparison	50
3.4	Steady State Current THDs	52
4.1	Motor Ratings and Parameters	67
4.2	Inverter and Motor Specifications	68
4.3	Computation Time Comparison	70
4.4	Computation Time Comparison	78
5.1	Motor Ratings and Parameters	99

CHAPTER 1

INTRODUCTION

1.1 Research Background

The dynamometer is a device for measuring torque, force and power. One of the earliest dynamometers can be dated back to 1821, when Gaspard de Prony invented the Prony brake, in which a mechanical friction brake is pressed against the flywheel mounted on the engine shaft, and the braking force is measured by adding weights on the weighting pan [1]. During the past 200 years, different dynamometers have been developed, and the technique of measuring torque and power has advanced significantly.

In the automotive industry, dynamometers play an important role in both manufacturing process and vehicle research and development. In addition to conventional tests of determining the torque or power characteristics of the unit under test (UUT), dynamometers are also employed in many other tests by different groups of users. For normal users, dynamometers are used in standard emission tests to provide simulated road loading. For automobile manufacturers, dynamometers are used in engine or powertrain development, engine management controller calibration, and evaluations of the transient and steady state responses of the vehicles or components. For researchers and developers, dynamometers are applied to improve fuel economy of combustion engines, to control noise and emission, and to experiment with new concepts for electrical vehicles.

The composition of a typical dynamometer system usually includes an absorption unit, a sensor/measuring unit, and a control unit, as shown in Figure 1.1. The UUT either can be engine, powertrain or vehicle components, and it is coupled to the absorption unit, which allows the UUT to move as required. The sensing and measurement part often includes a torque meter and a tachometer. The controller collects the data and gives commands to the absorption unit and the UUT.

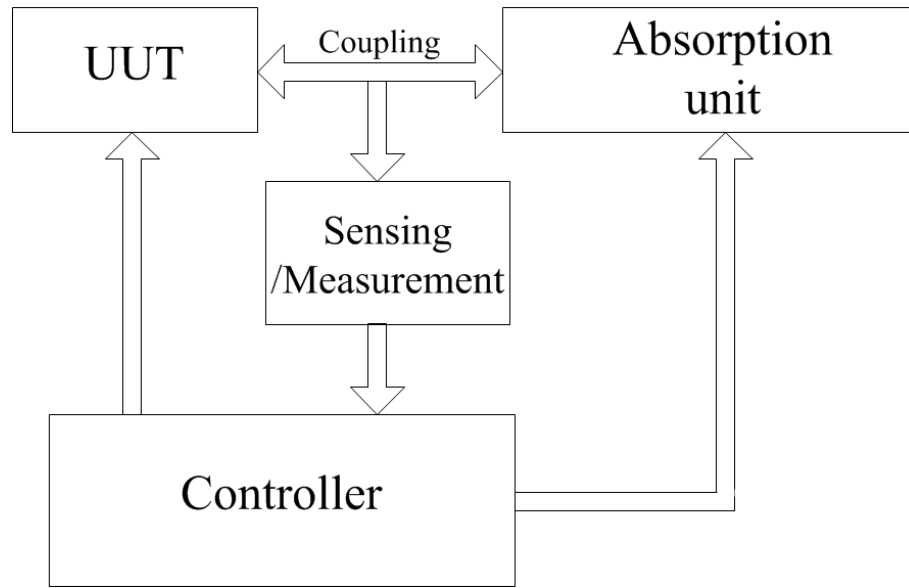


Figure 1.1: Typical Setup of a Dynamometer System

Based on whether the dynamometers can absorb or provide power, they can be classified as the following types:

- Absorption-only
- Absorption/motoring
- Compound

By definition, the absorption-only dynamometers can only absorb power from the UUT, hence it is of the simplest structure, least cost, and a variety of sizes/power ratings. Most of the dynamometers in the market are absorption-only. The absorption/motoring dynamometer is an adjustable speed drive, either DC motor or AC motor can be used. And it can provide almost the same motoring power as the absorbing power. By controlling the motor, the dynamometer can be manipulated over a wide operation range. However, the cost of the dynamometer is the highest since large power motor drives are expensive. The compound dynamometer is a compromise of the previous two types. It usually consists of a larger absorption unit and a smaller motoring unit. Comparing to the absorption/motoring type, the motor used in a compound dynamometer is smaller, hence the price of the whole

Table 1.1: Comparison between Dynamometers

Type	Absorption Only	Absorption/Motoring	Compound
Function	Absorb	Absorb/Drive	Absorb/Drive
Absorption			
Power	Very High	High	Very High
Motoring			
Power	None	High	Low
Cost	Low	High	Medium

system is lower. But due to the coupling between the absorption and motoring units, the system complexity is increased. Table 1.1 gives a comparison among these three types of dynamometers.

Depending on the functions of the dynamometers, different tests can be performed to examine the characteristics of the UUT. Basically, there are three types of tests, i.e., steady state test, sweep test, and transient test. In a steady state test, the UUT is held on a commanded speed for a desired amount of time, during which different loads are provided through the absorption unit. In a sweep test, a constant load is applied on the UUT, and the speed of the UUT is changed within a specified range. In a transient test, the power and speed of UUT are varied throughout the test cycle. The dynamometer needs to have fast response to meet the different requirements of the test cycles.

Among the dynamometers being compared, absorption/motoring dynamometer is most used by manufacturers and research facilities since it has excellent dynamic performance. Hence the absorption/motoring dynamometer is considered in the dissertation. In the rest of the dissertation, the absorption/motoring dynamometer is referred to as dynamometer for simplicity.

As there are variant transient tests for different purposes, dynamometers need to meet different requirements to fulfill the testing purpose. For instance, in a rear-wheel-drive (RWD) drivetrain test, a dynamometer needs to emulate the function of a combustion engine. This requires the dynamometer to have fast dynamic torque response and accurate speed control. Also in a RWD

Table 1.2: Comparison of Requirements of Dynamometers in Transient Tests

Function	Requirements
Provide load torque in engine test	Output load torque at engine speed No steady state error (600 Nm at 7000-9000 RPM)
Emulate ignition torque of combustion engine	Fast response current/torque control (bandwidth > 1500 Hz)
Emulate motors in EV	Fast response current/torque control (bandwidth > 1500 Hz) Output power at EV motor speed (450kW at 18000-22000 RPM)
Emulate low inertia wheel load	Low inertia (0.1 kgm^2)
Act as prime mover in component test	Low torque ripple at low speed (< 0.1 Nm at 10 RPM)

drivetrain test, a dyno can be used to emulate the wheel load to the drivetrain, which requires the dyno to emulate the low inertia of a actual wheel. In the electric vehicle (EV) development process, a dyno is used to emulate the EV motor, which requires the dyno to operate at high speed (>20k RPM) and can simulate the high frequency cogging torque. All these requirements result in different control strategies for the motors used in the dyno. Table 1.2 gives a comparison of the requirements of the dynos under different tests.

It can be observed from Table 1.2 that the fast response speed is an important requirement in automotive developing and testing process. Generally, system response speed can be increased by using higher switching frequency or using more complex controllers. By increasing the switching frequency, the number of manipulations on the motor currents can be increased. On the other hand, advanced and efficient control algorithms can be developed to expand the controller bandwidth.

To increase the switching frequency of the power converters, multi-level converters can be used. In [2], a 5-level inverter with reduced number of switches is proposed; in [3], a dual 7-level voltage supply is presented; and in [4], a 9-level topology is illustrated. Also,

[5–7] describe the application of modular multilevel converters (MMC) on grid-connected photovoltaic generation and medium voltage drive. Generally, the multilevel converters can generate $n - 1$ times carrier frequency with n voltage levels across the phase winding, resulting in less total harmonic distortion (THD). However, with the increase in the voltage levels, the number of switches as well as the switching losses also increase. And more complex control algorithm and PWM strategy are required to drive the multilevel converter. In the MMC case, input transformers are required to provide isolation to each individual modular converter. The transformers add additional volume and cost to the system, which make it difficult to fit in the vehicle.

Another option to increase the switching frequency is to use SiC/GaN devices. Converters made with SiC/GaN devices have been reported in [8–12]. Compared with IGBT converters, whose preferred switching frequency is less than 20kHz [9], the SiC/GaN converters can reach the maximum switching frequency at 200 kHz with negligible switching losses [9]. Although SiC/GaN converters are ideal for electrical vehicles, the primary limitation for universalizing the SiC/GaN devices is the price. The cost of SiC/GaN devices is still not comparable to the conventional IGBT switches. Another problem of high switching frequency is the EMI issue. When the switching frequency exceeds 100 kHz, the EMI of the power converters can have significant impact on low-voltage controllers. Additional EMI filters or suppression methods are required for high-switching-frequency converters. All these aspects make the SiC/GaN converters still not being widely used in electric vehicles.

Apart from aforementioned methods, the open-end winding topology can also effectively increase the switching frequency by interleaving the switching of the converters, the switching frequency of the voltage across the windings is doubled.

As mentioned earlier, advanced control algorithms can also be applied to further expand the controller bandwidth. Conventional proportional-integral (PI) control has been proven to have good response speed with almost zero steady state error, and has been widely applied

Table 1.3: Comparison of Possible Techniques

Increasing Switching Frequency		
Technique	Advantages	Disadvantages
Multilevel converters	<ul style="list-style-type: none"> ● (n-1) times carrier frequency with n voltage levels 	<ul style="list-style-type: none"> ● Have costly and bulky input transformer ● System complexity
Open-end winding	<ul style="list-style-type: none"> ● 2 times carrier frequency ● Simple structure 	<ul style="list-style-type: none"> ● Zero-sequence current may flow
SiC/GaN converter	<ul style="list-style-type: none"> ● Can operate at high switching frequency ● High thermal tolerance 	<ul style="list-style-type: none"> ● Expensive
Increasing Controller Bandwidth		
PI with gain scheduling	<ul style="list-style-type: none"> ● No steady error ● No observer 	<ul style="list-style-type: none"> ● System Complexity ● Reliability issues
Hysteresis with self tuning	<ul style="list-style-type: none"> ● Simple structure ● Parameter insensitive 	<ul style="list-style-type: none"> ● Variable switching frequency ● Large current/torque ripples
Fuzzy Logic	<ul style="list-style-type: none"> ● Small calculation effort ● Simple structure 	<ul style="list-style-type: none"> ● Variable switching frequency ● Need large memory
Model predictive control	<ul style="list-style-type: none"> ● Operate at system physical limit ● Robust to disturbances 	<ul style="list-style-type: none"> ● Large computation effort ● Steady state error ● Parameter sensitive

in industry. However, PI controller struggles when the operating point changes and when the system has multiple inputs and multiple outputs (MIMO). PI gain scheduling have been proposed in [13–15] to address the operating point changing problem. But for MIMO system, decoupling and system decomposition are still required, which increase the complexity of the controller. Hysteresis control can also provide fast responses, and it is simple structured and parameter insensitive [16]. But the main drawbacks are the variable switching frequency and large current/torque ripples [17]. Another fast response control method is fuzzy logic control [18–20]. It is based on a look-up table, which results in small calculation effort and simple controller structure. As a trade-off, large memory is required and the switching

frequency is not constant. In recent years, model predictive control (MPC) has drawn researchers' attention. Compared with the other methods, MPC can handle various system non-linearities and can be applied to MIMO systems. Since the plant model is integrated in the controller, the plant can also be manipulated at the system physical limits. However, large computation effort is introduced in the prediction process, and the controller heavily relies on the precision of the plant model parameters.

With all the hardware and software methods mentioned above, the advantages and disadvantages of possible techniques are compared in Table 1.3. In consideration of the cost-effectiveness of the over-all system, this dissertation investigates and evaluates the option of using open-end winding induction motor (OEWM) with model predictive control (MPC) to reach fast current/torque response. Considering the disadvantages of the setup mentioned in Table 1.3, different control methods have been proposed to compensate and improve the system performance, which are discussed in Chapters 3 to 5 of this dissertation.

1.2 Open-End Winding Machines

Open-end winding electric machine is also known as split phase machine or separately fed machine, obtained by removing the neutral point of the stator windings of a conventional electric machine. These machines are being examined for various applications such as propulsion motor in electric and hybrid vehicles, fault tolerant generator in aircraft systems, ship propulsion, and industrial drive systems. Compared to neutral connected motor, the open-end winding motors have the following advantages [21, 22].

- No pole switching constraint.
- In case of open or short circuit in one of the phases, the magnetomotive force (MMF) can be maintained by using the remaining two phases. This feature can be extended to multi-phase machines.

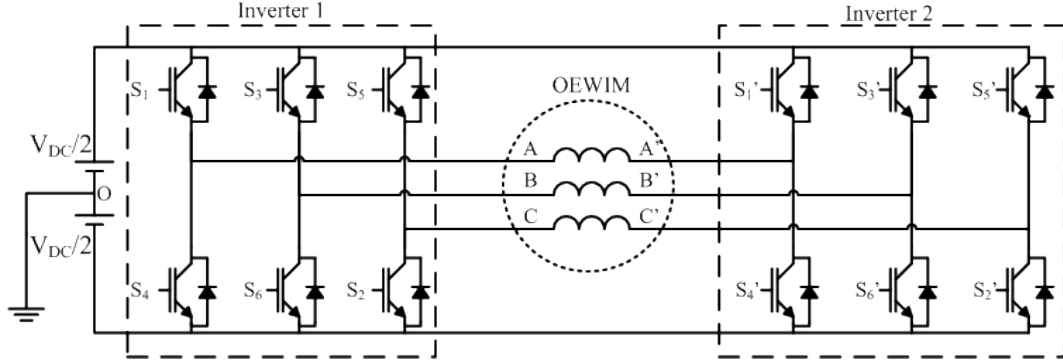


Figure 1.2: Open-end Winding Configuration with Two Three-phase Inverters

- Independent control of switches in each phase, which brings independent control of the stator current.
- Reduced power rating of individual switch: Feeding power from both ends of the winding by DC source, the switches in each phase bear half the power compared to that in neutral-connected configuration.
- Reduction in switching loss and total harmonic distortion (THD).

The open-end winding three-phase induction motor controlled from two two-level three-phase inverters is shown in Figure 1.2. Instead of calling it as an open-end winding machine, it is also referred to as separately-fed machine, using three H-bridge converters, as shown in Figure 1.3 [21, 22]. The strategy in these papers is to overcome the pole switching constraint of three-phase bridge inverters, where the number of switching states is limited to eight including two zero switching states. However, disadvantages including more switching devices and more complicated control also give the open-end winding motor some restraints. Besides, zero sequence voltages may appear which may also lead to additional losses.

Based on the number of isolated DC links, two possible topologies are presented in the literature. Topologies shown in Figure 1.2 and Figure 1.3 use only one DC-link and it can be represented either as three single-phase H-bridges or as two three-phase inverters. Another modified topology is shown in Figure 1.4, which uses two isolated DC sources to avoid the zero-sequence currents [23, 24]. A scheme using two isolated DC sources fed from each end

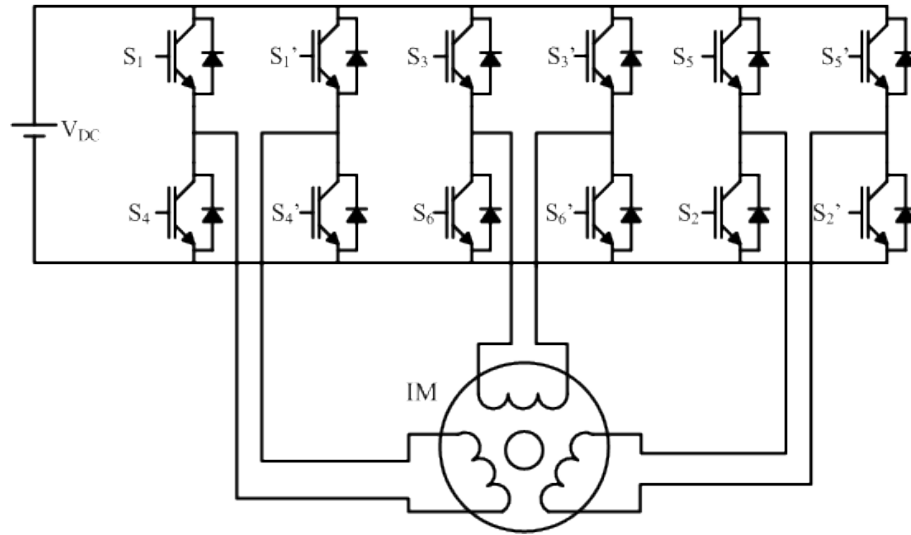


Figure 1.3: Induction Motor Fed by Three Independent Single-phase Bridge Inverters

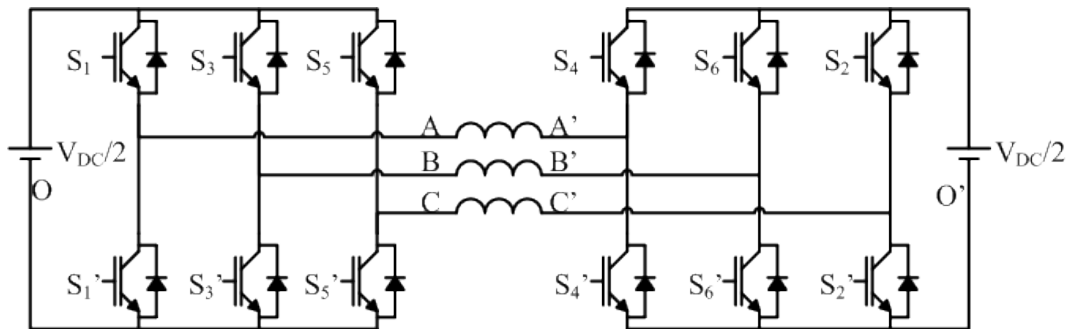


Figure 1.4: Open-end Winding Configuration with Two Isolated DC-links

with zero common mode voltage is illustrated in [24]. With only one DC source, a PWM scheme with common mode elimination is presented in [25].

As isolated power sources are limited in many applications, this dissertation focuses on the configuration with only one DC voltage source, to compare existing and investigate new control strategies for the open-end winding induction motor drive.

1.3 Control Methods for Induction Motor Drives

Conventional control methods such as proportional-integral (PI) control have been widely applied for controlling electric drive systems [26]. These control methods are originally

implemented using analog electronics. With the technical advancement of the semiconductor devices and the progression in control theory, several improvements have been made to the control methods for drive systems.

First, the implementation of control schemes in digital domain instead of analog circuits is the most notable transition in last 15 to 20 years. Due to the digital implementation, proper data sampling and approximation schemes are required to effectively represent the behavior of the continuous-time domain controllers. Secondly, non-linear control methods are being increasingly investigated and evaluated for drive applications. Compared with linear control methods which are mainly derived on single-input-single-output (SISO) systems, non-linear schemes can be applied on multi-input-multi-output (MIMO) systems. In addition, non-linear methods have better dynamics performances, and can include system constraints more effectively compared with linear counterparts. Moreover, advanced and complex control methods such as predictive control and artificial intelligence have also been increasingly explored by researchers. Wider operation range and better robustness against disturbances have been achieved by these control methods. Among the many control methods, model predictive control has gained increased attention due to its intuitive concept, fast dynamic response, and immunity to various disturbances. In the following section, conventional control methods and model predictive control methods are introduced, and the advancement of model predictive control on motor drives is illustrated.

1.3.1 Conventional Control Methods

A conventional control system consists of two parts, the plant and the controller, as shown in Figure 1.5. The plant can represent either a physical plant or an industrial process. The control problem is to manipulate the plant input u such that the plant is stabilized, the output y follows a given reference r , and the desired performance can be achieved despite disturbances and uncertainties. The conventional control methods for induction motor drives

constraints. However, a linearization process is required to provide the linearity for deriving the system transfer function. Therefore, the conventional PI control meets its limitation if the system is multi-input-multi-output (MIMO), non-linear, or constrained.

Some solutions have been proposed to overcome the above limitations. For a MIMO system, decomposition can be performed so that the system can be regarded as several SISO sub-systems. A well-known technique to apply PI control on MIMO system is to use cascaded control loops. As shown in Figure 1.6, the system consists of an outer speed loop and an inner current loop. Usually the sampling frequency of the speed loop is much lower than that of the current loop. Regarding the non-linear dynamics, the controller can be designed for different operating points, which require linearizations for each of them. Hence a gain-scheduling can be applied to improve the non-linear dynamic responses. To address the system constraints, some non-linear regulators such as output saturation can be used. As a result, high engineering efforts and stability problems occur, and the system often comes up with limited performance [27–29].

DTC with Hysteresis Controller

Figure 1.7 presents the block diagram of the DTC with hysteresis controller. The motor stator currents i_a, i_b and the motor mechanical angular speed ω_r are measured. By using the motor voltage model, the electrical torque T_e and the stator flux vector magnitude ψ_s are estimated. The errors between estimated variables and the references are passed through the hysteresis controllers. The outputs of the hysteresis controllers are indexed in a look-up table to generate the gating signals.

In the hysteresis control, a hysteresis band is defined, the control variable is maintained within the defined hysteresis boundary by changing the switching states of the converters. This method is conceptually simple and easy to implemented. Fast dynamic response can also be achieved if the hysteresis band is properly selected. However, there are two primary

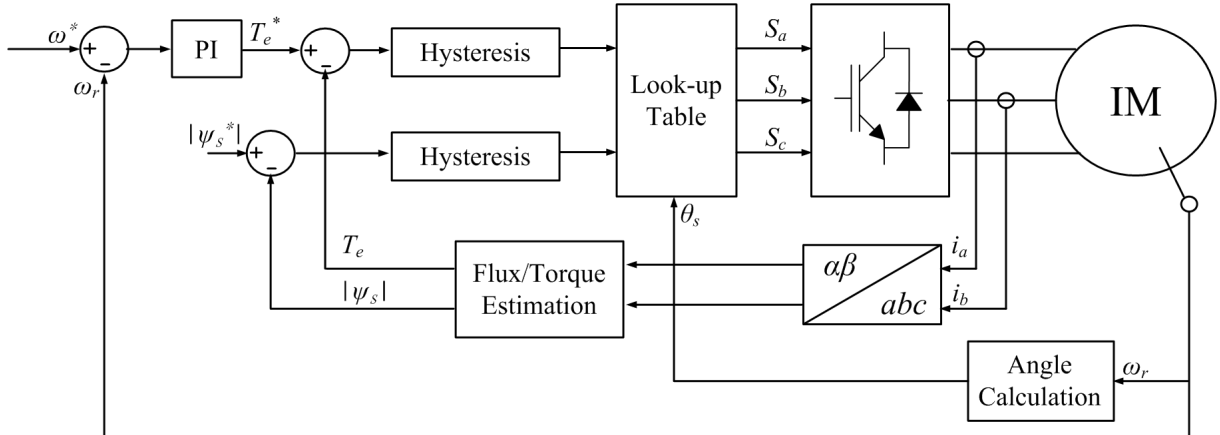


Figure 1.7: DTC with Hysteresis Controller for Induction Motors

drawbacks in this control scheme. One is that the switching frequency changes according to the hysteresis bandwidth, load parameters, and operating conditions. The variable switching frequency may cause resonance problems. The other problem is that the control method heavily relies on a high sampling frequency to maintain the control variables within the hysteresis band and to reduce the ripples. With such a high sampling frequency, the switching loss of the converter is not negligible.

1.3.2 Model Predictive Control

As conventional control methods have several limitations, model predictive control (MPC) drew increased attention in industrial manufactures [30]. MPC is firstly introduced in the 1960s as an application of optimal control theory. In late 1970s, researchers began to apply MPC on industrial applications [31]. The first application of MPC is reported in chemical process industry, where the time constant is long enough to complete all the required calculations. In power electronic applications, the earliest utilization of MPC can be dated back to 1980s where a high-power system with lower switching frequency is considered [32]. Due to the long calculation time required in the control algorithm, higher switching frequencies could not be achieved at that time. However, with the development of fast and powerful microprocessors, interests in applying MPC to power electronics have increased during the last

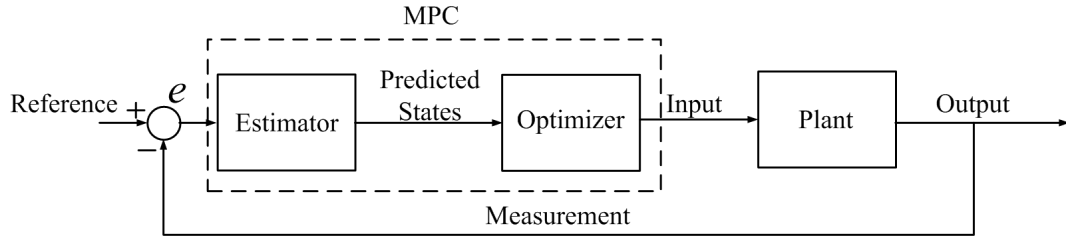


Figure 1.8: Block Diagram of the Proposed MPC System

decade. Compared with conventional control methods, MPC has the following advantages:

- Intuitive concept and straightforward derivation.
- Fast dynamic response.
- Superior suitability to MIMO systems.
- Easy inclusion of system constraints and non-linearities.
- Broad adaptation to a variety of systems.

Unlike the individual control method mentioned in Section 1.3.1, MPC summarizes a wide family of controllers [33]. In MPC, the mathematical model of the plant is used to predict the future behaviors of the plant. According to the predicted states of the plant, the most optimal actuation is selected to control the plant. Generally a MPC method consists of two parts, an estimator, which predicts the plant's future behavior, and an optimizer, which determines the optimal actuation. A typical MPC block diagram is shown in Figure 1.8.

Depending on whether an exact solution is calculated or not, the MPC methods can be categorized into two types, linear MPC and non-linear MPC [30]. The former one needs to calculate an exact solution to control the plant. The calculated solution is applied to the plant through a modulator, hence this method is also referred to as indirect MPC [34, 35]. The latter one does not come up with an exact solution, it integrates the plant into the controller and considers all the possible actuations. By using a cost function, the optimal actuation is directly applied on the plant. Therefore, this method is also named direct MPC [34, 35].

The MPC methods can be also categorized as single-step MPC and multi-step MPC depending on the prediction horizon. In single-step MPC, the prediction horizon is 1. All linear MPC methods fall into this category. In multi-step MPC, the prediction horizon can be more than 1. A multi-step MPC method with prediction horizon of 10 is reported in [36]. As the prediction horizon increases, the calculation time grows exponentially [36], hence a much longer sampling period is required in multi-step MPC than in single-step MPC. Usually, multi-step MPC is used in applications on which switching frequency is low enough to complete all the necessary calculations [37]. In automotive testing systems such as in dynamometers, the typical switching frequency is in the range of 5000 Hz to 10000 Hz, the sampling period is not sufficient for multi-step prediction. Hence in this dissertation, only single-step MPC methods are studied.

1.4 Scope of the Dissertation

The focus of this dissertation is to develop fast current/torque response control methods for the open-end winding induction motor drive with two two-level three-phase inverters sharing one DC-link. The following items are investigated, and improved control strategies are proposed.

1. Fast response predictive control for open-end winding induction motor
2. Computational efficient predictive current control for open-end winding induction motor
3. Predictive current control with disturbance observer and zero steady state error

1.4.1 Fast Response Predictive Control for Open-End Winding Induction Motors

As reviewed in Section 1.3.2, successful applications of model predictive control on conventional wye-connected induction motor drive have been presented in literatures [30, 34, 35]. However, for open-end winding configuration considered in this dissertation, no such research has been reported yet.

The focus of this work is to develop predictive control methods for open-end winding induction motor drive, so that fast current/torque response can be achieved as well as the zero-sequence current can be suppressed. Four different model predictive control methods are proposed, i.e., linear predictive current control, non-linear predictive current control, linear predictive torque control, and non-linear predictive torque control. The development process of the control methods consists of several steps. First, a full-order mathematical model of the open-end winding induction motor is derived. Based on the model, an accurate flux observer is designed to provide estimation of the rotor and stator flux. A cost-function based optimizer is devised so that the optimal actuation can be obtained. Some practical issues such as dead-time effect and digital calculation delay are also considered, compensators are designed to address these problems. The proposed methods are simulated in Matlab environment. An experimental system is also built to verify the proposed methods.

1.4.2 Computational Efficient Predictive Current Control for Open-End Winding Induction Motors

In conventional induction motor drive fed by two-level inverters, 8 switching states are mapped onto 7 voltage vectors. Conventional predictive control methods need to evaluate these 7 voltage vectors to find out the optimal actuation within each sampling period. For the case in this dissertation, two two-level inverters are used. A total of 64 switching

states are mapped onto 27 voltage vectors. Due to the increase of the number of voltage vectors to be evaluated, the calculation time increases exponentially. As a result, the sampling frequency is limited. As lower sampling frequency leads to larger current total harmonic distortion (THD) and slower dynamic responses, a calculation-effective predictive control method is urged to improve the performances of the system.

The focus of this work is to design computational effective model predictive control methods so that the controller can operate in higher sampling frequency and faster dynamic response can be achieved. Two predictive current control methods are proposed. The first method is derived in A-B-C frame, and three-phase independent control is achieved by treating the zero-sequence component as a feed-forward term. The second method investigates the current trajectory generated by each voltage vector. An intelligent sorting algorithm is proposed to reduce the number of voltage vector to be evaluated. Both methods have been compared with conventional predictive current control method in simulation and experiment.

1.4.3 Predictive Current Control with Disturbance Observer and Zero Steady State Error

Unlike the conventional PI control method, in which integrators are used to eliminate the steady state errors, model predictive control uses machine parameters to estimate and predict state variables. As the machine parameters change according to different working environment, the inaccurate calculation leads to increased steady state error and deteriorated dynamic response. A robust control method is demanded to provide satisfactory steady state and dynamic responses under different parameter mismatch situations.

The focus of this work is to arise a disturbance-resistant control method so that the controller can maintain fast dynamic response as well as zero steady state error. A deadbeat current control method with disturbance observer is proposed. Based on the sensitivity analysis of the open-end winding induction motor, a sliding mode observer is derived to

compensate the parameter mismatch and to predict the future state of the motor. The proposed controller is tested under different parameter mismatch situations and compared with conventional deadbeat control in simulations and experiments.

1.5 Organization of the Dissertation

This dissertation is organized as follows:

Chapter 2 illustrates the operating principles of the open-end winding induction motor. The electrical model of open-end winding induction motor with zero-sequence components is derived. Different possible PWM methods for open-end winding configuration are studied. The delay issue resulted from digital calculation and power converters is also analyzed.

Chapter 3 presents the fast response predictive control strategies for open-end winding induction motor drive. Four different control methods, i.e., linear predictive current control, non-linear predictive current control, linear predictive torque control, and non-linear predictive torque control are investigated. Detailed derivation is given for each control method. Simulations and experiments are executed to validate the feasibility of proposed methods. Both transient and steady state performances are examined and analyzed. A comparison is made across the four methods.

Chapter 4 provides two computational efficient predictive control methods. The deficiencies of conventional model predictive control methods are explained. A predictive current control method in A-B-C frame (PCC-ABC) and a three-dimensional predictive current trajectory control (3DPCTC) method are proposed. Theoretical analysis is given for both methods. A conventional predictive current control method is also implemented to provide comparison to the proposed methods. Simulations and experiments are done to prove the effectiveness of proposed methods as compared to the conventional method.

Chapter 5 introduces a predictive current control with disturbance observer and zero-steady state error. A parameter sensitivity analysis is given for the open-end winding induc-

tion motor. To increase the robustness of the controller against the parameter mismatch, a sliding-mode disturbance observer with zero-sequence current suppression is proposed. The stability of proposed observer is analyzed. Simulations are performed under different parameter mismatch situations. A detailed analysis of the simulation results are presented.

Chapter 6 describes the salient features of the proposed model predictive controls on open-end winding induction motor drive. The key contributions of the dissertation are summarized, a conclusion is given on proposed methods. Based on the current work, a few recommendations for future work are also presented.

CHAPTER 2

OPEN-END WINDING INDUCTION MOTORS -

CHARACTERISTICS AND MATHEMATICAL MODELING

Open-end winding induction motor is obtained by disconnecting the neutral point of a conventional wye-connected machine and feeding both ends by either two three-phase inverters or three H-bridge inverters. This dissertation investigates the open-end winding induction motor fed by two two-level three-phase voltage source inverters sharing one DC link. As a result, a common mode path is created between the two inverters and the zero-sequence current can flow. In this chapter, the electrical and mechanical model of the open-end winding induction motor is derived, the corresponding PWM strategies are investigated, and the delay issue resulted from digital calculation and power converters is studied.

2.1 Modeling of Open-End Winding Induction Motors

Due to the presence of zero-sequence current, the motor windings can no longer be considered as three-phase balanced. A zero-sequence component must be included in the modeling. This section describes the modeling of open-end winding induction motor with zero-sequence components.

2.1.1 Electrical Model

The circuit diagram of the open-end winding induction motor drive is shown in Figure 2.1. The stator and rotor state-space equation in A-B-C frame can be expressed as:

$$\begin{bmatrix} \mathbf{v}_{sabc} \\ \mathbf{0} \end{bmatrix} = \begin{bmatrix} \mathbf{r}_s \\ \mathbf{r}_r \end{bmatrix} \begin{bmatrix} \mathbf{i}_{sabc} \\ \mathbf{i}_{rabc} \end{bmatrix} + p \begin{bmatrix} \boldsymbol{\psi}_{sabc} \\ \boldsymbol{\psi}_{rabc} \end{bmatrix} \quad (2.1)$$

Where \mathbf{v}_{sabc} , \mathbf{v}_{rabc} are stator and rotor voltage vectors, \mathbf{i}_{sabc} , \mathbf{i}_{rabc} are stator and rotor current vectors, and $\boldsymbol{\psi}_{sabc}$, $\boldsymbol{\psi}_{rabc}$ are stator and rotor flux vectors. \mathbf{r}_s and \mathbf{r}_r are stator and

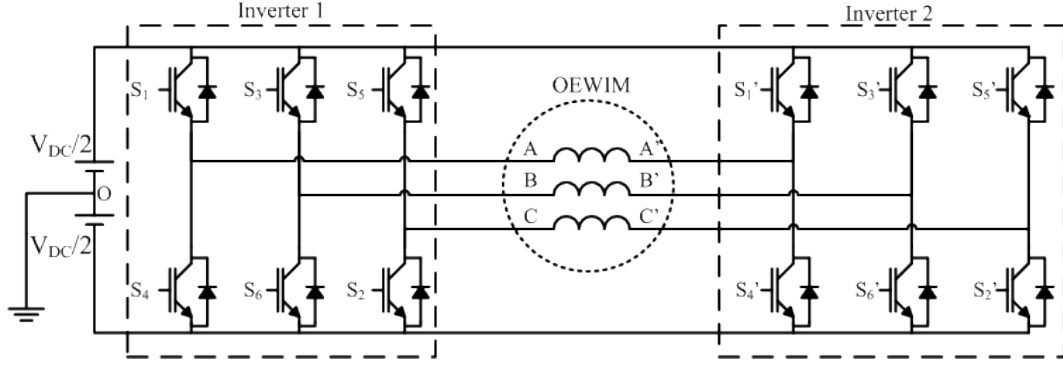


Figure 2.1: Open-End Winding Induction Motor Drives

rotor resistance matrices. p is the derivative operator.

$$\mathbf{v}_{sabc} = \begin{bmatrix} v_a \\ v_b \\ v_c \end{bmatrix}, \mathbf{i}_{sabc} = \begin{bmatrix} i_a \\ i_b \\ i_c \end{bmatrix}, \boldsymbol{\psi}_{sabc} = \begin{bmatrix} \psi_a \\ \psi_b \\ \psi_c \end{bmatrix}, \mathbf{r}_s = \begin{bmatrix} r_s & & \\ & r_s & \\ & & r_s \end{bmatrix}, \mathbf{r}_r = \begin{bmatrix} r_r & & \\ & r_r & \\ & & r_r \end{bmatrix}$$

The stator and rotor flux can be expressed as:

$$\begin{bmatrix} \boldsymbol{\psi}_{sabc} \\ \boldsymbol{\psi}_{rabc} \end{bmatrix} = \begin{bmatrix} \mathbf{L}'_s & \mathbf{L}'_{sr} \\ (\mathbf{L}'_{sr})^T & \mathbf{L}'_r \end{bmatrix} \begin{bmatrix} \mathbf{i}_{sabc} \\ \mathbf{i}_{rabc} \end{bmatrix} \quad (2.2)$$

In which $\mathbf{L}'_s, \mathbf{L}'_{sr}, \mathbf{L}'_r$ are parameter matrices as follows:

$$\mathbf{L}'_s = \begin{bmatrix} L_{ls} + L_m & -\frac{1}{2}L_m & -\frac{1}{2}L_m \\ -\frac{1}{2}L_m & L_{ls} + L_m & -\frac{1}{2}L_m \\ -\frac{1}{2}L_m & -\frac{1}{2}L_m & L_{ls} + L_m \end{bmatrix}$$

$$\mathbf{L}'_r = \begin{bmatrix} L_{lr} + L_m & -\frac{1}{2}L_m & -\frac{1}{2}L_m \\ -\frac{1}{2}L_m & L_{lr} + L_m & -\frac{1}{2}L_m \\ -\frac{1}{2}L_m & -\frac{1}{2}L_m & L_{lr} + L_m \end{bmatrix}$$

$$\mathbf{L}'_{sr} = L_m \begin{bmatrix} \cos(\omega_r t) & \cos(\omega_r t + \frac{2\pi}{3}) & \cos(\omega_r t - \frac{2\pi}{3}) \\ \cos(\omega_r t - \frac{2\pi}{3}) & \cos(\omega_r t) & \cos(\omega_r t + \frac{2\pi}{3}) \\ \cos(\omega_r t + \frac{2\pi}{3}) & \cos(\omega_r t - \frac{2\pi}{3}) & \cos(\omega_r t) \end{bmatrix}$$

L_{ls} and L_{lr} are stator and rotor leakage inductance, L_m is the mutual inductance, ω_r is the rotor angular speed, t is the time.

Perform $dq0$ transformation on (2.2), the following equation in $dq0$ frame can be obtained:

$$\begin{bmatrix} \psi_{sdq0} \\ \psi_{rdq0} \end{bmatrix} = \begin{bmatrix} \mathbf{K}\mathbf{L}'_s\mathbf{K}^{-1} & \mathbf{K}\mathbf{L}'_{sr}\mathbf{K}^{-1} \\ \mathbf{K}(\mathbf{L}'_{sr})^T\mathbf{K}^{-1} & \mathbf{K}\mathbf{L}'_r\mathbf{K}^{-1} \end{bmatrix} \begin{bmatrix} \mathbf{i}_{sdq0} \\ \mathbf{i}_{rdq0} \end{bmatrix} \quad (2.3)$$

The $dq0$ transformation matrix \mathbf{K} is given by:

$$\mathbf{K} = \frac{2}{3} \begin{bmatrix} \cos(\omega_e t) & \cos(\omega_e t - \frac{2\pi}{3}) & \cos(\omega_e t - \frac{4\pi}{3}) \\ -\sin(\omega_e t) & -\sin(\omega_e t - \frac{2\pi}{3}) & -\sin(\omega_e t - \frac{4\pi}{3}) \\ \frac{1}{2} & \frac{1}{2} & \frac{1}{2} \end{bmatrix}$$

In which ω_e is the angular speed of arbitrary referene frame, and:

$$\mathbf{K}\mathbf{L}'_s\mathbf{K}^{-1} = \begin{bmatrix} L_{ls} + L_M & & \\ & L_{ls} + L_M & \\ & & L_{ls} \end{bmatrix}, \quad \mathbf{K}\mathbf{L}'_r\mathbf{K}^{-1} = \begin{bmatrix} L_{lr} + L_M & & \\ & L_{lr} + L_M & \\ & & L_{lr} \end{bmatrix},$$

$$\mathbf{K}\mathbf{L}'_{sr}\mathbf{K}^{-1} = \mathbf{K}(\mathbf{L}'_{sr})^T\mathbf{K}^{-1} = \begin{bmatrix} L_M & & \\ & L_M & \\ & & 0 \end{bmatrix} = \mathbf{L}_m$$

In which $L_M = \frac{3}{2}L_m$, let $L_s = L_{ls} + L_M$, $L_r = L_{lr} + L_M$, it can be obtained that:

$$\mathbf{L}_s = \mathbf{K}\mathbf{L}'_s\mathbf{K}^{-1} = \begin{bmatrix} L_s & & \\ & L_s & \\ & & L_{ls} \end{bmatrix}, \quad \mathbf{L}_r = \mathbf{K}\mathbf{L}'_r\mathbf{K}^{-1} = \begin{bmatrix} L_r & & \\ & L_r & \\ & & L_{lr} \end{bmatrix}$$

Then (2.3) can be written as:

$$\begin{bmatrix} \psi_{sdq0} \\ \psi_{rdq0} \end{bmatrix} = \begin{bmatrix} \mathbf{L}_s & \mathbf{L}_m \\ \mathbf{L}_m & \mathbf{L}_r \end{bmatrix} \begin{bmatrix} \dot{\mathbf{i}}_{sdq0} \\ \dot{\mathbf{i}}_{rdq0} \end{bmatrix} \quad (2.4)$$

Perform $dq0$ transformation on (2.1), the stator and rotor equations of the open-end winding induction motor in arbitrary frame can be written as:

$$\begin{bmatrix} \mathbf{v}_{sdq0} \\ \mathbf{0} \end{bmatrix} = \begin{bmatrix} \mathbf{r}_s \\ \mathbf{r}_r \end{bmatrix} \begin{bmatrix} \dot{\mathbf{i}}_{sdq0} \\ \dot{\mathbf{i}}_{rdq0} \end{bmatrix} + p \begin{bmatrix} \psi_{sdq0} \\ \psi_{rdq0} \end{bmatrix} + \begin{bmatrix} \mathbf{J}\omega_e \\ \mathbf{J}(\omega_e - \omega_r) \end{bmatrix} \begin{bmatrix} \psi_{sdq0} \\ \psi_{rdq0} \end{bmatrix} \quad (2.5)$$

Where \mathbf{J} is the coupling matrix, and it is given by:

$$\mathbf{J} = \begin{bmatrix} 0 & -1 & 0 \\ 1 & 0 & 0 \\ 0 & 0 & 0 \end{bmatrix}$$

(2.4) and (2.5) are the state-space expression of the electrical model of the open-end winding induction motor including zero-sequence components. The electrical torque can be calculated using either flux or current, and it can be expressed as:

$$T_e = \frac{3}{2}P(\psi_{rq}i_{rd} - \psi_{rd}i_{rq}) \quad (2.6)$$

$$T_e = \frac{3}{2}P\frac{L_M}{L_s}(\psi_{sq}i_{rd} - \psi_{sd}i_{rq}) \quad (2.7)$$

$$T_e = \frac{3}{2}P\frac{L_M}{L_r}(\psi_{rd}i_{sq} - \psi_{rq}i_{sd}) \quad (2.8)$$

$$T_e = \frac{3}{2}P\frac{L_M}{L_s L_r \sigma}(\psi_{sq}\psi_{rd} - \psi_{sd}\psi_{rq}) \quad (2.9)$$

$$T_e = \frac{3}{2}PL_M(i_{rd}i_{sq} - i_{rq}i_{sd}) \quad (2.10)$$

2.1.2 Mechanical Model

The mechanical model of the open-end winding induction motor is given by:

$$T_e = J\frac{2}{P}\frac{d}{dt}\omega_r + T_L \quad (2.11)$$

Where J is the inertia of the motor, P is the number of poles, T_L is the load torque.

2.2 PWM Strategies of Open-End Winding Induction Motors

Many researchers have investigated the modulation strategies to achieve flexibility of control, reduction of harmonics, and elimination of common mode voltage in open-end winding machines [23–25, 38–44]. Depending on topologies of inverters or number of DC sources being used for the open-end winding machines, various PWM strategies are proposed in the literature.

With a configuration of three single-phase H-bridges, a PWM scheme with controllable grid power factor and higher phase voltage is proposed in [38]. When the topology is configured as dual two-level three-phase inverters, a high power three-phase synchronous motor with open windings is presented in [39]. Using the same power circuits, a space vector PWM strategy using the redundancy in switching states is presented in [23]; a PWM strategy with improved DC-bus utilization is also illustrated in [40].

As shown in Figure 2.1, two two-level three-phase inverters are used in the open-end winding induction motor drive. Hence three voltage levels can be generated across the phase winding, i.e., $+V_{DC}$, 0 or $-V_{DC}$. Also, by interleaved switching of the two inverters, the switching frequency across the phase winding is two times the frequency of the individual inverter. In this section, the switching patterns of the two inverters are studied, the voltage vector generation is investigated, and the PWM strategy for the open-end winding induction motor is discussed.

2.2.1 Switching Patterns and Voltage Vectors

For conventional induction motor fed by single two-level inverter, 8 switching states are available. These 8 switching states can be mapped onto a two-level hexagon, as shown in Figure 2.2. Due to the fact that a wye-connected motor is three-phase balanced, there is no zero-sequence component in this configuration. Hence the switching states 000 and 111 are equivalent, and 7 voltage vectors can be generated from the 8 switching states.

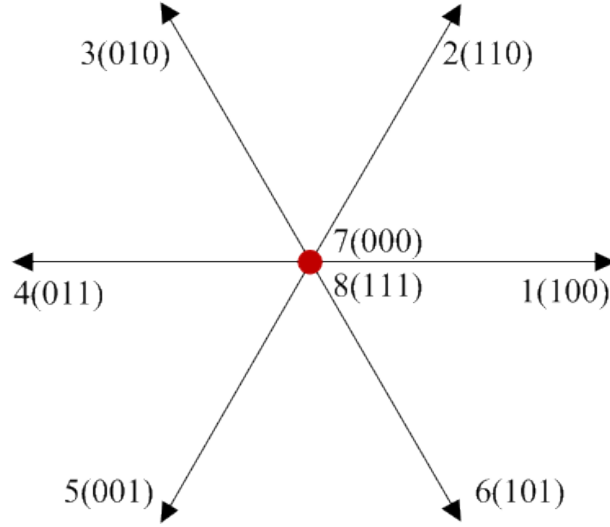


Figure 2.2: Switching States of A Two-Level Inverter

For open-end winding induction motor fed by two inverters, a total of 64 switching states can be generated by switching the two inverters. These 64 switching states can be mapped onto a three-level hexagon, as shown in Figure 2.3. It can be noticed that the structure in Figure 2.3 is similar to the switching states generated by a three-level inverter, in which 19 voltage vectors represented by A through S are located within the three-level hexagon. However, due to the fact that the two inverters share the same DC-link, zero-sequence voltage is generated across the phase winding. Therefore, in the common DC-link configuration, a total of 27 different voltage vectors can be generated from the 64 switching states. The 27 voltage vectors and corresponding switching states are listed in Table 2.1.

2.2.2 Zero-Sequence Current Suppression

The zero-sequence voltage generated by the two inverters is defined as:

$$v_0 = \frac{1}{3}(v_{aa'} + v_{bb'} + v_{cc'}) \quad (2.12)$$

It can be observed from Table 2.1 that some switching combinations can generate zero sequence voltage, which results in zero-sequence current flowing within the drive system.

Table 2.1: Switching States and Voltage Vectors in Open-End Winding Induction Motors

Number	Switching State	Voltage Vector		
		$V_\alpha(V_{DC})$	$V_\beta(V_{DC})$	$V_0(V_{DC})$
1	8 - 7'	0	0	-1
2	7 - 4', 1 - 8'	0.6667	0	-0.6667
3	1 - 4'	1.3333	0	-0.3333
4	7 - 6', 3 - 8'	-0.3333	0.5774	-0.6667
5	1 - 6', 2 - 8', 3 - 4', 7 - 5'	0.3333	0.5774	-0.3333
6	1 - 5', 2 - 4'	1	0.5774	0
7	3 - 6'	-0.6667	1.1547	-0.3333
8	3 - 5', 2 - 6'	0	1.1547	0
9	2 - 5'	0.6667	1.1547	0.3333
10	5 - 8', 7 - 2'	-0.3333	-0.5774	-0.6667
11	1 - 2', 5 - 4', 6 - 8', 7 - 3'	0.3333	-0.5774	-0.3333
12	1 - 3', 6 - 4'	1	-0.5774	0
13	3 - 2', 4 - 8', 5 - 6', 7 - 1'	-0.6667	0	-0.3333
14	1 - 1', 2 - 2', 3 - 3', 4 - 4' 5 - 5', 6 - 6', 7 - 7', 8 - 8'	0	0	0
15	1 - 7', 2 - 3', 6 - 5', 8 - 4'	0.6667	0	0.3333
16	3 - 1', 4 - 6'	-1	0.5774	0
17	2 - 1', 3 - 7', 4 - 5', 8 - 6'	-0.3333	0.5774	0.3333
18	2 - 7', 8 - 5'	0.3333	0.5774	0.6667
19	5 - 2'	-0.6667	-1.1547	-0.3333
20	5 - 3', 6 - 2'	0	-1.1547	0
21	6 - 3'	0.6667	-1.1547	0.3333
22	5 - 1', 4 - 2'	-1	-0.5774	0
23	4 - 3', 5 - 7', 6 - 1', 8 - 2'	-0.3333	-0.5774	0.3333
24	6 - 7', 8 - 3'	0.3333	-0.5774	0.6667
25	4 - 1'	-1.3333	0	0.3333
26	4 - 7', 8 - 1'	-0.6667	0	0.6667
27	7 - 8'	0	0	1

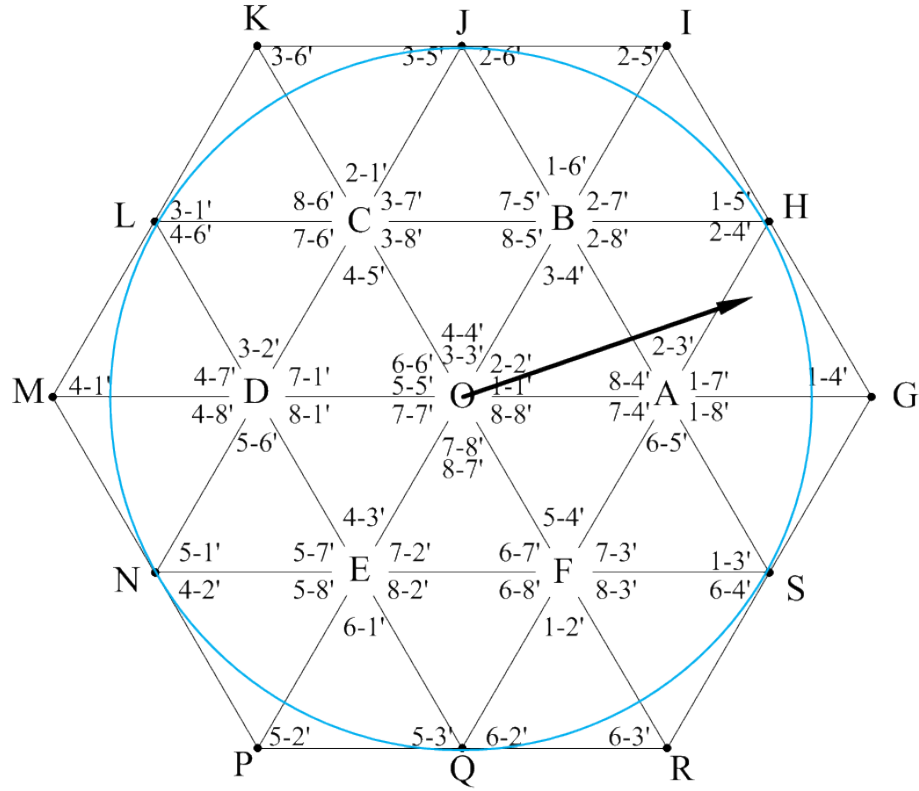


Figure 2.3: Switching States of Two Inverters in Open-End Winding Induction Motors

To suppress the zero-sequence current, proper switching strategy must be developed. It is noticed from Table 2.1 that among the 27 different voltage vectors, there are 7 voltage vectors which do not generate any zero-sequence voltage. One possible method to suppress the zero-sequence current is to only use these 7 non-zero-sequence-voltage-generating voltage vectors. However, this method will result in larger current ripples due to the insufficient use of the 27 voltage vectors.

Another option to suppress the zero-sequence current is to use the volt-second balancing of multiple voltage vectors. As shown in Figure 2.4, the 7 non-zero-sequence-voltage-generating voltage vectors form a shaded intermediate hexagon. Within this shaded hexagon, zero-sequence voltage can be suppressed to zero by volt-second balancing of different voltage vectors. The inscribing circle to the shaded hexagon represents the maximum magnitude of

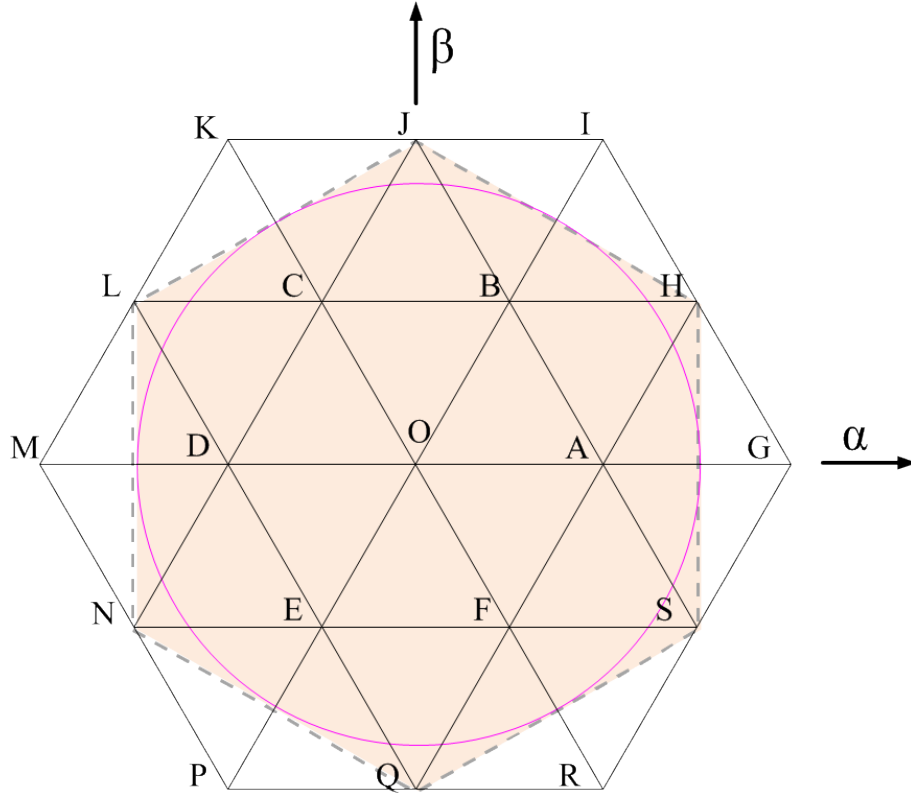


Figure 2.4: 2-D View of Voltage Vectors of Open-End Winding Induction Motors

the voltage vector which has zero zero-sequence voltage. When voltage vectors fall outside the shaded hexagon, the zero-sequence current is inevitable and cannot be controlled.

The above phenomenon can also be understood by looking at the three-dimensional view of the voltage vectors. Remap the 27 voltage vectors in a three-dimensional space as shown in Figure 2.5, the 27 voltage vectors are marked with red circles. It can be observed that the projections of the 27 voltage vectors on the plane $v_{s0} = 0$ form the same three-level hexagon shown in Figure 2.4. It can be noticed that only 7 voltage vectors locate on the plane $v_{s0} = 0$, the other 20 voltage vectors locate on 6 other planes with $v_{s0} = \pm\frac{1}{3}V_{DC}, \pm\frac{2}{3}V_{DC}, \pm V_{DC}$, which means these 20 voltage vectors will generate zero-sequence current as described in Table 2.1.

It can be also noticed that the 27 voltage vectors locate on a cube, which is marked by the dashed lines. The length of each edge of the cube is $2V_{DC}$, which represents the voltage limit. In other words, the two inverters can only generate voltage vectors which locate on the

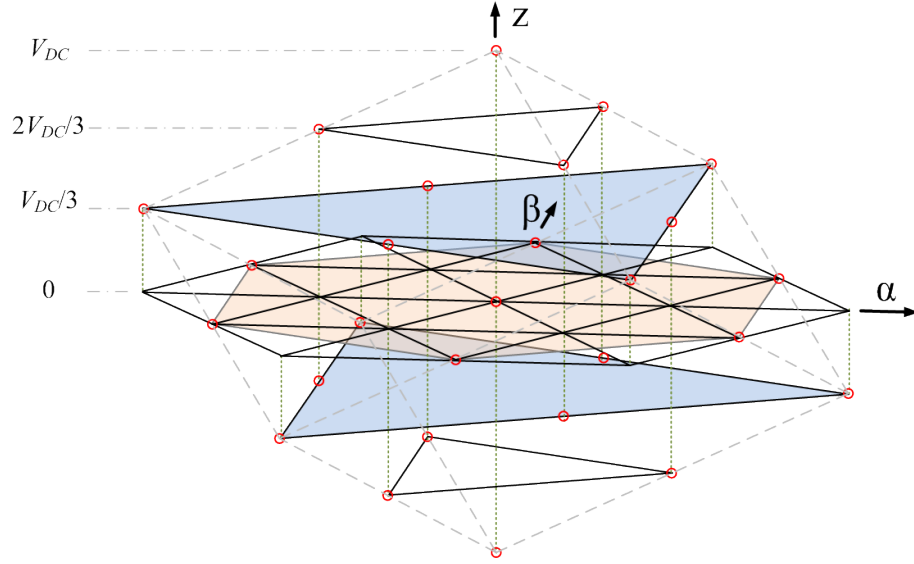


Figure 2.5: 3-D View of Voltage Vectors of Open-End Winding Induction Motors

surface of the cube or inside the cube. The intersection of the cube with the plane $v_{s0} = 0$ is marked as a shaded hexagon in Figure 2.5. Within this shaded hexagon, the zero-sequence current can be suppressed close to zero level. When the voltage vector is outside the shaded hexagon, uncontrollable zero-sequence current will flow.

2.2.3 PWM Generation of Open-End Winding Induction Motor Drives

As illustrated in Section 2.2.1, the two inverters need to generate the voltage vector which will be applied to the open-end winding induction motor. The relationship between the voltage vector generated from each inverter and the voltage vector applied to the induction motor can be described as:

$$\mathbf{v}_{12} = \mathbf{v}_{i1} - \mathbf{v}_{i2} \quad (2.13)$$

Where \mathbf{v}_{12} is the voltage vector applied to the motor, \mathbf{v}_{i1} and \mathbf{v}_{i2} are the voltage vectors generated by each individual inverter.

As the magnitude and angle of \mathbf{v}_{i1} and \mathbf{v}_{i2} can change arbitrarily, there are infinite number of combinations of \mathbf{v}_{i1} and \mathbf{v}_{i2} to generate \mathbf{v}_{12} . In this dissertation, the magnitudes

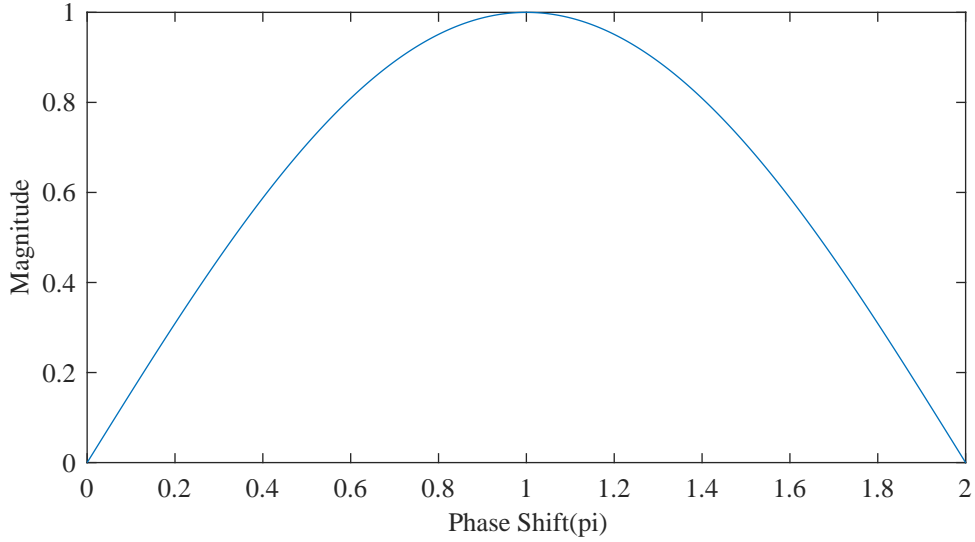


Figure 2.6: Magnitude of Combined Voltage Vector under Different Phase Shift

of \mathbf{v}_{i1} and \mathbf{v}_{i2} are set the same for the ease of calculation. Let θ_{12} be the phase difference between \mathbf{v}_{i1} and \mathbf{v}_{i2} , θ_r be the angle between \mathbf{v}_{i1} and stationary a phase, and V_{12} be the magnitude of \mathbf{v}_{i1} and \mathbf{v}_{i2} , (2.13) becomes:

$$\mathbf{v}_{12} = V_{12}\angle\theta_r - V_{12}\angle(\theta_r - \theta_{12}) \quad (2.14)$$

The relationship between the magnitude of \mathbf{v}_{12} and the phase shift θ_{12} is plotted in Figure 2.6. It can be observed that when the phase shift between \mathbf{v}_{i1} and \mathbf{v}_{i2} is 180° , the combined voltage vector \mathbf{v}_{12} has the maximum magnitude. In other words, to generate the same \mathbf{v}_{12} , maintaining the phase difference of 180° between the two inverters can make each inverter output minimized voltage vector, which means the inverters are utilized most efficiently.

In conventional wye-connected induction motor, either sinusoidal PWM (SPWM) or space vector PWM (SVPWM) can be used to generate the PWM signal. In particular, SVPWM is preferred since it makes better use of the modulation range, the magnitude of fundamental component is 1.15 times of that under SPWM. However, this merit is invalid in open-end winding configuration.

In SPWM, the reference signal of each inverter is a sinusoidal wave, hence Figure 2.6 is valid in generating the combined voltage vector. When the phase difference is 180° , the inverters reaches the optimal utilization in generating the voltage vectors. In the case of SVPWM, since the reference signal can be regarded as a fundamental sinusoidal wave added an offset, whose frequency is three times the fundamental. Hence the reference signal of SVPWM can be written as:

$$\begin{aligned}\mathbf{v}_{i1} &= V_{12}\angle\theta_r + V_{offset}\angle 3\theta_r \\ \mathbf{v}_{i2} &= V_{12}\angle(\theta_r + \theta_{12}) + V_{offset}\angle(3\theta_r + 3\theta_{12})\end{aligned}$$

Where V_{offset} is the magnitude of the offset signal. Substitute the above equations into (2.14), the combined voltage vector can be written as:

$$\mathbf{v}_{12} = V_{12}\angle\theta_r - V_{12}\angle(\theta_r - \theta_{12}) + (V_{offset}\angle 3\theta_r - V_{offset}\angle(3\theta_r + 3\theta_{12})) \quad (2.15)$$

It can be observed from (2.15) that a 3rd order frequency offset term is present in the combined voltage vector. To eliminate this offset term, the phase difference between the two inverters θ_{12} needs to satisfy the condition that $\theta_{12} = N\frac{2\pi}{3}$. Figure 2.7 shows the reference signal generation of SVPWM under 120° phase difference. It can be noticed that although the fundamental component of each inverter is 1.15 times larger than that under SPWM, this merit is cancelled by the 120° phase difference in order to eliminate the offset signal. Hence the magnitude of combined voltage vector is the same as that under SPWM.

In conclusion, in open-end winding configuration, SPWM with 180° phase difference and SVPWM with 120° phase difference are equivalent. In the following chapters of this dissertation, SPWM with 180° phase difference is used to generate the PWM signals.

2.3 Delay Compensation

As large amount of calculations are required in MPC methods, a non-negligible time delay is introduced before the actuation. Also, due to the zero-order-hold nature of the power

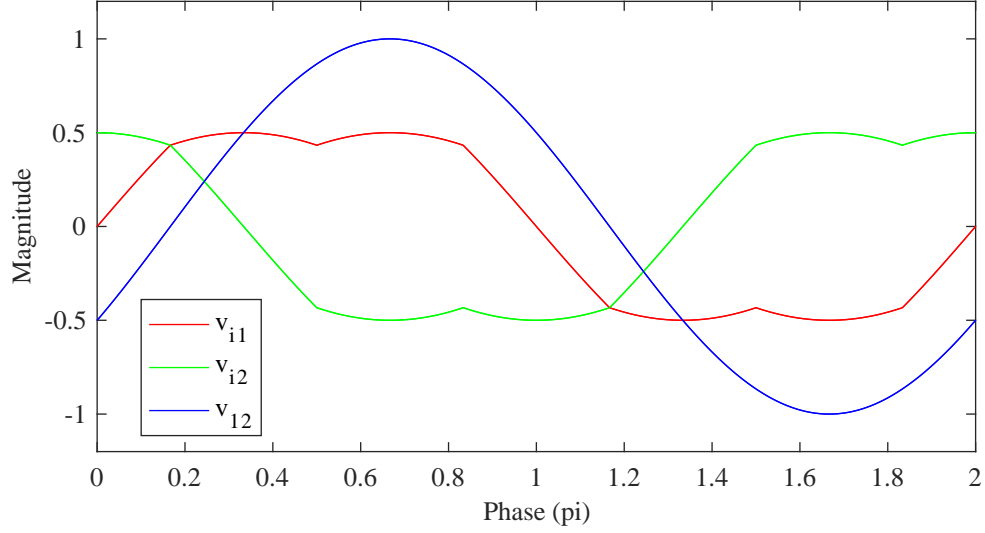


Figure 2.7: Reference Signal Generation of SVPWM with 120° Phase Difference

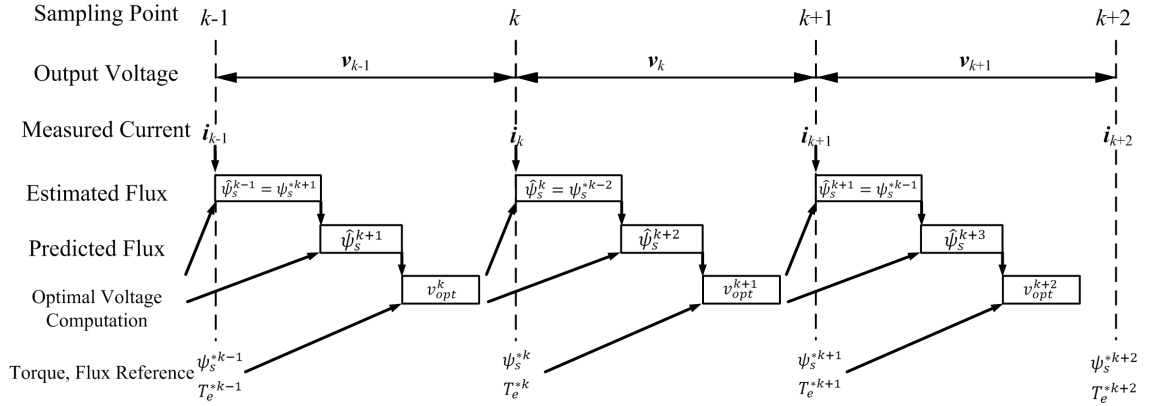


Figure 2.8: Control Sequence of PTC for Open-End Winding Induction Motors

converters, a delay on current is also brought in [45]. Ignorance of these delay effects would result in deteriorated performances of the system. Considering this problem, delay compensation methods have been proposed in literatures [46–50]. In this section, the cause of the delay is analyzed, and the compensation method for open-end winding induction motor drive is introduced.

In a typical MPC method, several steps need to be accomplished to obtain the optimal actuation. Figure 2.8 shows the control sequence of predictive torque control (PTC) for

open-end winding induction motor. At time instant k , the optimal voltage vector $\mathbf{v}_{opt,k}$, which is calculated in the previous sampling period, is applied to the inverters. At the same point, the motor stator currents are measured to obtain the current vector $\mathbf{i}_{s,k}$. During the time period between k and $k + 1$, the digital controller needs to finish calculation of finding optimal voltage vector $\mathbf{v}_{opt,k+1}$. At time instant $k + 1$, $\mathbf{v}_{opt,k+1}$ is applied to inverters. And during the time interval between $k + 1$ and $k + 2$, $\mathbf{v}_{opt,k+1}$ is held and effective on the open-end winding induction motor. At time instant $k + 2$, the estimated flux and torque should be equal to the reference values which are set at time instant k . Hence there are two samples delay between the reference state and the actual realized state.

To compensate for this delay, prediction of stator flux and electrical torque at time instant $k + 2$ is required. Based on $\mathbf{v}_{opt,k}$ and $\mathbf{i}_{s,k}$, the stator and rotor flux vectors $\hat{\psi}_{s,k}$ and $\hat{\psi}_{r,k}$ are estimated. From the estimated flux vectors and the voltage vector $\mathbf{v}_{opt,k}$, the stator flux and torque at time instant $k + 2$ can be predicted. Therefore, the delay resulted from digital calculation and power converter is compensated. The flowchart of PTC with delay compensation is shown in Figure 2.9.

2.4 Summary

In this chapter, the electrical and mechanical models of open-end winding induction motor fed by two three-phase VSIs sharing the same DC-link are presented. The PWM strategies of the open-end winding induction motor are analyzed in both 2-dimensional and 3-dimensional view. The cause of the zero-sequence current is also investigated. Considering the implementation on digital controllers and real motor drives, the delay resulted from digital calculation and zero-order-hold nature of power converters is also studied. The work in this chapter lays a theoretical foundation for the following chapters.

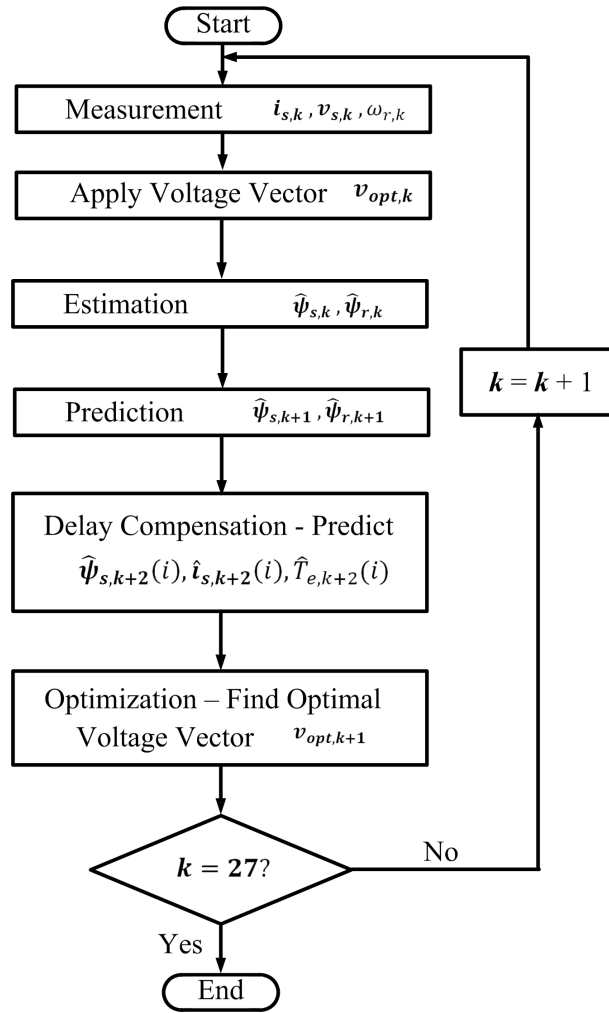


Figure 2.9: Flowchart of PTC with Delay Compensation for Open-End Winding Induction Motors

CHAPTER 3

FAST RESPONSE PREDICTIVE CONTROL FOR OPEN-END WINDING INDUCTION MOTORS ^{1,2}

In automotive testing systems, fast current/torque response is required to accurately track the dynamic behavior of the UUT and to minimize the measurement error. In this chapter, an open-end winding induction motor drive with two two-level inverters sharing the same DC-link is investigated. Four MPC methods, i.e., linear predictive current control (linear PCC), non-linear predictive current control (non-linear PCC), linear predictive torque control (linear PTC) and non-linear predictive torque control (non-linear PTC) and proposed [51, 52]. The transient and steady state responses of the four different methods are evaluated through simulation and experiment. The simulated and experimental results show that the proposed methods have faster dynamic responses compared to conventional control method. A detailed analysis is given on different aspects of the compared methods.

3.1 Introduction

In Section 1.3.2, linear and non-linear model predictive control methods on conventional wye-connected induction motor drive have been reviewed [30, 34, 35]. Based on the state variables being used in the model, the linear MPC method and non-linear MPC method can be further subdivided into two types. One is predictive current control (PCC), and the other is predictive flux/torque control (PTC). In linear PCC, a deadbeat controller is

¹©2015 IEEE. Portion Adapted, with permission, from B. Zhu, K. Rajashekara and H. Kubo, "Predictive torque control with zero-sequence current suppression for open-end winding induction machine", Industry Applications Society Annual Meeting, 2015 IEEE

²©2017 IET. Portion Adapted, with permission, from B. Zhu, K. Rajashekara and H. Kubo, "A Comparison between Current Based and Flux/Torque Based Model Predictive Control Methods for Open-End Winding Induction Motor Drives", the work in this paper is a postprint of a paper submitted to and accepted for publication in IET Electric Power Applications and is subjected to Institution of Engineering and Technology Copyright. The copy of record is available at the IET Digital Library

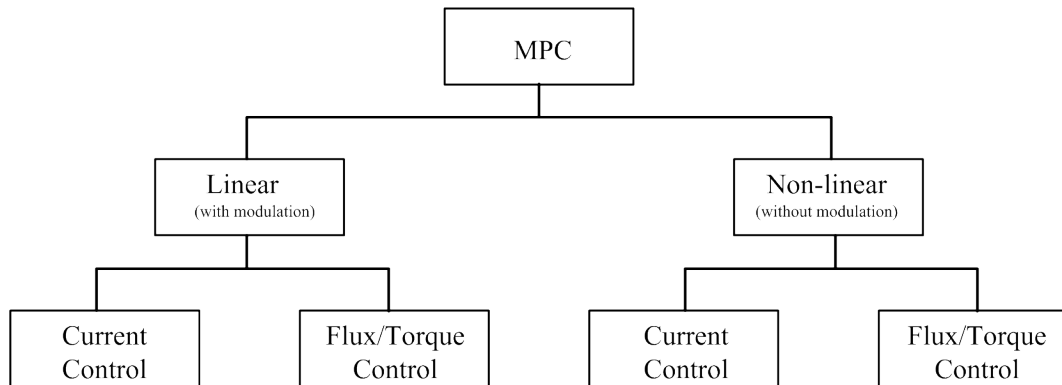


Figure 3.1: MPC Methods for Open-End Winding Induction Motor Drives

used to regulate the currents, and the reference voltage vector is generated using predicted current and predicted back EMF [28, 53]. In non-linear PCC, the cost function evaluates the errors between current references and predicted currents to determine the optimal switching pattern [34, 35, 54–57]. In linear PTC, or deadbeat flux/torque control as mentioned in [58–60], stator flux and electrical torque are predicted to generate the voltage reference. In non-linear PTC, the cost function evaluates the errors of flux magnitude and torque magnitude to determine the optimal switching pattern, usually a weighting factor is required in this method [46, 61–64]. Also, non-linear MPC methods using hysteresis control and trajectory control are reported in [36, 37, 65–67]. Figure 3.1 shows the classification of MPC methods for open-end winding induction motor drive.

A comparison of direct MPC methods has been reported in [64], in which both non-linear PCC and non-linear PTC have been applied to a wye-connected induction motor fed by a two-level inverter. However, in the system studied in this dissertation, two two-level inverters with common DC-link are employed. New control strategies need to be developed to address the zero-sequence current issue and to provide proper control on the two inverters. Hence, it is still necessary to evaluate the effectiveness of MPC methods on the OEWIM. In this chapter, four MPC methods are proposed and examined [51, 52], and the results prove that the proposed methods can effectively suppress the zero-sequence current as well as provide fast dynamic response over a wide operation range.

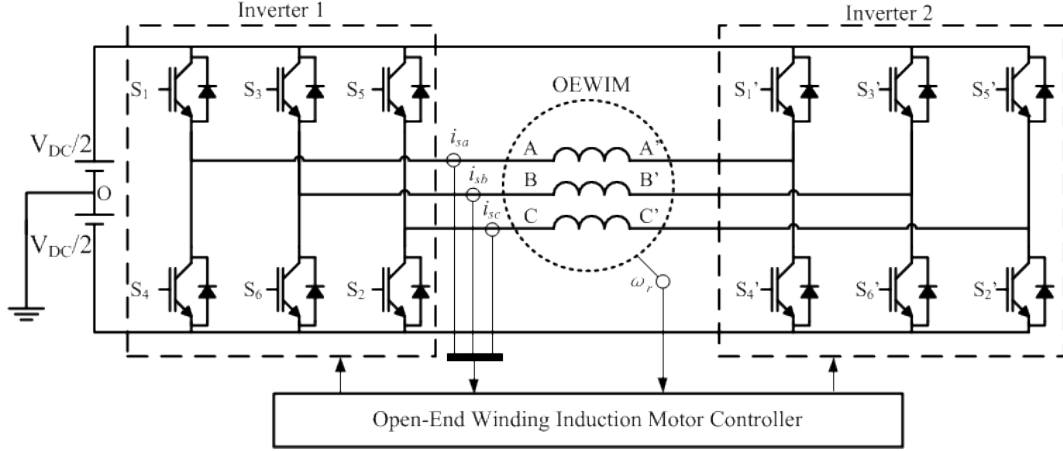


Figure 3.2: Open-end Winding Induction Motor Drives

3.2 Theoretical Derivation

The configuration of the OEWM with two two-level inverters sharing the same DC-link is shown in Figure 3.2. From (2.4) and (2.5) the electrical model of OEWM in arbitrary reference frame can be written as:

$$\begin{bmatrix} \mathbf{v}_s \\ \mathbf{v}_r \end{bmatrix} = \begin{bmatrix} \mathbf{r}_s \\ \mathbf{r}_r \end{bmatrix} \begin{bmatrix} \mathbf{i}_s \\ \mathbf{i}_r \end{bmatrix} + p \begin{bmatrix} \boldsymbol{\psi}_s \\ \boldsymbol{\psi}_r \end{bmatrix} + \begin{bmatrix} \mathbf{J}_3 \omega_a & \\ & \mathbf{J}_3(\omega_a - \omega_r) \end{bmatrix} \begin{bmatrix} \boldsymbol{\psi}_s \\ \boldsymbol{\psi}_r \end{bmatrix} \quad (3.1)$$

$$\begin{bmatrix} \boldsymbol{\psi}_s \\ \boldsymbol{\psi}_r \end{bmatrix} = \begin{bmatrix} \mathbf{L}_s & \mathbf{L}_m \\ \mathbf{L}_m & \mathbf{L}_r \end{bmatrix} \begin{bmatrix} \mathbf{i}_s \\ \mathbf{i}_r \end{bmatrix} \quad (3.2)$$

Where $\mathbf{v}_s, \mathbf{i}_s, \mathbf{i}_r, \boldsymbol{\psi}_s, \boldsymbol{\psi}_r$ are state variables with zero-sequence component, e.g. $\mathbf{v}_s = \begin{bmatrix} v_{sd} & v_{sq} & v_{s0} \end{bmatrix}^T$. $\mathbf{R}_s, \mathbf{R}_r, \mathbf{L}_s, \mathbf{L}_r, \mathbf{L}_m$ are system parameter matrices, for instance: $\mathbf{R}_s = \text{diag} \begin{bmatrix} R_s & R_s & R_s \end{bmatrix}, \mathbf{L}_s = \text{diag} \begin{bmatrix} L_s & L_s & L_{ls} \end{bmatrix}, \mathbf{L}_m = \text{diag} \begin{bmatrix} L_m & L_m & 0 \end{bmatrix}$. ω_a is arbitrary reference frequency, ω_r is the electrical frequency of the rotor, p is the derivative

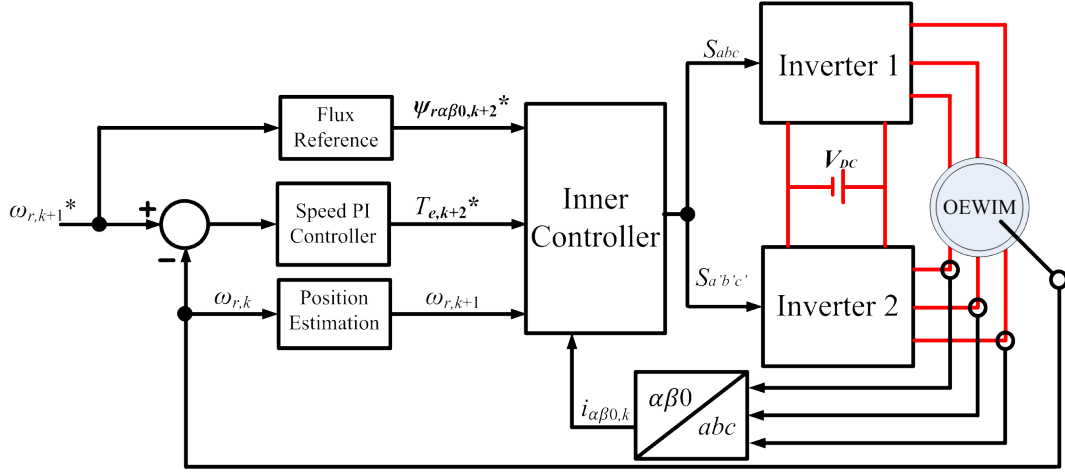


Figure 3.3: Block Diagram of the Open-End Winding Induction Motor Drive

operator. The coupling matrix \mathbf{J}_3 can be written as:

$$\mathbf{J}_3 = \begin{bmatrix} 0 & -1 & 0 \\ 1 & 0 & 0 \\ 0 & 0 & 0 \end{bmatrix}$$

The block diagram of the controller is shown in Figure 3.3. Depending on different control methods, the inner controller changes accordingly.

3.2.1 Predictive Current Control (PCC)

From (3.1)(3.2), the derivative of the current vectors in stationary frame ($\omega_a = 0$) can be written as:

$$p \begin{bmatrix} \mathbf{i}_s \\ \mathbf{i}_r \end{bmatrix} = \begin{bmatrix} \mathbf{L}_s & \mathbf{L}_m \\ \mathbf{L}_m & \mathbf{L}_r \end{bmatrix}^{-1} \left(\begin{bmatrix} \mathbf{v}_s \\ \mathbf{0} \end{bmatrix} - \begin{bmatrix} \mathbf{R}_s & \\ & \mathbf{R}_r \end{bmatrix} \begin{bmatrix} \mathbf{i}_s \\ \mathbf{i}_r \end{bmatrix} - \begin{bmatrix} \mathbf{0} & \mathbf{0} \\ \mathbf{0} & -\omega_r \mathbf{J}_3 \end{bmatrix} \begin{bmatrix} \boldsymbol{\psi}_s \\ \boldsymbol{\psi}_r \end{bmatrix} \right) \quad (3.3)$$

The stator current equation can be obtained from (3.3):

$$p \mathbf{i}_s = \frac{\mathbf{I}_3}{\mathbf{L}_s \boldsymbol{\sigma}} \left(\mathbf{v}_s - \mathbf{R}_s \mathbf{i}_s + \frac{\mathbf{L}_m}{\mathbf{L}_r} (\mathbf{R}_r \mathbf{i}_r - \omega_r \mathbf{J}_3 \boldsymbol{\psi}_r) \right) \quad (3.4)$$

Where $\boldsymbol{\sigma} = \mathbf{I}_3 - \frac{L_m^2}{L_s L_r}$, \mathbf{I}_3 is dimension 3 identity matrix. The back EMF in (3.3) then can be written as:

$$\mathbf{v}_l = \mathbf{R}_s \mathbf{i}_s - \frac{L_m}{L_r} (\mathbf{R}_r \mathbf{i}_r - \omega_r \mathbf{J}_3 \psi_r) \quad (3.5)$$

An open-loop flux estimator is used for calculating the rotor flux in (3.5). The rotor flux in rotor reference frame ($\omega_a = \omega_r$) can be estimated as:

$$p\psi_r = \frac{L_m}{L_r} \mathbf{i}_s - \frac{\mathbf{I}_3}{\tau_r} \psi_r \quad (3.6)$$

Where $\tau_r = L_r / \mathbf{R}_r$. Substitute (3.5) into (3.3):

$$p\mathbf{i}_s = \frac{\mathbf{I}_3}{L_s \boldsymbol{\sigma}} (\mathbf{v}_s - \mathbf{v}_l) \quad (3.7)$$

Discretize (3.7) using forward Euler method, the stator current can be predicted as:

$$\hat{\mathbf{i}}_{s,k+1} = \mathbf{i}_{s,k} + T_s \frac{\mathbf{I}_3}{L_s \boldsymbol{\sigma}} (\hat{\mathbf{v}}_{s,k} - \hat{\mathbf{v}}_{l,k}) \quad (3.8)$$

In which T_s is the sampling period of inner controller. Due to the digital calculation delay described in Section 2.3, one more step extrapolation is required to compensate this delay. After one more step iteration, (3.8) becomes:

$$\hat{\mathbf{i}}_{s,k+2} = \hat{\mathbf{i}}_{s,k+1} + T_s \frac{\mathbf{I}_3}{L_s \boldsymbol{\sigma}} (\hat{\mathbf{v}}_{s,k+1} - \hat{\mathbf{v}}_{l,k+1}) \quad (3.9)$$

By using the deadbeat control law, $\hat{\mathbf{i}}_{s,k+2} = \mathbf{i}_s^*$, the reference voltage needed to apply at time instant $k+1$ can be obtained as:

$$\hat{\mathbf{v}}_{s,k+1} = \frac{\mathbf{I}_3}{T_s L_s \boldsymbol{\sigma}} (\mathbf{i}_s^* - \hat{\mathbf{i}}_{s,k+1}) + \hat{\mathbf{v}}_{l,k+1} \quad (3.10)$$

The current reference \mathbf{i}_s^* is obtained from flux reference and torque reference in a similar way to conventional field oriented control. The block diagram of linear PCC is shown in Figure 3.4.

For non-linear PCC, a cost function is used to select the optimal voltage vector to be applied on the inverters. As open-end winding configuration uses two two-level inverters, a

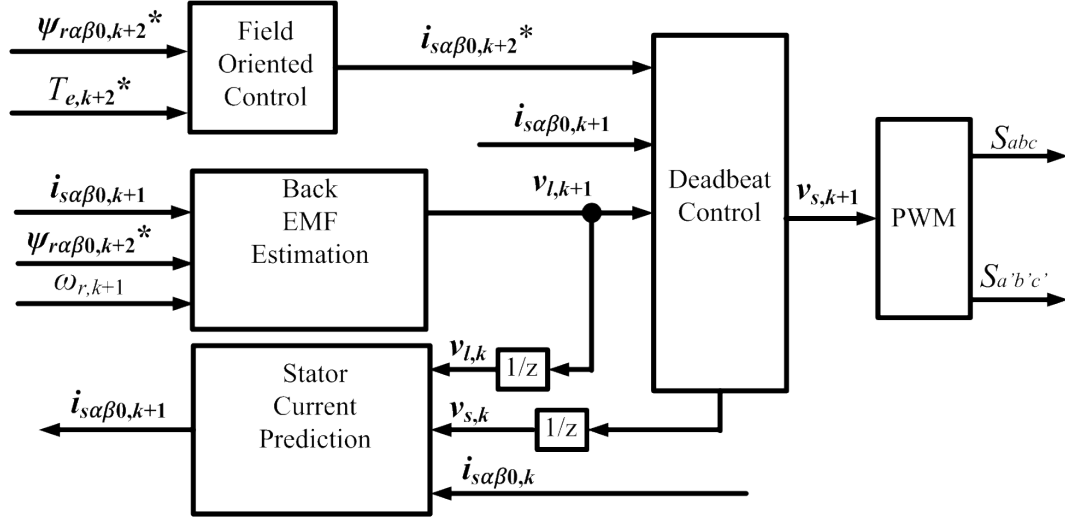


Figure 3.4: Block Diagram of Inner Controller Using Linear PCC

total of 64 switching combinations can be mapped onto 27 different voltage vectors [51]. By substituting $\hat{\mathbf{v}}_{s, k+1}$ in (3.9) with 27 possible voltage vectors, (3.9) becomes:

$$\hat{\mathbf{i}}_{s, k+2}(i) = \hat{\mathbf{i}}_{s, k+1} + T_s \frac{\mathbf{I}_3}{L_s \sigma} (\hat{\mathbf{v}}_{s, k+1}(i) - \hat{\mathbf{v}}_{l, k+1}) \quad (3.11)$$

Where i varies from 1 to 27. And the cost function is given by:

$$g(i) = w_\alpha \left| i_{s\alpha}^* - \hat{i}_{s\alpha, k+2}(i) \right| + w_\beta \left| i_{s\beta}^* - \hat{i}_{s\beta, k+2}(i) \right| + w_0 \left| \hat{i}_{s0, k+2}(i) \right| \quad (3.12)$$

Where w_α, w_β, w_0 are weighting factors of current errors. Then the voltage vector to be applied on the inverters can be obtained as:

$$\mathbf{v}_{opt, k+1} = \arg \min_{\{i=1,2,\dots,27\}} g(i) \quad (3.13)$$

The block diagram of non-linear PCC is shown in Figure 3.5.

3.2.2 Predictive Torque Control (PTC)

Discretize (3.6) using forward Euler method, the rotor flux at time instant $k + 1$ can be predicted as:

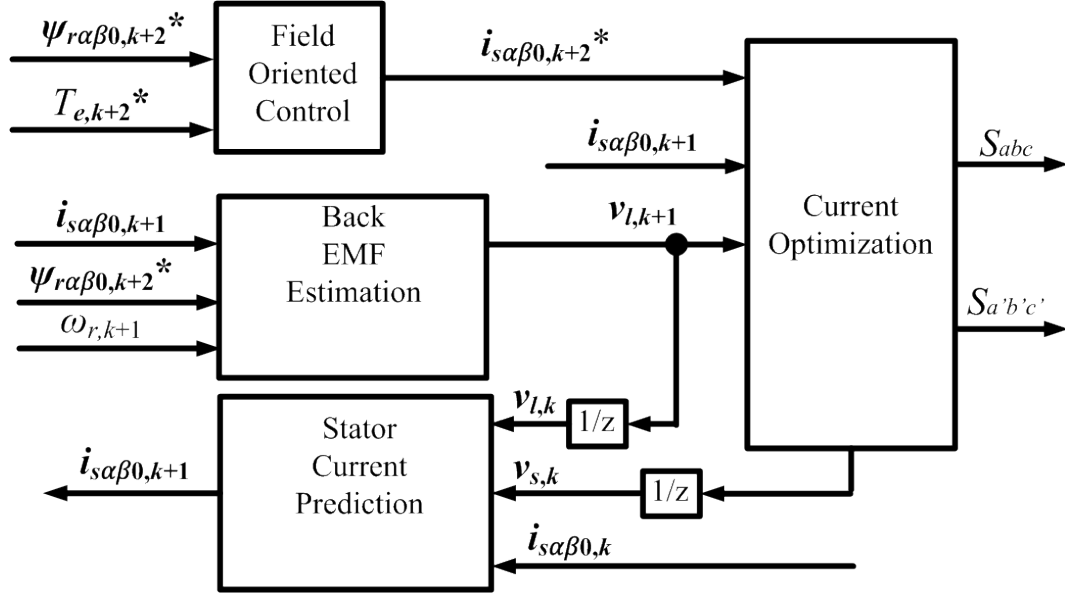


Figure 3.5: Block Diagram of Inner Controller Using Non-Linear PCC

$$\hat{\psi}_{r,k+1} = \frac{L_m}{\tau_r} T_s i_{s,k} + \left(\mathbf{I}_3 - \frac{\mathbf{I}_3}{\tau_r} \right) T_s \psi_{r,k} \quad (3.14)$$

To predict the stator flux at time instant $k + 1$, one can use the stator current equation in (3.1), and the stator flux in arbitrary frame can be predicted as:

$$\hat{\psi}_{s,k+1} = T_s v_{s,k} + \left(\mathbf{I}_3 - T_s \left(\frac{\mathbf{I}_3}{\tau_s \sigma} + \mathbf{J}_3 \omega_{a,k} \right) \right) \psi_{s,k} + \frac{\mathbf{k}_r}{\tau_s \sigma} T_s + \psi_{r,k} \quad (3.15)$$

Where $\tau_s = L_s / R_s$, $\mathbf{k}_r = L_m / L_r$. Using (3.14) and (3.15), and perform one more step extrapolation, the per unit electrical torque at time instant $k + 2$ can be expressed as:

$$\hat{T}_{e,k+2} = \frac{L_m P}{\sigma L_s L_r} (\hat{\psi}_{sq,k+2} \hat{\psi}_{rd,k+2} - \hat{\psi}_{sd,k+2} \hat{\psi}_{rq,k+2}) \quad (3.16)$$

Where P is number of pole pairs. In rotor flux orientation frame ($\omega_a = \omega_e$, $\psi_{rd} = |\psi_r|$, $\psi_{rq} = 0$), ω_e is the synchronous frequency of the rotor flux, by using the deadbeat control law, $\hat{\psi}_{rd,k+2} = |\psi_r^*|$, $\hat{T}_{e,k+2} = T_e^*$. The d-axis and q-axis voltages to be applied at time instant $k + 1$ can be calculated as:

$$\hat{v}_{sd,k+1} = \frac{1}{T_s} |\psi_r^*| + \left(\frac{R_s}{\sigma L_s} - \frac{1}{T_s} \right) \hat{\psi}_{sd,k+1} - \hat{\omega}_{e,k+1} \hat{\psi}_{sq,k+1} - \frac{R_s L_m}{\sigma L_s L_r} \hat{\psi}_{rd,k+1} \quad (3.17)$$

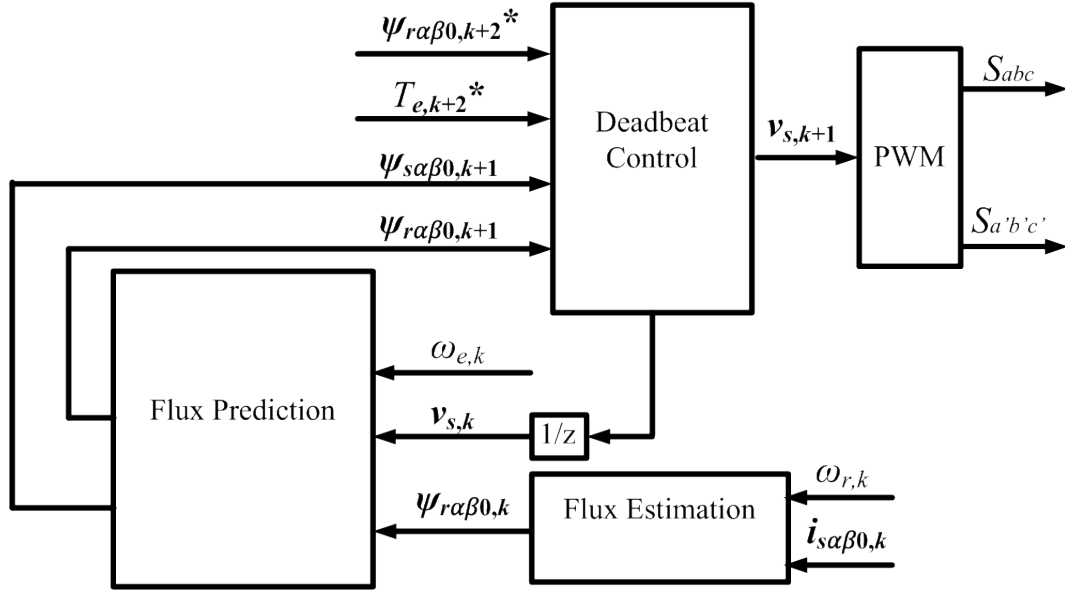


Figure 3.6: Block Diagram of Inner Controller Using Linear PTC

$$\hat{v}_{sq,k+1} = \frac{\sigma L_r}{PT_s} \frac{T_e^*}{|\psi_r^*|} - \left(\frac{1}{T_s} - \frac{R_s}{\sigma L_s} \right) \hat{\psi}_{sq,k+1} + \hat{\omega}_{e,k+1} \hat{\psi}_{sd,k+1} \quad (3.18)$$

The block diagram for linear PTC is shown in Figure 3.6.

For non-linear PTC, the cost function not only needs to minimize the torque error and stator flux magnitude error, but also needs to suppress the zero-sequence current. The electrical torque and stator flux magnitude can be obtained from (3.15) and (3.16), and the zero-sequence current can be predicted using the zero-sequence part of (3.9), and is rewritten as:

$$\hat{i}_{s0,k+2}(i) = \left(1 - \frac{T_s R_s}{L_{ls}} \right) \hat{i}_{s0,k+1} + \frac{T_s}{L_{ls}} \hat{v}_{s,k+1}(i) \quad (3.19)$$

Hence the cost function can be given as:

$$h(i) = w_{te} |T_e^* - \hat{T}_{e,k+2}(i)| + w_{\psi} \left| |\psi_s^*| - |\hat{\psi}_{s,k+2}(i)| \right| + w_0 |\hat{i}_{s0,k+2}(i)| \quad (3.20)$$

Where w_{te} , w_{ψ} and w_0 are the weighting factors of torque error, flux magnitude error and zero-sequence current respectively. Then, the optimal voltage vector \mathbf{v}_{opt} to be applied can be determined by:

$$\mathbf{v}_{opt,k+1} = \arg \min_{\{i=1,2,\dots,27\}} h(i) \quad (3.21)$$

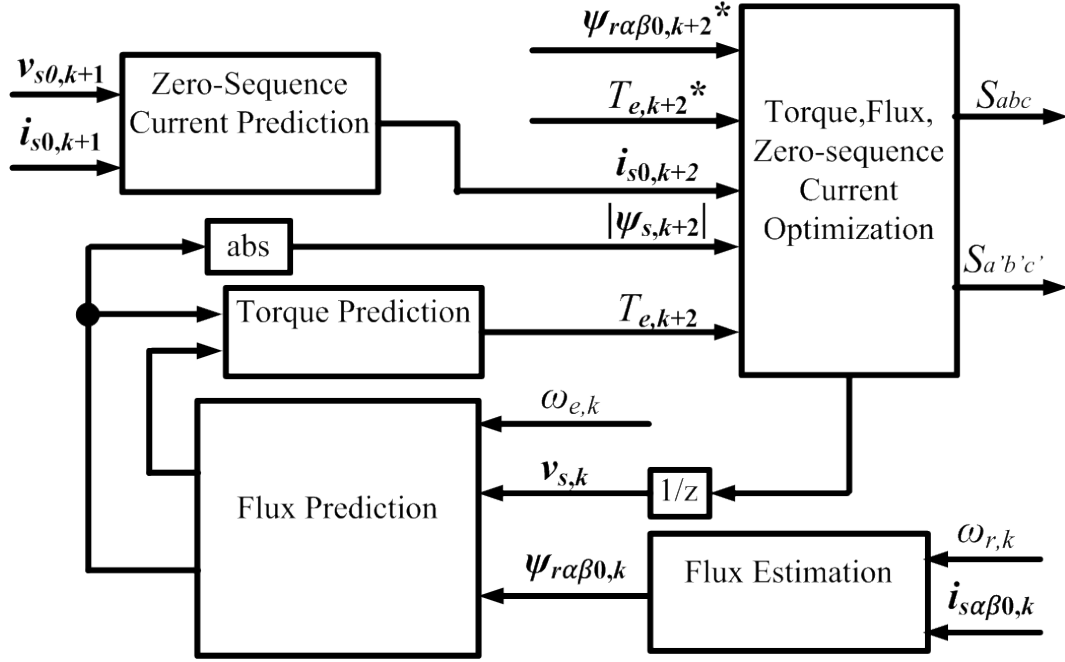


Figure 3.7: Block Diagram of Inner Controller Using Non-Linear PTC

The block diagram of non-linear PTC is shown in Figure 3.7.

3.3 Simulation Results

In order to validate the performances of the methods under study, an OEWM is modeled in Matlab/Simulink. The parameters and ratings of the motor are given in Table 3.1. The simulation step-length is set as $1e-7$ second, the sampling frequency of speed PI controller is 1kHz, and the sampling frequency of the inner controller used in simulation is 10 kHz. For non-linear PCC, the weighting factors in (3.12) are $w_\alpha = w_\beta = w_0 = 1$, for non-linear PTC, the weighting factors in (3.20) are $w_{te} = w_\psi = w_0 = 1$. A low pass filter with cutoff frequency 6000Hz is added between the current sampling and controller to provide same situation as in experiment. Since the SPWM and SVPWM methods are equivalent in open-end winding configuration as discussed in Section 2.2.3, SPWM is used in both simulation and in experiment. The dead-time of the inverter is set to be $2\mu s$.

Table 3.1: Motor Ratings and Parameters

Power(kW)	5.5
Poles	4
Rating Speed (rpm)	1470
Line to Line Voltage (V)	200
Stator Resistance ($m\Omega$)	834
Rotor Resistance ($m\Omega$)	654
Stator Leakage Inductance (mH)	3.2
Rotor Leakage Inductance (mH)	3.2
Mutual Inductance (mH)	138.1

3.3.1 Transient State Operation

The torque responses obtained from the above mentioned control strategies are shown in Figure 3.8. At $t=0.0005s$, for a 0.8 p.u. torque command, no significant difference is observed in the step responses. However, it can be observed that the non-linear MPC methods provide larger slopes than linear MPC methods, which means a faster torque response can be obtained by using non-linear MPC methods. This is because in non-linear MPC methods, the optimal voltage vector is applied to the motor during the whole sampling period, while in linear MPC methods, zero vectors are used in every sampling cycle, which do not provide any torque hence make the raising slope lower than non-linear MPC methods.

To estimate the frequency response of individual controllers, a sinusoidal torque perturbation with magnitude of 0.05 p.u. is injected to the reference torque. The frequency of the torque perturbation varies from 200 rad/s to 20000 rad/s. The reference torque and output electrical torque are measured over a frequency range from 200 rad/s to 20000 rad/s. The step length chosen for measurements is 200 rad/s. The frequency responses of the methods under comparison are shown in Figure 3.9. It can be observed that although all the methods present similar bandwidth, the non-linear PTC presents the largest phase margin, which means non-linear PTC provides fastest response among the MPC methods under comparison. It is also noticed that PCC methods preserve a more steady gain than PTC methods

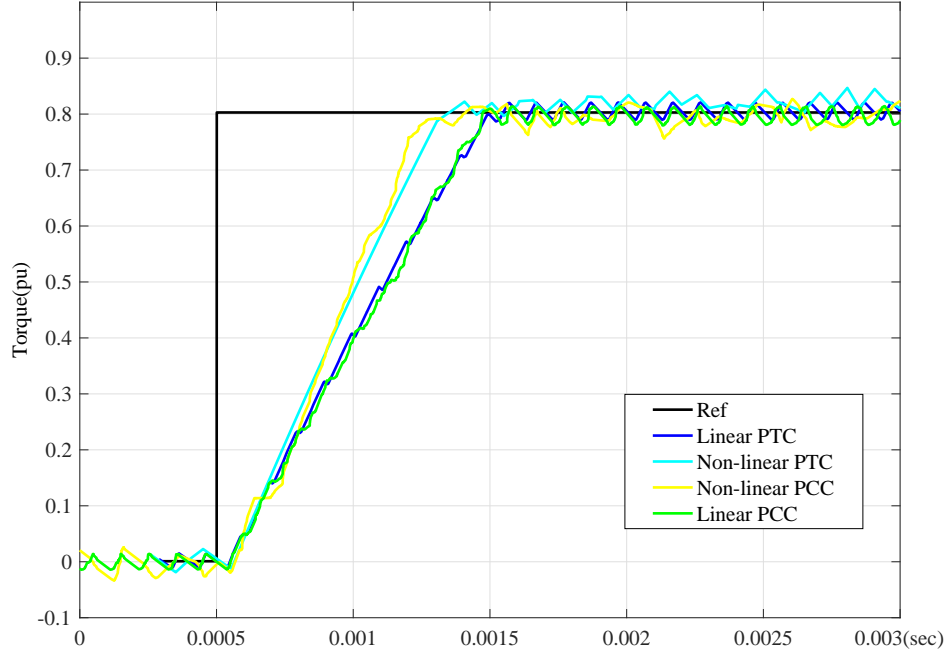


Figure 3.8: Torque Responses in Simulation

during the frequency response test, which means the PCC methods are expected to have less oscillations than PTC methods during transient state.

3.3.2 Steady State Operation

To examine the steady state performances, the induction motor is set to work under rated speed and 0.8 p.u. load. Figure 3.10 shows the steady state responses of the linear and non-linear MPC methods. It can be observed that linear MPC methods provide less distortion on the phase currents, this can be explained by comparing the switching frequency of linear and non-linear MPC methods. Under the same sampling frequency 10kHz, by interleaved switching of the two inverters, the linear MPC methods maintain a constant 20kHz switching frequency across the phase winding; while the non-linear MPC methods do not have control on switching frequency, and the actual switching frequency across the winding is less than

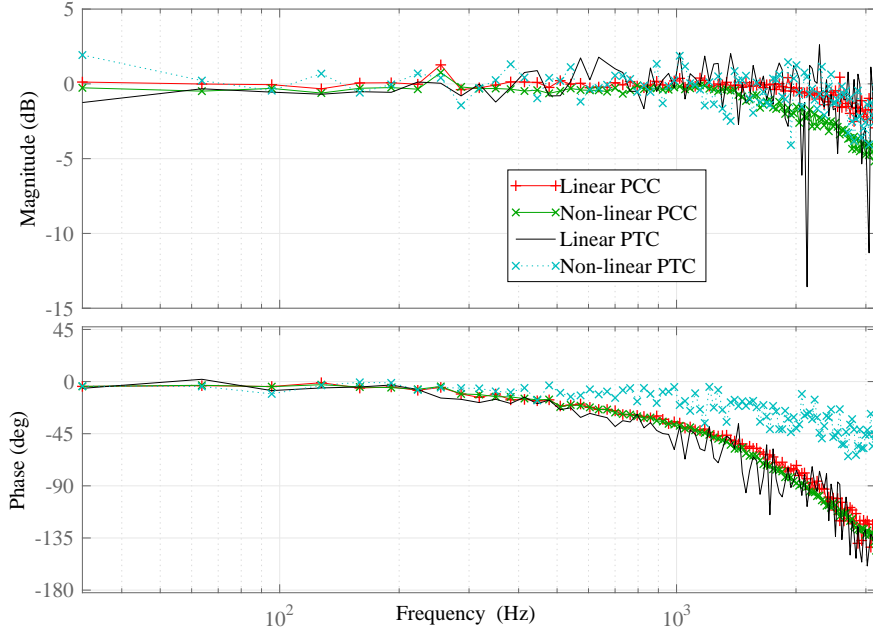


Figure 3.9: Frequency Responses in Simulation

10kHz. Hence much larger distortion is generated. This fact can be also observed in zero-sequence current and torque ripple waveforms in Figure 3.10. In linear MPC methods, a switching frequency ripple can be observed in zero-sequence current and torque ripple, but in non-linear MPC methods, the frequency of the ripple is less than the sampling frequency. Hence the magnitude of zero-sequence current and torque ripple of non-linear MPC methods is larger than of linear MPC methods. Also it can be observed that non-symmetry with respect to 0 exists in the torque ripple in linear MPC methods, which indicates that steady-state errors exist in these methods.

3.4 Experimental Results

Experiments are performed to verify the steady state and transient state responses of the control methods under study. The block diagram of the experimental setup is shown in

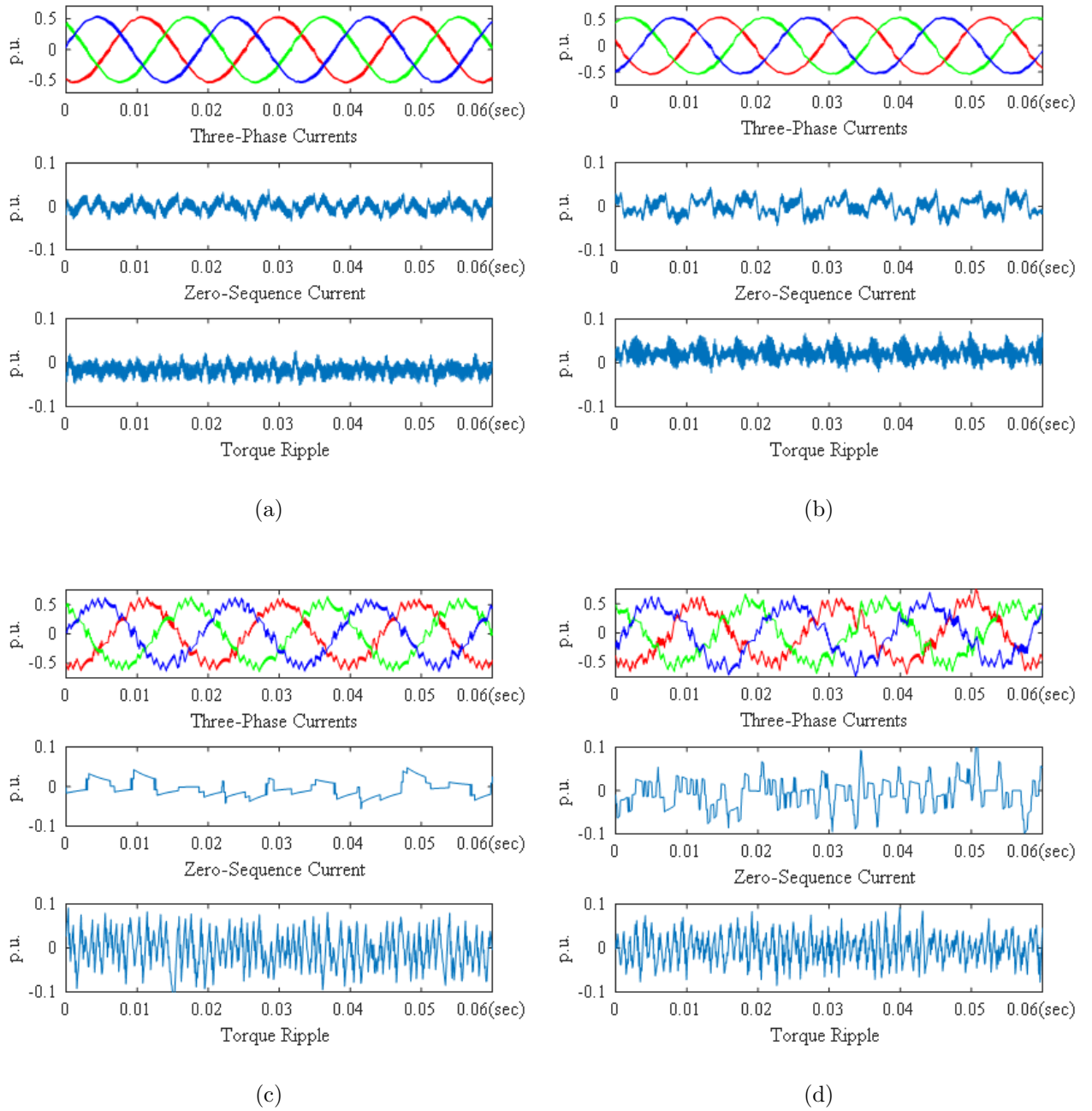


Figure 3.10: Steady State Responses in Simulation

- (a) Linear PCC
- (b) Linear PTC
- (c) Non-Linear PCC
- (d) Non-Linear PTC

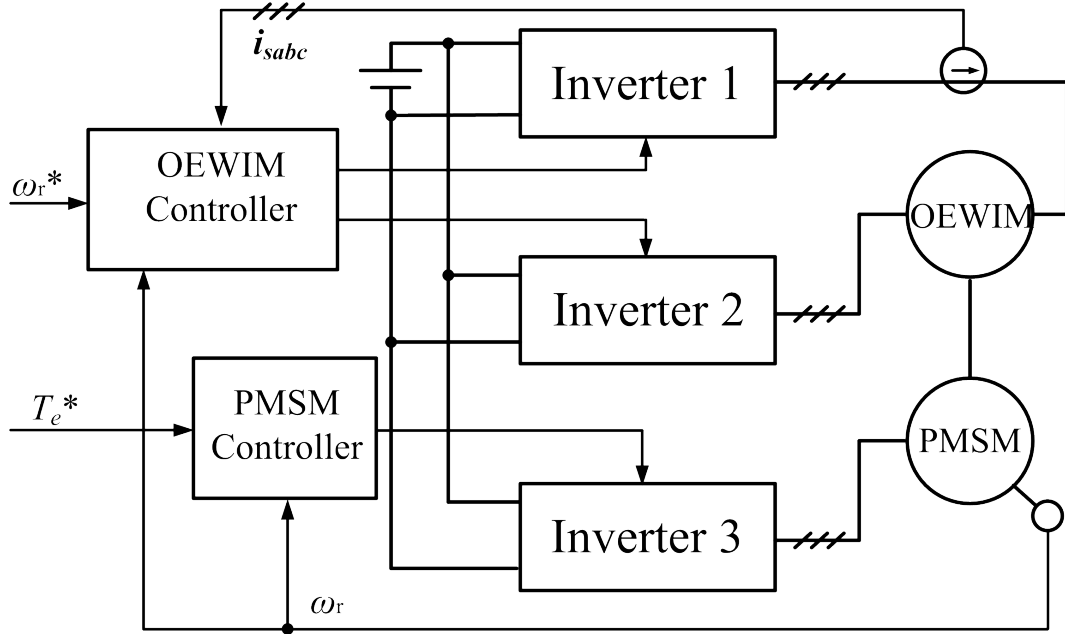


Figure 3.11: Block Diagram of the Experimental System

Figure 3.11, and the system overview is shown in Figure 3.12 (a). A 4-pole OEWIM is coupled with a permanent magnet synchronous motor (PMSM) used as a load. Two three-phase two-level inverters are used for the OEWIM drive and one three-phase inverter for PMSM drive. The motor parameters of OEWIM are listed in Table 3.1, the inverter and motor specifications are shown in Table 3.2. The rotor position is measured by a 2048-point incremental encoder. A Texas Instrument TMS320F28335 digital signal processor is used as the controller, which is mounted on a self-implemented controller board shown in Figure 3.12 (b). The clock frequency of DSP is 150 MHz, the inner controller sampling frequency is 10kHz. The weighting factors in (3.12) of non-linear PCC are $w_\alpha = w_\beta = w_0 = 1$, the weighting factors in (3.20) of non-linear PTC are set to be $w_{te} = w_\psi = w_0 = 1$.

Table 3.3 lists the time required to finish calculation in each sampling period. It is shown that linear MPC methods require much less computation time than their non-linear counterparts. This is because in linear MPC methods, an exact solution is calculated ((3.10) for linear PCC, (3.17)(3.18) for linear PTC), the calculated voltage vector is compared with a

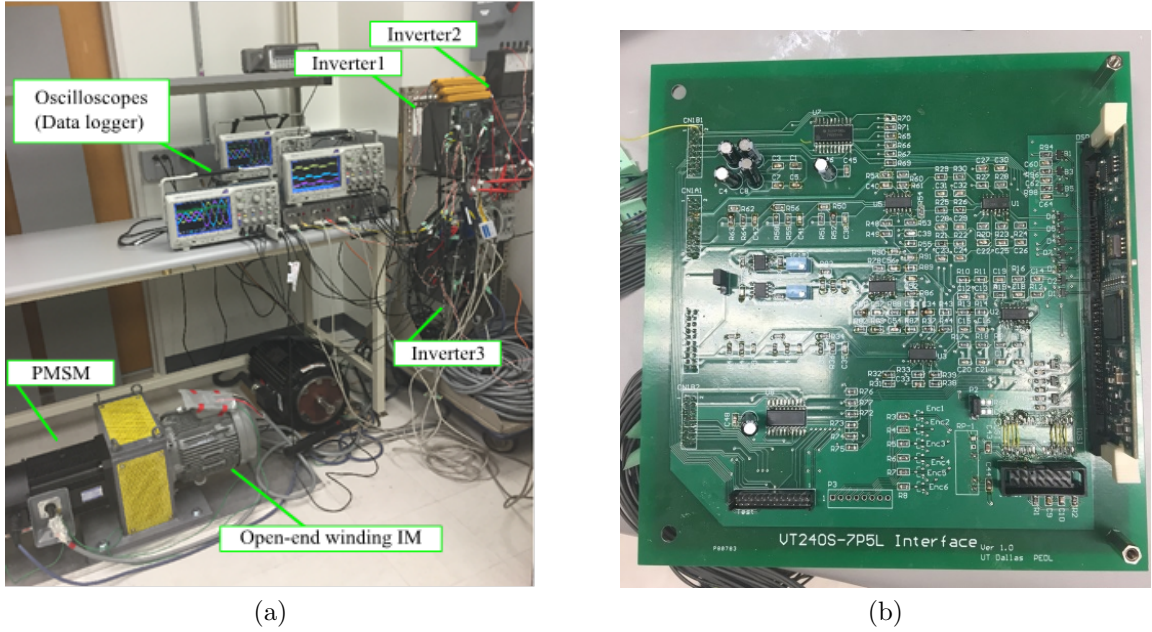


Figure 3.12: Experimental Setup
(a) System Overview
(b) Controller Board

Table 3.2: Inverter and Motor Specifications

Inverters	7.5 kW
OEWIM	5.5 kW, 200 V, 50 Hz, 1470 rpm
PMSM	5.5 kW, 200 V, 50 Hz, 1500 rpm

triangular carrier to generate the switching signals. The non-linear MPC methods need to evaluate all possible voltage vectors to determine the optimal actuation. In conventional motor drive using single inverter, the controller only needs to evaluate 7 voltage vectors for two control variables ($i_{s\alpha}, i_{s\beta}$ or $|\psi_s|, T_e$) during one sampling period, hence the calculation time is still comparable to linear MPC methods as reported in [64]; but the controller for open-end winding motor needs to evaluate 27 voltage vectors for three control variables ($i_{s\alpha}, i_{s\beta}, i_{s0}$ or $|\psi_s|, T_e, i_{s0}$) during one sampling period. Hence, the computation time increases exponentially due to the increase of number of voltage vectors and control variables [34]. As a result, the controller in open-end winding motor drive needs much longer calculation time

Table 3.3: Computation Time Comparison

Linear PCC	13.09 μs
Non-linear PCC	38.61 μs
Linear PTC	16.35 μs
Non-linear PTC	77.81 μs

to determine the optimal switching pattern, in turn limits the sampling frequency of the controller. Also, non-linear PTC presents the heaviest computation burden among all the control methods being compared. The reason for this can be found in Section 3.2.2. In non-linear PCC, only equation (3.9) is used in the searching loop; but in non-linear PTC, equation (3.15), (3.16), and (3.20) must be used in the searching loop. Hence the computation time for non-linear PTC is much longer than non-linear PCC. This result is in accordance with the analysis in [64]. To make a fair comparison, the switching frequency of each control method should be kept the same. But the sampling frequencies and switching frequencies of non-linear MPC methods are restricted by their computation time. Hence in this study, the sampling frequencies of all the methods are kept the same to ensure same hardware resource utilization.

3.4.1 Steady State Operation

To evaluate the performances in steady state, two tests are performed, the OEWIM is first running at 0.3 pu speed (447 rpm) and with no load, then the OEWIM is controlled at 1.0 pu speed and under 0.8 pu load. The steady state responses are shown in Figure 3.13.

It can be observed that under 0.3 pu speed with no load, the linear MPC methods can suppress the zero-sequence current to almost zero. However, zero-sequence currents are still observed in non-linear MPC methods. This phenomenon matches with the analysis in Section 2.2.2. At 0.3 pu speed with no load, the voltage vector to be applied to the inverters lies in the inner hexagon (ABCDEF in Figure 2.4) of the three-level structure, by using PWM and

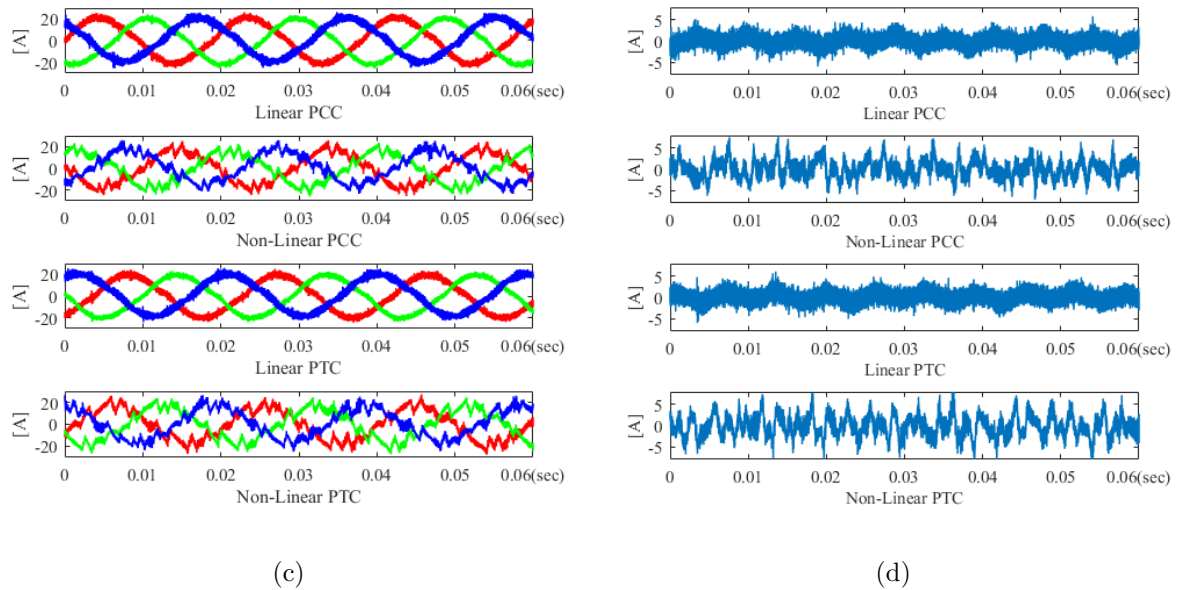
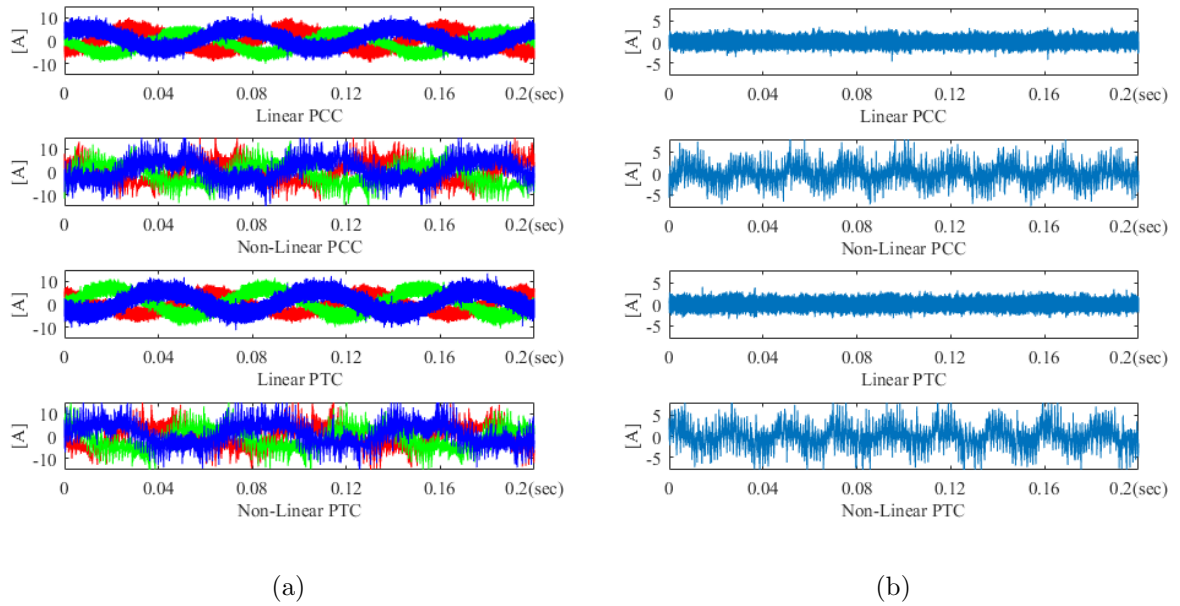


Figure 3.13: Steady State responses in Experiment
 (a) Three-Phase Currents at 0.3 pu speed under no load
 (b) Zero-Sequence Current at 0.3 pu speed under no load
 (c) Three-Phase Currents at 1.0 pu speed under 0.8 pu load
 (d) Zero-Sequence Current at 1.0 pu speed under 0.8 pu load

Table 3.4: Steady State Current THDs

Linear PCC	6.23%
Non-linear PCC	18.13%
Linear PTC	6.76%
Non-linear PTC	22.42%

proper dead-time compensation, the controller can ensure that the output voltage vector lies on the plane $v_{s0} = 0$. As a result, the zero-sequence voltage is controlled to close to zero level. However, for non-linear MPC methods, the inverters can only output discrete voltage vectors during the sampling period, hence the zero-sequence current can be only suppressed using alternative selecting of voltage vectors with opposite zero-sequence components. Also, due to the variable switching frequency, the switching dead-time cannot be compensated. Therefore the zero-sequence current is still observed even during the low modulation region.

Figure 3.13 (c) and Figure 3.13 (d) present the steady state response under 1.0 pu speed (1470 rpm) and 0.8 pu load. The current THDs are listed in Table 3.4. Among the control methods being compared, linear MPC methods provide stronger zero-sequence current suppression and lower current THD than their non-linear counterparts. In this situation, the output voltage vector uses the complete three-level hexagon shown in Figure 2.4. When the output voltage vector lies outside the shaded region, uncontrollable zero-sequence current flows, as shown in Figure 3.13 (d). Also, during the high speed loaded test, the switching frequency of the linear MPC methods is maintained at 20 kHz due to the mandatory switching of PWM, while the non-linear MPC methods enter into six-step operating range, which further reduced the switching frequency and increased the zero-sequence current.

Figure 3.14 shows the FFT spectrum of one phase current under linear and non-linear MPC methods. As the PWM carrier frequency in linear MPC methods is the same with sampling frequency, which is 10 kHz, the effective switching frequency of linear MPC methods is 20 kHz due to the interleaving switching of the two inverters. From Figure 3.14 (a) and (c),

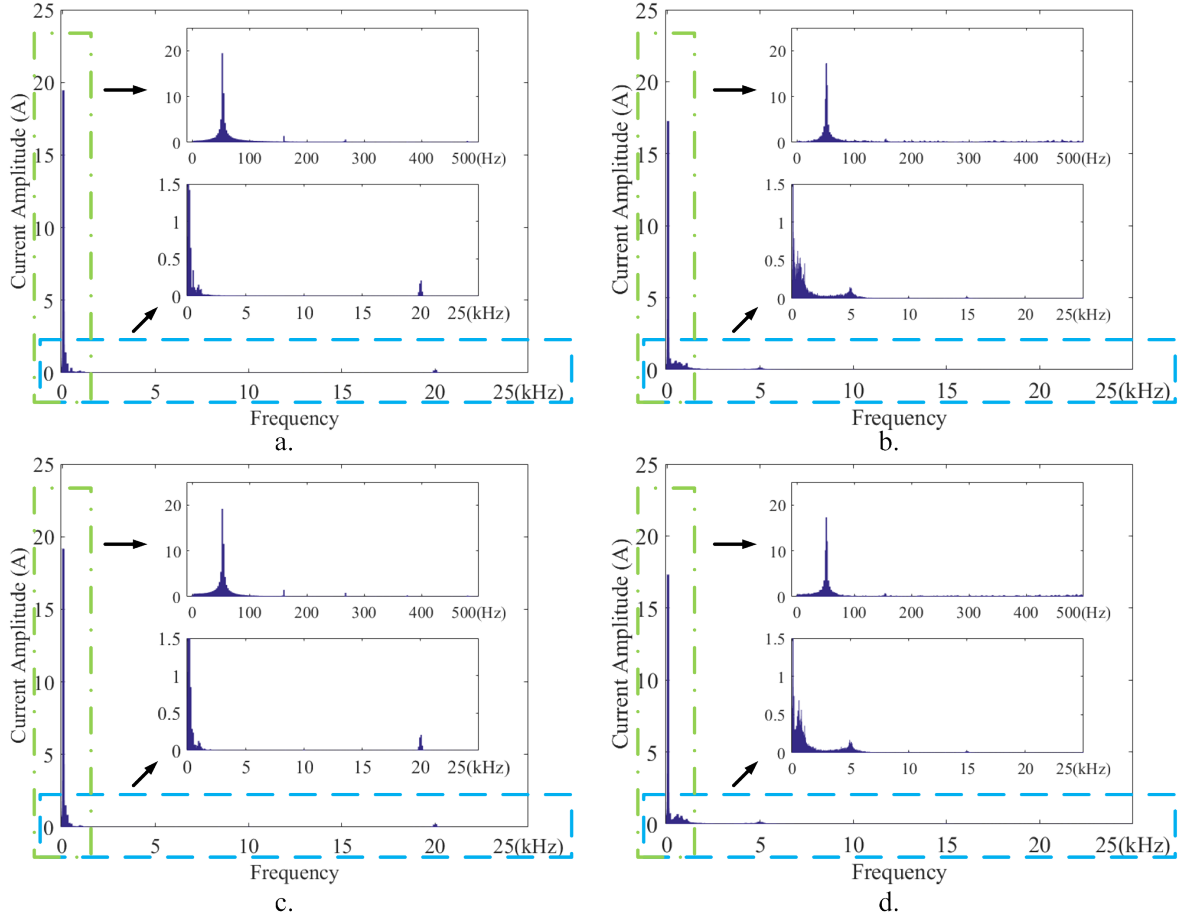


Figure 3.14: FFT Spectrum of One Phase Current
 (a) Linear PCC (b) Non-Linear PCC
 (c) Linear PTC (d) Non-Linear PTC

high frequency components can be observed at 20 kHz in the spectrum. However, no such components are observed in Figure 3.14 (b) and (d). due to the variable switching frequency of non-linear MPC methods. In the low frequency band, the fundamental component can be observed at 50Hz, and the zero-sequence component can be observed at 150Hz. The magnitudes of fundamental components under non-linear MPC methods are found lower than those under linear MPC methods. This is mainly due to the steady state error under non-linear MPC methods. It can be noticed that more low frequency harmonics are presented

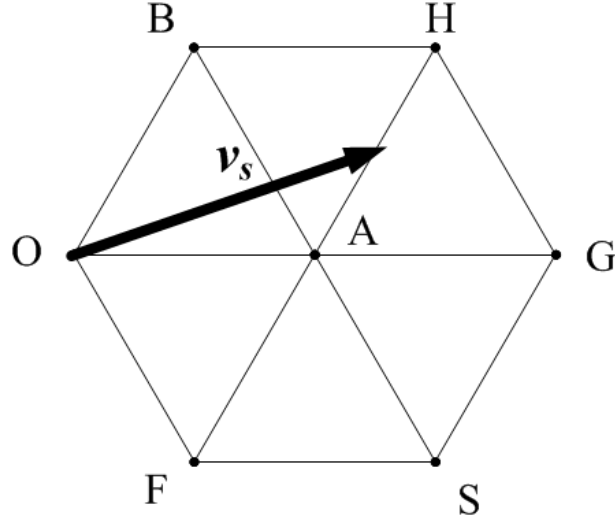


Figure 3.15: Voltage Vector Selection in MPC Methods

under non-linear MPC methods. This phenomenon can be explained by the lower switching frequency of non-linear MPC methods compared with those of linear MPC methods.

One difference between linear and non-linear MPC methods should be noticed from Figure 3.14, that is the switching frequency components of the compared methods. From Figure 3.14 (c) and (d), the switching frequency components of non-linear locate at 5 kHz, which is half of the sampling frequency. This phenomenon can be understood by looking at Figure 3.15, which is a zoom view of Figure 2.4. Assume at time instant k , the location of the output voltage vector v_s is shown in Figure 3.15. Since only discrete switching states can be output from non-linear MPC methods, either switching state A or H is applied to the inverters. Due to the fact that the sampling frequency is much higher than the fundamental frequency, switching states A and H are selected alternately throughout multiple sampling periods until v_s moves to a new location, and a new balance is found through the cost function. Because of the sampling and switching are synchronized in non-linear MPC, the average switching frequency is half of the sampling frequency. And in the high speed/load range, the inverters enter into six-step operation, the switching frequency of non-linear MPC is further reduced. As a result, the switching frequency components of non-linear MPC concentrate within the

range lower than half of the sampling frequency, as shown in Figure 3.14 (c) and (d). In contrast, due to the mandatory switching of the PWM and the interleaved switching of the two inverters, the switching frequency components of linear MPC locate exactly at 20 kHz, which is two times the sampling frequency.

Therefore, with the same sampling frequency, the switching frequency of linear MPC is more than 4 times higher than that of non-linear MPC in open-end winding configuration. In order to achieve comparable switching frequency, the controller clock of non-linear MPC is required to be 4 times faster than that of linear MPC.

3.4.2 Transient State Operation

The transient state responses are evaluated over the full speed range. A 1.0 pu to -1.0 pu speed reversal is performed. The phase A current and zero-sequence current under each control method are shown in Figure 3.16 and Figure 3.17 respectively. It is shown in Figure 3.16 that although all the methods present similar response time during the speed reversal, linear MPC methods have less current ripples than their non-linear counterparts. Besides, linear MPC methods also provide stronger zero-sequence current suppression during transient state, as shown in Figure 3.17.

To understand this phenomenon, one needs to consider the weighting factors in (3.12) and (3.20). Unlike the balanced wye-connected induction motor used in [64], the zero-sequence current due to the DC-link sharing adds an additional complexity to the control design process under the open-end winding configuration. In [64], the weighting factors of non-linear PCC are fixed, and only one weighting factor needs to be tuned in non-linear PTC. However, in the system studied in this paper, the weighting factor of zero-sequence current always needs to be tuned. There is a trade-off between the zero-sequence current suppression and system performance. As studied in [51], in the 27 voltage vectors in open-end winding configuration, there are 7 voltage vectors which do not generate zero-sequence

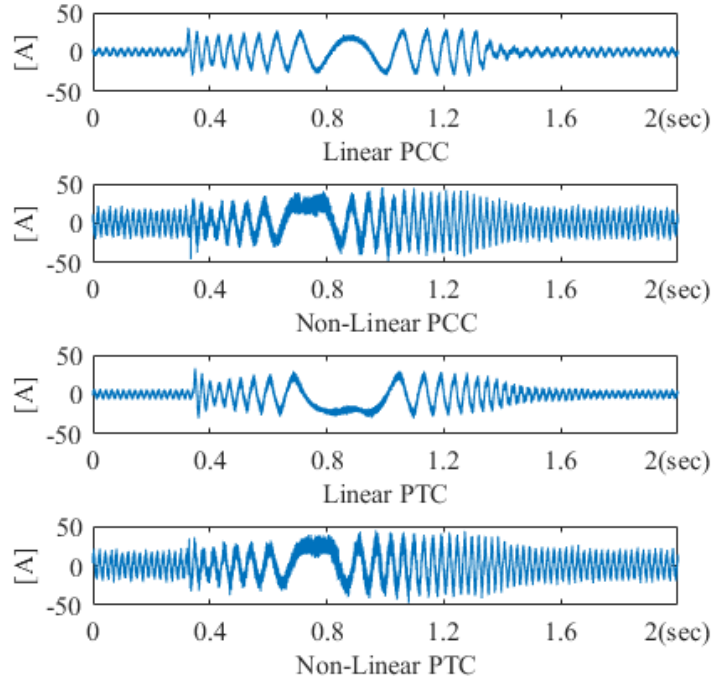


Figure 3.16: Transient State A Phase Current in Experiment

voltages hence do not produce any zero-sequence current. If the weighting factor of zero-sequence current is larger than the other weighting factors, these 7 voltage vectors will be selected more frequently, which result in less zero-sequence current but weaker tracking on the other two control variables, hence larger current ripples and larger steady state errors are produced. If the weighting factor of zero-sequence current is less than the other weighting factors, the other 20 zero-sequence-current-producing voltage vectors will be chosen more frequently, so that the zero-sequence current is increased. And due to the dead-time and current zero-crossing effect, the zero-sequence current will not be totally eliminated even if zero-sequence-current-producing voltage vectors are selected. Hence in the open-end winding configuration, the weighting factor tuning process is much complicated and time consuming comparing to the balanced wye-connected motor case.

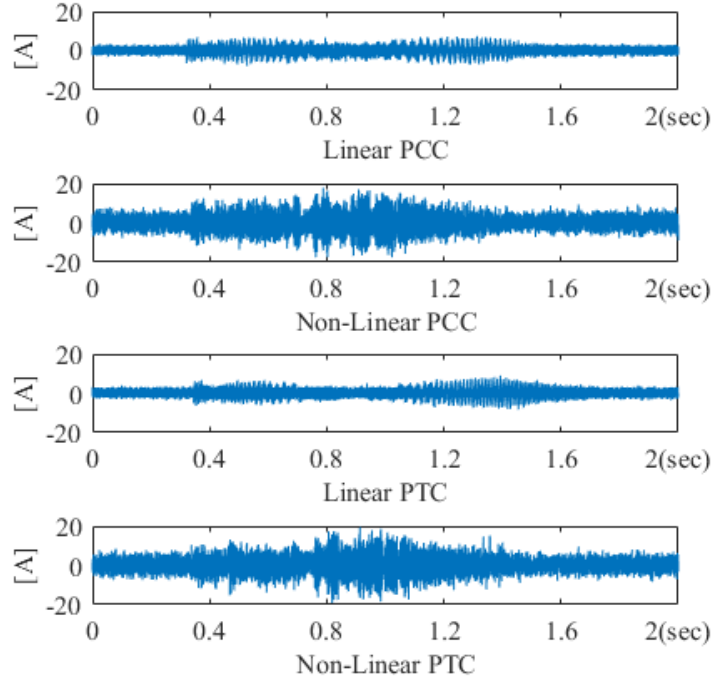


Figure 3.17: Transient State Zero-Sequence Current in Experiment

3.5 Summary

In this chapter, four fast response MPC methods, i.e., linear PCC, non-linear PCC, linear PTC and non-linear PTC are proposed for open-end winding induction motor. For the zero-sequence current presented in open-end winding configuration, the proposed methods either use deadbeat control law, or cost functions, to provide sufficient suppression. The steady state and transient state responses of proposed methods are evaluated in simulation and experiment. The simulated results show that the proposed methods have higher bandwidth, hence faster responses, than conventional FOC-PI method. And in the experimental comparison among the four proposed methods, non-linear MPC methods present longer computation time than linear MPC methods. Under the same sampling frequency, linear MPC

can provide stronger zero-sequence current suppression and smaller current distortion than non-linear MPC methods.

CHAPTER 4

COMPUTATIONALLY EFFICIENT PREDICTIVE CURRENT CONTROL FOR OPEN-END WINDING INDUCTION MOTORS ^{1,2}

In automotive testing systems, high switching frequency is required to improve system response and to reduce current/torque ripples. In conventional MPC methods, the switching frequency is constrained by its enormous calculation time [52], hence computation-efficient MPC methods are urged. In this chapter, two MPC methods are proposed [68, 69]. The proposed methods are evaluated in simulation and verified in experiment. The experimental results show that the proposed methods reduce the calculation time effectively while maintain fast dynamic responses and enhanced zero-sequence current suppression.

4.1 Introduction

Although MPC has many advantages over the conventional control methods, such as fast dynamic response, easy inclusion of system non-linearities and constraints, one major problem of MPC is the heavy computation burden. Due to the large calculation time, the successful commercializations of MPC on drive applications are still limited to the systems with low switching frequencies [70–72]. For higher frequency applications, digital processors with higher clock frequency or FPGA are used to increase the computation power [73–75], which in turn adds additional cost and extra engineering efforts to the overall system.

Depending on topologies of converters and the MPC methods being used, the computation time is mainly contributed from two aspects [72]. The first one is the topology of the

¹©2017 IEEE. Portion Adapted, with permission, from B. Zhu, K. Rajashekara and H. Kubo, "A novel predictive current control for open-end winding induction motor drive with reduced computation burden and enhanced zero sequence current suppression", Applied Power Electronics Conference and Exposition (APEC), 2017 IEEE

²©2017 IEEE. Portion Adapted, with permission, from B. Zhu, K. Rajashekara and H. Kubo, "A Three-Dimensional Predictive Current Trajectory Control Method for Open-End Winding Induction Motor", Energy Conversion Congress and Exposition (ECCE), 2017 ECCE

converter, or the number of voltage levels available. For two-level voltage source inverters (2L-VSI), 7 voltage vectors need to be evaluated during each sampling period; for neutral-point clamped inverters, 3 voltage levels are available, and 27 switching states need to be considered. As the number of voltage levels increases, the number of evaluations also grows exponentially. Hence the computation time is greatly increased. Another cause of longer calculation time is the selection of prediction horizon. As longer switching horizons effectively improve the system performance by reduce the switching losses and lower the current/torque THD [76], it also results in a combinatorial explosion of the number of admissible switching sequences to be assessed. A direct method to determine the optimal switching sequence is to enumerate all the possible switching sequences and select the optimal one. Although this method is conceptually easy, it is computationally expensive, and thus prohibited for long switching horizons. As a result, MPC methods can be only implemented on hardware with constrained switching horizons [77].

Due to the above mentioned facts, researchers have endeavored to optimize the computation efficiency during the last decades. Methods have been proposed and implemented to reduce the calculation time required by MPC [72, 78–85]. A branch and bound algorithm is applied to reduce long-horizon computation burden in [72]. In [78], a sector distribution method to exclude sub-optimal candidate vectors during the prediction process is described. A modified switching algorithm is proposed in [79]. Other techniques such as single-vector based approach [80], double-vector approach [81], and graphical method [82] also present effective calculation time reduction. Also, [81, 83, 84] have explored the possibilities of controlling different variables on various systems. [83] presents a current control approach on 2L-VSI, [84] illustrates a flux/torque control method on NPC converter, and [81] uses active and reactive power to control a doubly-fed induction generator.

In the aforementioned literatures, only two control variables have been considered, and the system is three-phase balanced. In the open-end winding configuration studied in this

dissertation, the three-phase balance is absent and an additional zero-sequence current needs to be suppressed. The control algorithms referred may not work when the number of control variables increases. Therefore, new control methods are required to address the three-phase unbalance, to suppress the zero-sequence current, as well as to reduce the computation burden. In this chapter, two computation-efficient MPC methods, i.e., predictive current control in A-B-C frame (PCC-ABC) [68] and three-dimensional predictive current trajectory control (3DPCTC) [69], are proposed. Compared with conventional MPC methods, the proposed methods significantly reduce the calculation time, present more stable dynamic responses, and provide enhanced zero-sequence current suppression.

4.2 Predictive Current Control in A-B-C Frame (PCC-ABC)

In this section, a predictive current control method based on A-B-C frame, without using cost function, for open-end winding induction motor drive is presented. The experimental results show that the proposed method reduces the computation time by 61.05% compared with conventional predictive current control method. It also reduces zero-sequence current and provides faster dynamic response.

4.2.1 System Model

In open-end winding induction motor fed by two inverters with common DC source shown in Figure 4.1, the electrical model in the stationary frame is given by (4.1) to (4.5):

$$\mathbf{v}_s = \mathbf{R}_s \mathbf{i}_s + \frac{d}{dt} \boldsymbol{\psi}_s \quad (4.1)$$

$$\mathbf{0} = \mathbf{R}_r \mathbf{i}_r + \frac{d}{dt} \boldsymbol{\psi}_r - \mathbf{j} \omega_r \boldsymbol{\psi}_r \quad (4.2)$$

$$\boldsymbol{\psi}_s = \mathbf{L}_s \mathbf{i}_s + \mathbf{L}_m \mathbf{i}_r \quad (4.3)$$

$$\boldsymbol{\psi}_r = \mathbf{L}_r \mathbf{i}_r + \mathbf{L}_m \mathbf{i}_s \quad (4.4)$$

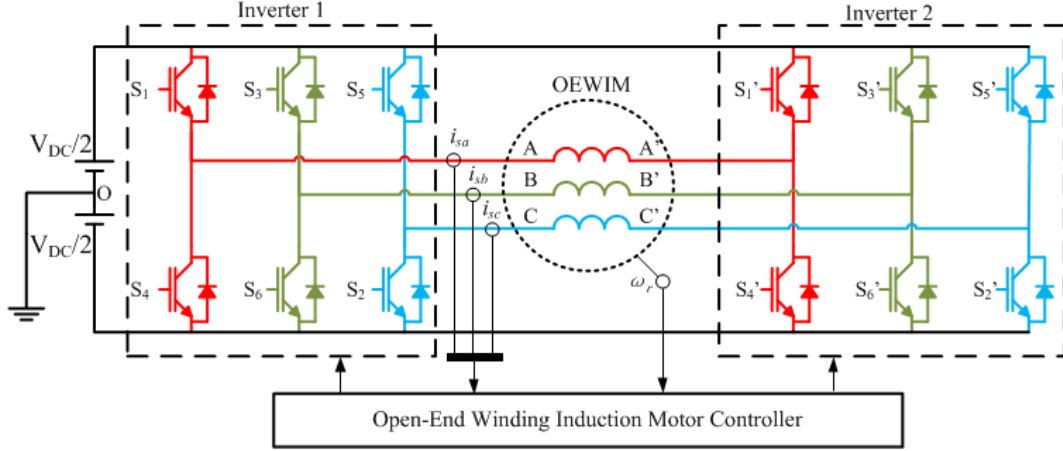


Figure 4.1: An Open-End Winding Induction Motor Drive

$$T_e = \frac{3}{2}P(\psi_{sd}i_{sq} - \psi_{sq}i_{sd}) \quad (4.5)$$

In which $\mathbf{R}_s, \mathbf{R}_r, \mathbf{L}_s, \mathbf{L}_r, \mathbf{L}_m$ are system parameter matrices with zero-sequence components, e.g. $\mathbf{R}_s = \text{diag}[R_s, R_s, R_s]$, $\mathbf{L}_s = \text{diag}[L_s, L_s, L_{ls}]$, $\mathbf{L}_m = \text{diag}[L_m, L_m, 0]$. And $\mathbf{v}_s, \mathbf{i}_s, \mathbf{i}_r, \boldsymbol{\psi}_s, \boldsymbol{\psi}_r$ are state variables with zero-sequence component, e.g. $\mathbf{v}_s = \begin{bmatrix} v_{sd} & v_{sq} & v_{s0} \end{bmatrix}^T$. ω_r is the rotor electrical angular speed, P is number of pole pairs. \mathbf{j} is the coupling matrix which is given as:

$$\mathbf{j} = \begin{bmatrix} 0 & -1 & 0 \\ 1 & 0 & 0 \\ 0 & 0 & 0 \end{bmatrix}$$

From (4.4), the rotor current vector \mathbf{i}_r can be expressed as:

$$\mathbf{i}_r = \frac{\mathbf{I}}{\mathbf{L}_r}(\boldsymbol{\psi}_r - \mathbf{L}_m \mathbf{i}_s) \quad (4.6)$$

Where \mathbf{I} is rank 3 identity matrix. Substitute (4.6) into (4.3), the stator flux vector can be written as:

$$\boldsymbol{\psi}_s = \mathbf{L}_s \mathbf{i}_s + \frac{\mathbf{L}_m}{\mathbf{L}_r}(\boldsymbol{\psi}_r - \mathbf{L}_m \mathbf{i}_s) \quad (4.7)$$

Substitute (4.6) into (4.2), the rotor voltage equation becomes:

$$\frac{d}{dt}\boldsymbol{\psi}_r = -\frac{\mathbf{R}_r}{\mathbf{L}_r}(\boldsymbol{\psi}_r - \mathbf{L}_m \mathbf{i}_s) + \mathbf{j}\omega_r \boldsymbol{\psi}_r \quad (4.8)$$

From (4.1) (4.7) and (4.8), the stator current equation can be obtained:

$$p\mathbf{i}_s = \frac{\mathbf{I}}{\mathbf{L}_s\boldsymbol{\sigma}} \left(\mathbf{v}_s - \mathbf{R}_s\mathbf{i}_s + \frac{\mathbf{L}_m}{\mathbf{L}_r}(\mathbf{R}_r\mathbf{i}_r - \omega_r\mathbf{J}_3\boldsymbol{\psi}_r) \right) \quad (4.9)$$

In which $\boldsymbol{\sigma} = \mathbf{I}_3 - \frac{\mathbf{L}_m^2}{\mathbf{L}_s\mathbf{L}_r}$. Considering all the terms other than \mathbf{v}_s in (4.9) to be the load voltage term, then the load voltage in (4.9) can be written as:

$$\mathbf{v}_l = \mathbf{R}_s\mathbf{i}_s - \frac{\mathbf{L}_m}{\mathbf{L}_r}(\mathbf{R}_r\mathbf{i}_r - \omega_r\mathbf{j}\boldsymbol{\psi}_r) \quad (4.10)$$

Substitute (4.10) into (4.9), the simplified stator current equation can be written as:

$$p\mathbf{i}_s = \frac{\mathbf{I}}{\mathbf{L}_s\boldsymbol{\sigma}}(\mathbf{v}_s - \mathbf{v}_l) \quad (4.11)$$

4.2.2 Flux Estimation

As shown in 4.10), the rotor flux vector $\boldsymbol{\psi}_r$ needs to be estimated. The rotor flux can be estimated using a rotor speed sensor and measured currents from the three-phase windings under the rotating reference frame aligned with rotor winding. And the estimated rotor flux can be written as:

$$\frac{d}{dt}\boldsymbol{\psi}_r = \frac{\mathbf{L}_m}{\boldsymbol{\tau}_r}\mathbf{i}_s - \frac{\mathbf{I}}{\boldsymbol{\tau}_r}\boldsymbol{\psi}_r \quad (4.12)$$

Where $\boldsymbol{\tau}_r = \mathbf{L}_r/\mathbf{R}_r$. Discretize 4.12) within sampling period T_s , the estimated rotor flux $\hat{\boldsymbol{\psi}}_r$ at time instant k can be obtained:

$$\frac{d}{dt}\hat{\boldsymbol{\psi}}_{r,k} = \frac{\mathbf{L}_m T_s}{\boldsymbol{\tau}_r}\mathbf{i}_{s,k-1} + \left(\mathbf{I} - \frac{T_s}{\boldsymbol{\tau}_r}\right)\hat{\boldsymbol{\psi}}_{r,k-1} \quad (4.13)$$

4.2.3 Conventional PCC

In conventional PCC, (4.11) is discretized using Forward Euler method, and the stator current vector can be predicted as:

$$\hat{\mathbf{i}}_{s,k+1} = \mathbf{i}_{s,k} + T_s \frac{\mathbf{I}}{\mathbf{L}_s\boldsymbol{\sigma}}(\mathbf{v}_{s,k} - \mathbf{v}_{l,k}) \quad (4.14)$$

Due to the delay effect described in Section 2.3, an additional extrapolation step is required to compensate the delay. The predicted stator current at time instant $k+2$ can be expressed as:

$$\hat{\mathbf{i}}_{s,k+2} = \mathbf{i}_{s,k+1} + T_s \frac{\mathbf{I}}{\mathbf{L}_s \boldsymbol{\sigma}} (\mathbf{v}_{s,k+1} - \mathbf{v}_{l,k+1}) \quad (4.15)$$

As open-end winding configuration uses two two-level inverters, a total of 64 switching combinations can be mapped onto 27 different voltage vectors [52]. The conventional PCC predicts the resultant current under each voltage vector using the following cost function:

$$g(i) = \left| i_{s\alpha}^* - \hat{i}_{s\alpha,k+2}(i) \right| + \left| i_{s\beta}^* - \hat{i}_{s\beta,k+2}(i) \right| + w_0 \left| \hat{i}_{s0,k+2}(i) \right| \quad (4.16)$$

Where w_0 is the weighting factor of current error in zero axis. From (4.16), the voltage vector to be applied on the converters can be obtained as:

$$\mathbf{v}_{opt,k+1} = \arg \min_{\{i=1,2,\dots,27\}} g(i) \quad (4.17)$$

Unlike the wye-connected motor fed by single inverter where the controller only needs to evaluate 7 voltage vectors for two control variables ($i_{s\alpha}, i_{s\beta}$) during one sampling period [64], the controller for open-end winding motor needs to evaluate 27 voltage vectors for three control variables ($i_{s\alpha}, i_{s\beta}, i_{s0}$) during one sampling period. As number of control variables increases, the computation time increases exponentially with number of voltage vectors to be evaluated [67], hence the controller has very limited time for computation in open-end winding configuration.

On the other hand, for a balanced wye-connected induction motor, the two control variables ($i_{s\alpha}, i_{s\beta}$) are equally weighted [64]. However, for OEWIM, to address the suppression effect of the zero-sequence current, the weighting factor w_0 needs to be tuned. As there are 7 out of 27 voltage vectors which do not generate any zero-sequence voltage, they are selected more frequently by the cost function if w_0 increases, which in turn results in larger errors in $i_{s\alpha}$ and $i_{s\beta}$. When w_0 decreases, although errors in $i_{s\alpha}$ and $i_{s\beta}$ are reduced, the zero-sequence

current increases. A proper weighting factor w_0 is required to minimize the overall steady state error. Hence, finding such a w_0 can add more complexity to the design process for the PCC on OEWM.

4.2.4 Proposed PCC-ABC

With the common DC-link configuration for OEWM, the two inverters can also be regarded as three H-bridges, as highlighted in Figure 4.1. Therefore, each phase winding of the OEWM can be controlled through the H-bridge independently from the other two phases. This is a unique advantage of open-end winding configuration with one DC source. From (4.11), the stator voltage equation can be written as:

$$\mathbf{v}_s = \mathbf{L}_s \sigma p \mathbf{i}_s + \mathbf{v}_l \quad (4.18)$$

In which p is the derivative operand.

To transform the above equation to A-B-C frame, one can use Clarke transformation. Assume \mathbf{C} is the transformation matrix from A-B-C frame to α - β -0 frame, and \mathbf{C}^{-1} is the transformation matrix from α - β -0 frame to A-B-C frame, the transformation on (4.18) results in:

$$\mathbf{C}^{-1} \mathbf{v}_s = \mathbf{C}^{-1} \mathbf{L}_s \sigma p \mathbf{C} \mathbf{C}^{-1} \mathbf{i}_s + \mathbf{C}^{-1} \mathbf{v}_l \quad (4.19)$$

The stator voltage equation in A-B-C frame then can be expressed as:

$$\mathbf{v}_{sabc} = \mathbf{C}^{-1} \mathbf{L}_s \sigma p \mathbf{C} \mathbf{i}_{sabc} + \mathbf{v}_{labc} \quad (4.20)$$

The $\mathbf{C}^{-1} \mathbf{L}_s \sigma p \mathbf{C}$ tern in (4.20) can be written in matrix form as:

$$\mathbf{C}^{-1} \mathbf{L}_s \sigma p \mathbf{C} = \begin{bmatrix} \frac{2L_s \sigma p}{3} + \frac{L_{ls} p}{3} & \frac{L_{ls} p}{3} - \frac{L_s \sigma p}{3} & \frac{L_{ls} p}{3} - \frac{L_s \sigma p}{3} \\ \frac{L_{ls} p}{3} - \frac{L_s \sigma p}{3} & \frac{2L_s \sigma p}{3} + \frac{L_{ls} p}{3} & \frac{L_{ls} p}{3} - \frac{L_s \sigma p}{3} \\ \frac{L_{ls} p}{3} - \frac{L_s \sigma p}{3} & \frac{L_{ls} p}{3} - \frac{L_s \sigma p}{3} & \frac{2L_s \sigma p}{3} + \frac{L_{ls} p}{3} \end{bmatrix} \quad (4.21)$$

Knowing that the zero sequence current is defined as:

$$i_{s0} = \frac{1}{3}(i_{sa} + i_{sb} + i_{sc}) \quad (4.22)$$

Then (4.21) can be re-written as:

$$\mathbf{C}^{-1}\mathbf{L}_s\sigma p\mathbf{C} = \begin{bmatrix} L_s\sigma p & & \\ & L_s\sigma p & \\ & & L_s\sigma p \end{bmatrix} + \frac{(L_{ls} - L_s\sigma)p}{3} \begin{bmatrix} 1 & 1 & 1 \\ 1 & 1 & 1 \\ 1 & 1 & 1 \end{bmatrix} \quad (4.23)$$

Sustitute (4.23) into (4.20), it can be obtained:

$$\begin{bmatrix} v_{sa} \\ v_{sb} \\ v_{sc} \end{bmatrix} = L_s\sigma p \begin{bmatrix} i_{sa} \\ i_{sb} \\ i_{sc} \end{bmatrix} + \begin{bmatrix} v_{la} \\ v_{lb} \\ v_{lc} \end{bmatrix} + (L_{ls} - L_s\sigma)p \begin{bmatrix} i_{s0} \\ i_{s0} \\ i_{s0} \end{bmatrix} \quad (4.24)$$

Discretize (4.24) using forward Euler method, the predicted currents under $A - B - C$ frame can be written as:

$$\begin{bmatrix} \dot{i}_{sa,k+1} \\ \dot{i}_{sb,k+1} \\ \dot{i}_{sc,k+1} \end{bmatrix} = \frac{T_s}{L_s\sigma} \left(\begin{bmatrix} v_{sa,k} \\ v_{sb,k} \\ v_{sc,k} \end{bmatrix} - \begin{bmatrix} v_{la,k} \\ v_{lb,k} \\ v_{lc,k} \end{bmatrix} \right) + \begin{bmatrix} \dot{i}_{sa,k} \\ \dot{i}_{sb,k} \\ \dot{i}_{sc,k} \end{bmatrix} + \frac{L_{ls} - L_s\sigma}{L_s\sigma} \begin{bmatrix} i_{s0,k} \\ i_{s0,k} \\ i_{s0,k} \end{bmatrix} \quad (4.25)$$

Due to the calculation delay of the digital controller and the zero-order-hold nature of power converters, one more step extrapolation is required to compensate the delay described in Section 2.3. Hence the stator three-phase currents at time instant $k + 2$ can be predicted as:

$$\begin{bmatrix} i_{sa,k+2}(i) \\ i_{sb,k+2}(i) \\ i_{sc,k+2}(i) \end{bmatrix} = \frac{T_s}{L_s\sigma} \left(\begin{bmatrix} v_{sa,k+1}(i) \\ v_{sb,k+1}(i) \\ v_{sc,k+1}(i) \end{bmatrix} - \begin{bmatrix} v_{la,k+1} \\ v_{lb,k+1} \\ v_{lc,k+1} \end{bmatrix} \right) + \begin{bmatrix} \dot{i}_{sa,k+1} \\ \dot{i}_{sb,k+1} \\ \dot{i}_{sc,k+1} \end{bmatrix} + \frac{L_{ls} - L_s\sigma}{L_s\sigma} \begin{bmatrix} i_{s0,k+1} \\ i_{s0,k+1} \\ i_{s0,k+1} \end{bmatrix} \quad (4.26)$$

Where T_s is the sampling period, i varies from 1 to 3, which represent the three possible voltages to be applied to each phase winding, i.e., $v_{sa,k+1}(i)$ can be $+V_{DC}, 0, -V_{DC}$. And the

Table 4.1: Motor Ratings and Parameters

Power(kW)	5.5
Poles	4
Rating Speed (rpm)	1470
Line to Line Voltage (V)	200
Stator Resistance ($m\Omega$)	834
Rotor Resistance ($m\Omega$)	654
Stator Leakage Inductance (mH)	3.2
Rotor Leakage Inductance (mH)	3.2
Mutual Inductance (mH)	138.1

cost function in (4.16) becomes three independent optimization functions which predict the error between the reference and predicted current in three phases, and they share the same form as:

$$g_a(i) = \left| i_a^* - i_{sa,k+2}(i) \right| \quad (4.27)$$

It is shown that no weighting factor is required in (4.27), since each phase is controlled independently. The voltage ($+V_{DC}$ or 0 or $-V_{DC}$) which minimizes $g(i)$ in (4.16) will be applied to each phase. In this way, the controller only needs to evaluate 3 possible voltages for one phase, and repeating this evaluation for the other two phases results in a total of 9 evaluations to find the optimal switching pattern. Comparing with evaluating 27 voltage vectors in one sampling period using conventional PCC, the calculation time of the proposed method is reduced by 66.7%, and the weighting factors in the cost functions are also eliminated.

4.2.5 Simulation Results

To verify the optimization effect of conventional PCC and proposed PCC-ABC method, simulation is performed using Matlab/Simulink software. The block diagram of the controller used in both simulation and experiment is shown in Figure 4.2. The motor parameters are listed in Table 4.1. The PWM carrier frequency is 10 kHz, and the sampling frequency of the controller is set to be 10 kHz. The weighting factor w_0 in (4.16) is chosen to be $w_0 = 1$.

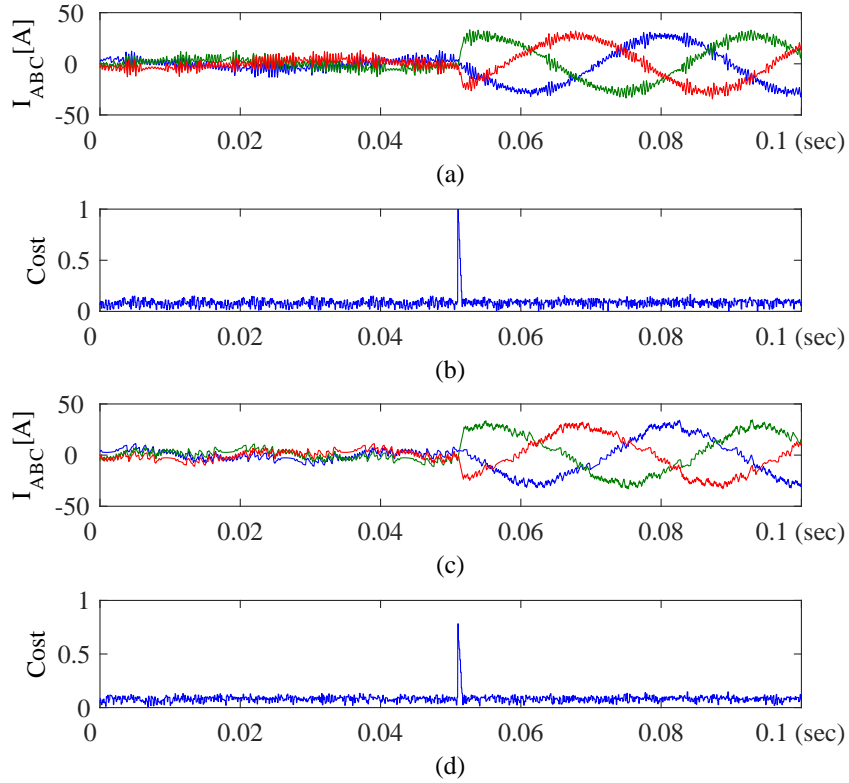


Figure 4.3: Simulation Transient Responses of PCC and PCC-ABC
 (a) Three-Phase Currents of PCC
 (b) Cost of PCC
 (c) Three-Phase Currents of PCC-ABC
 (d) Cost of PCC-ABC

4-pole OEWM is coupled with a permanent magnet synchronous motor (PMSM) used as a load. Two three-phase two-level inverters are used for the OEWM drive and one three-phase inverter for PMSM drive. The inverter and motor specifications are shown in Table 4.2. A quadrature encoder is mounted on the shaft of PMSM, the speed information is sent to both PMSM controller and OEWM controller. A Texas Instrument TMS320F28335 digital signal processor is used as the controller for OEWM with clock frequency 150 MHz and sampling frequency 20 kHz. Both conventional PCC and proposed PCC-ABC are implemented for

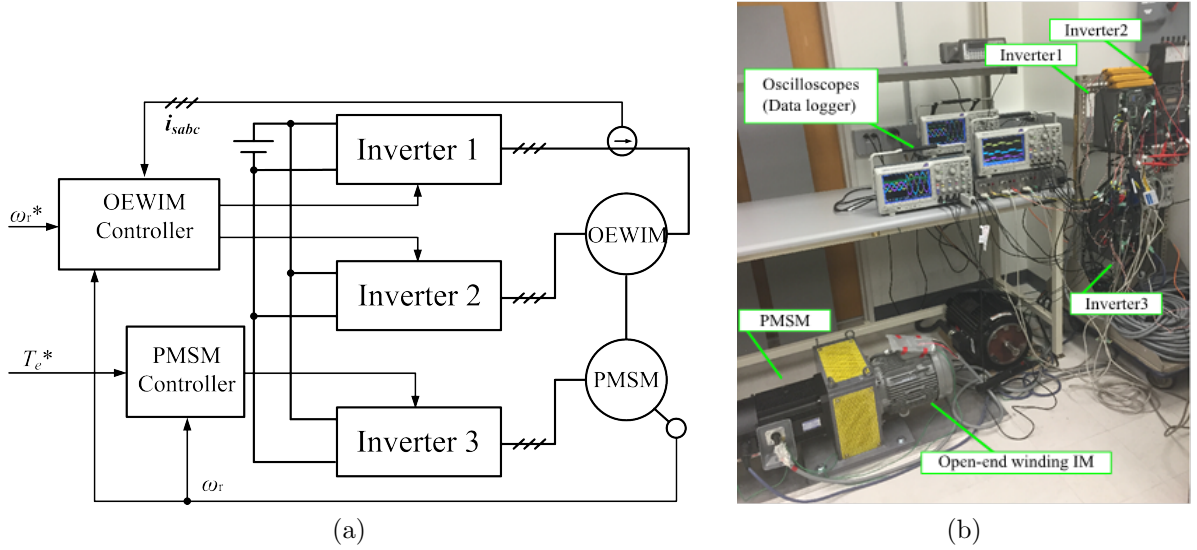


Figure 4.4: Experimental System Setup
(a) Block Diagram
(b) System Overview

Table 4.3: Computation Time Comparison

Conventional PCC	39.46 μs (5919 clock cycles)
PCC-ABC	15.36 μs (2305 clock cycles)

comparison, the weighting factor w_0 in equation (4.16) of conventional PCC is set to be $w_0 = 1$.

Table 4.3 shows the computation time in conventional PCC and proposed PCC-ABC. As the clock frequency of the DSP is 150 MHz and sampling frequency of the controller is 20 kHz, there are 7500 clock cycles within each sampling period. For conventional PCC, it takes 5919 clock cycles, which is 78.92% of the sampling period to finish the calculation. But for proposed PCC-ABC, it takes 2305 clock cycles to finish the calculation. It is shown that the proposed method reduces the computation time by 61.05% compared with conventional PCC. It is also known that the sampling frequency of the controller is limited by the calculation time. With a shorter calculation time, the controller can undertake higher sampling

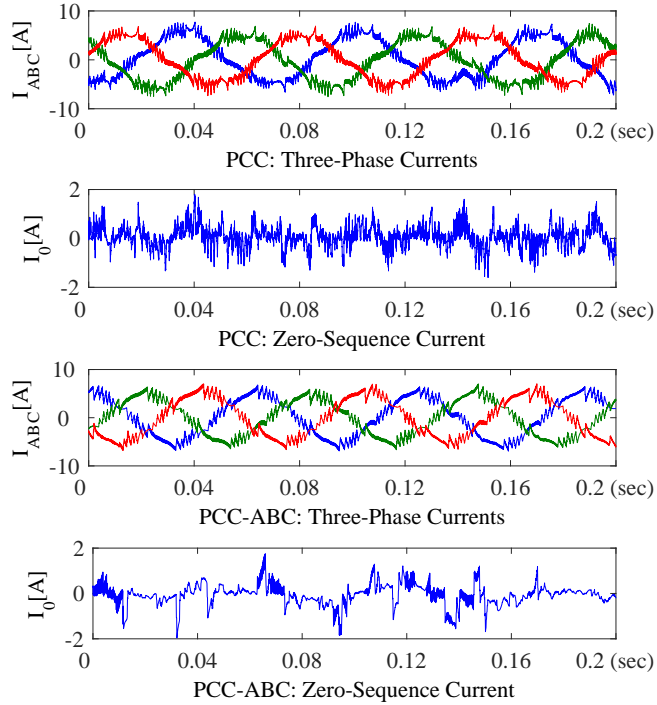


Figure 4.5: Experiment: Steady State Performance at 447 rpm with No Load

frequency which results in higher switching frequency thus less current ripples. With conventional PCC, it is impossible to raise the sampling frequency to more than 20 kHz with a 150 MHz clock. But with proposed PCC-ABC, the sampling frequency of the controller can be further increased, hence the current ripples can be further reduced.

To compare the steady state performance of the OEWIM under conventional PCC and proposed PCC-ABC, the three-phase currents and zero sequence current waveforms are shown in Figure 4.5 to Figure 4.7. When the motor is running at 447 rpm, both conventional PCC and proposed PCC-ABC can provide good zero-sequence current suppression, as shown in Figure 4.5. When the motor speed is increased, the proposed PCC-ABC can still provide good zero-sequence current suppression, while the conventional PCC presents larger errors compared with PCC-ABC, as shown in Figure 4.6 and Figure 4.7 shows the situation when

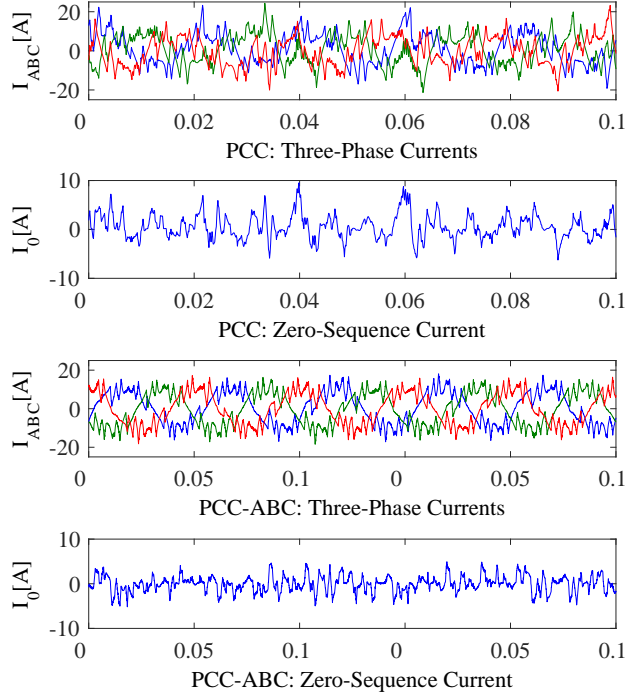


Figure 4.6: Experiment: Steady State Performance at 1470 rpm with No Load

the motor is running at 1470 rpm with 0.8 pu load. It can be observed that the magnitude of zero-sequence current under PCC-ABC is smaller than that under conventional PCC, which means the proposed method can provide stronger zero-sequence current suppression when the motor is under load.

The transient responses of the two methods are shown in Figure 4.8. A 1.0 pu to -1.0 pu speed reversal is performed under both methods. It is shown that the proposed PCC-ABC presents faster transient response than the conventional PCC. During the speed reversal test, current spikes are observed with conventional PCC, which means the cost function (4.16) used in conventional PCC cannot provide an optimal switching vector which can minimize the current errors. Hence it can be inferred that the proposed PCC-ABC can also provide a more stable transient response than conventional PCC.

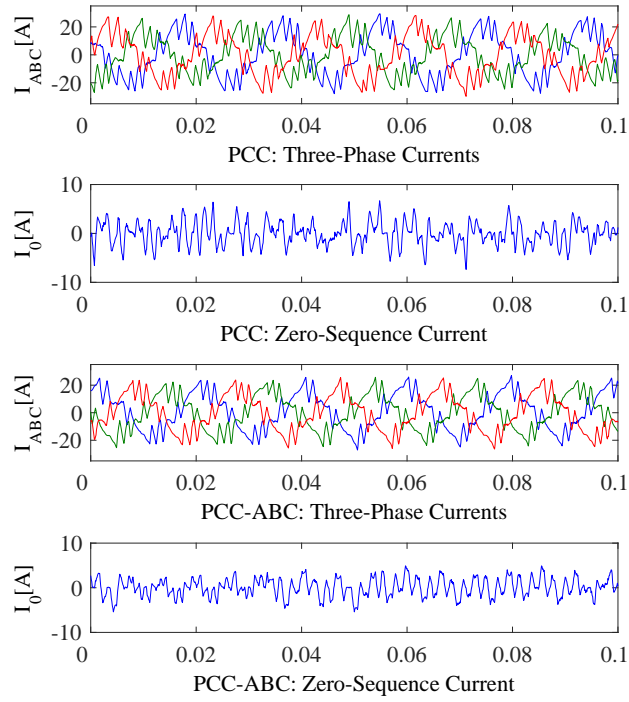


Figure 4.7: Experiment: Steady State Performance at 1470 rpm with 0.8 pu Load

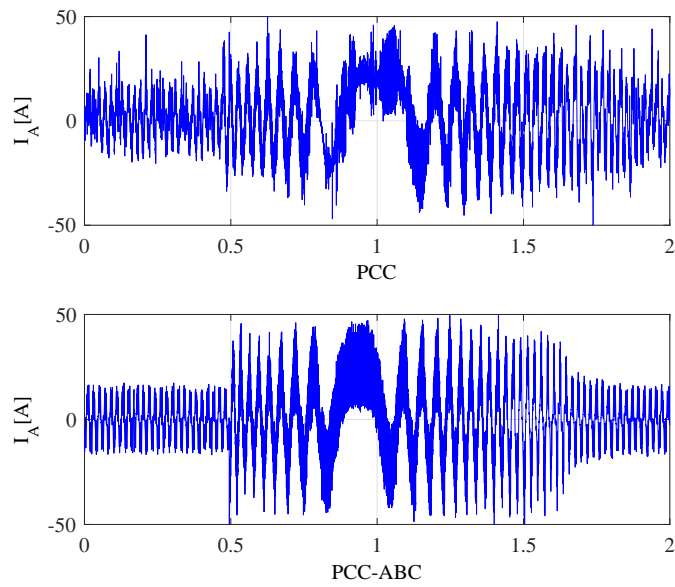


Figure 4.8: Experiment: A Phase Current during Speed Reversal

4.3 Three-Dimensional Predictive Current Trajectory Control (3DPCTC)

As discussed in Section 4.2.3, conventional PCC requires large calculation time to find the optimal voltage to be applied on the inverters. And selecting a proper weighting factor add additional complexity to the design process. In this section, another approach to reduce the computation burden and to improve system performance is proposed. A three-dimensional predictive current trajectory control (3DPCTC) method is presented and evaluated. Compared with conventional predictive control methods, the proposed method significantly reduces calculation burden, and provides stronger zero-sequence current suppression and lower current distortion as well as more stable transient response.

4.3.1 Methodology

In the open-end winding configuration with isolated DC-links, the two inverters can have 64 switching combinations, among which there are 19 different voltage vectors. The α axis and β axis components can be mapped onto a three-level hexagon, as shown in Figure 4.9 (a). For open-end winding configuration sharing one DC-link, the zero-sequence component needs to be considered. Figure 4.9 (b) shows the voltage vectors in a three-dimensional space with the zero-sequence axis orthogonal to the $\alpha\beta$ plane. Among 64 possible switching combinations, there are 27 different voltage vectors, which are marked with circles in Figure 4.9(b). It can be observed that the projections of the 27 voltage vectors form the same three-level hexagon shown in Figure 4.9 (a). However, only seven voltage vectors are located on the plane $v_{s0} = 0$. These seven voltage vectors do not generate any zero-sequence voltage, and they form a shaded intermediate hexagon in Figure 4.9 (a) and (b). Within this shaded hexagon, the zero-sequence current can be suppressed to around close to zero level. The radius of the circle inscribing the shaded hexagon represents the largest magnitude of the voltage vectors which can suppress the zero-sequence current to zero. Apart from the 7 voltage vectors, all the other 20 voltage vectors contain zero-sequence component, and they

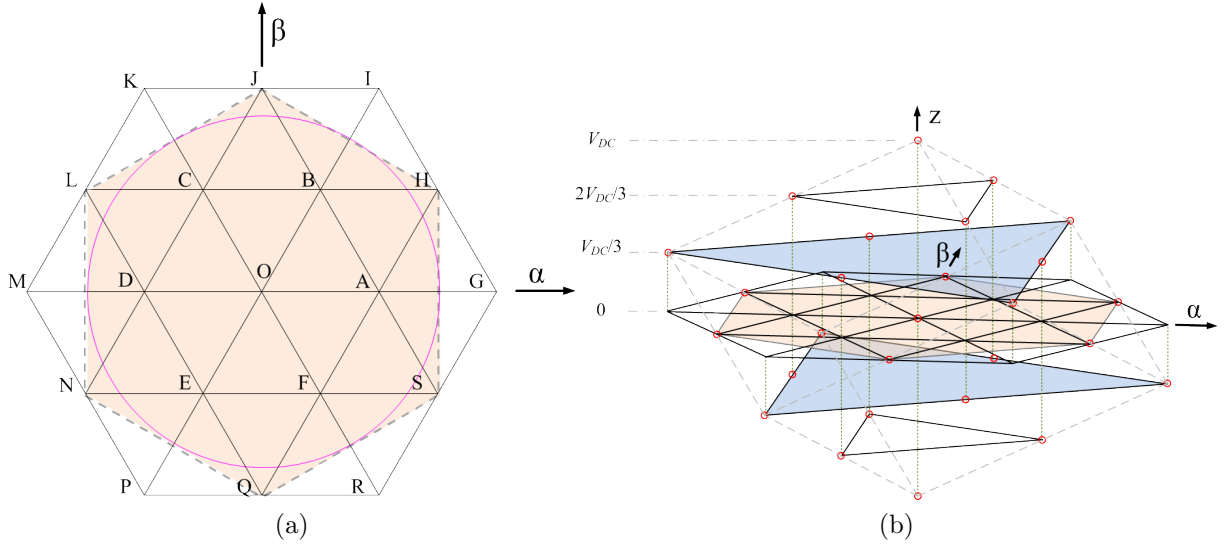


Figure 4.9: (a) Voltage Vectors in Two Dimensional Plane
(b) Voltage Vectors in Three-Dimensional Space

are located on 6 different planes with zero-sequence voltages $\pm\frac{1}{3}V_{DC}$, $\pm\frac{2}{3}V_{DC}$, $\pm V_{DC}$. It can be also noticed that the 27 voltage vectors locate on a cube, which is marked by the dashed lines. The length of each edge of the cube is $2V_{DC}$, which represents the voltage limit. In other words, the two inverters can only generate voltage vectors which locate on the surface of the cube or inside the cube.

In balanced wye-connected motor, the zero-sequence current is always zero, hence the stator current trajectory can be mapped on a two-dimensional plane [64, 86–88]. In open-end winding configuration with one DC-link, there are three variables to be controlled, i.e., $i_{s\alpha}$, $i_{s\beta}$, i_{s0} . As a result, the stator current trajectory of open-end winding induction motor needs to be mapped on a three-dimensional space. Hence the control problem now becomes to find a switching pattern for the two inverters so that the stator current trajectory can track the current reference. From (4.15), the voltage vector to be applied at time instant $k + 1$ can be expressed as:

$$\mathbf{v}_{s,k+1} = \frac{\mathbf{L}_s \boldsymbol{\sigma}}{T_s} (\hat{\mathbf{i}}_{s,k+2} - \mathbf{i}_{s,k+1}) + \mathbf{v}_{l,k+1} \quad (4.28)$$

In order to control the stator current trajectory to track the current reference, one needs to

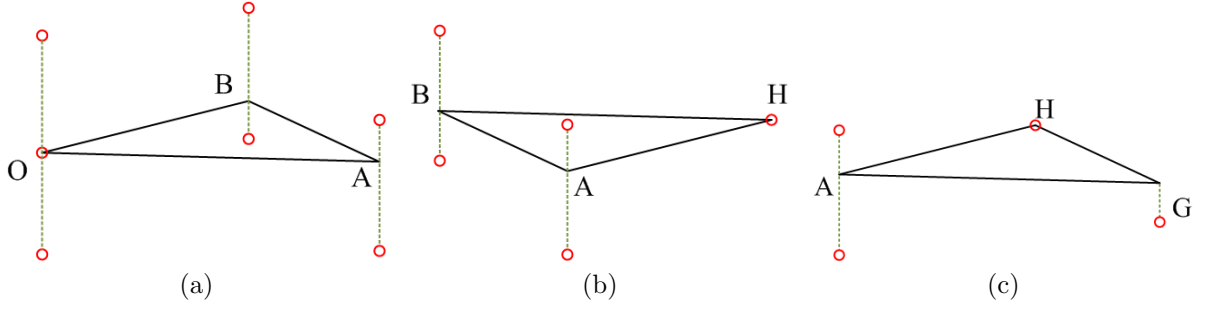


Figure 4.10: Voltage Vectors in:
 (a) Inner Triangle
 (b) Intermediate Triangle
 (c) Outer Triangle

find the voltage vector which is closest to $v_{s,k+1}$ in (4.28) in Figure 4.9 (b). It can be noticed from Figure 4.9 (a) that there are three types of triangles in the three-level hexagon, i.e., the inner triangle, the intermediate triangle and the outer triangle, as shown in Figure 4.10 respectively. Take Figure 4.10 (a) as an example, when $v_{s,k+1}$ locates in AOB, there are 7 adjacent voltage vectors, Hence a cost function can be used to find the distance between the possible voltage vector $v_s(i)$ and the demanded voltage vector $v_{s,k+1}$, the cost function can be written as:

$$f(i) = \|\mathbf{v}_s(i) - \mathbf{v}_{s,k+1}\|^2 = (v_{s\alpha}(i) - v_{s\alpha,k+1})^2 + (v_{s\beta}(i) - v_{s\beta,k+1})^2 + (v_{s0}(i) - v_{s0,k+1})^2 \quad (4.29)$$

The voltage vector to be applied at time instant k+1 can be expressed as:

$$\mathbf{v}_{opt,k+1} = \arg \min_{\{i=1,2,\dots,7\}} f(i) \quad (4.30)$$

From (4.30), it can be known that the number of evaluations is 7, which equals to the number of voltage vectors located in inner triangle. Same operation can be performed when $v_{s,k+1}$ locates in intermediate triangle or outer triangle, the number of evaluations is 5 or 4 according to 4.10 (b) and (c). Compared with conventional PCC method mentioned in the previous section, the proposed method does not have weighting factor and does not need to evaluate (4.16) for each of the possible voltage vectors. Also the number of evaluations is

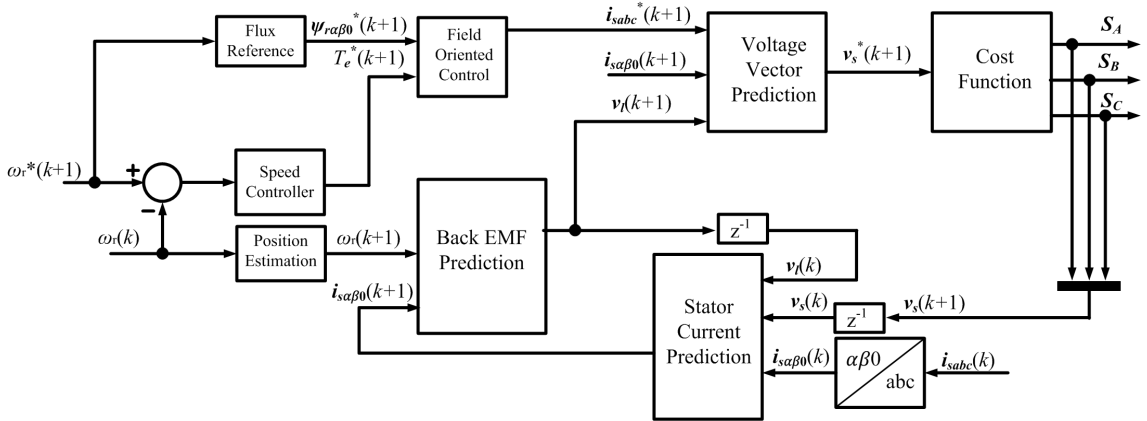


Figure 4.11: Block Diagram of the Controller

reduced according to the location of $v_{s,k+1}$. Hence the searching loop is simplified and the calculation time is reduced. Besides, due to the quadratic nature of the cost function, the proposed method can also provide stronger suppression on zero-sequence current. The block diagram of the proposed controller is shown in Figure 4.11.

4.3.2 Experimental Results

To verify the performance of the proposed method, an experimental system was developed, the block diagram is shown in Figure 4.4 (a), and the system overview is shown in Figure 4.4 (b). A 4-pole OEWIM is coupled with a permanent magnet synchronous motor (PMSM) used as a load. Two three-phase two-level inverters are used for the OEWIM drive and one three-phase inverter for PMSM drive. The OEWIM parameters are shown in Table 4.1, the inverter and motor specifications are shown in Table 4.2. A quadrature encoder is mounted on the shaft of PMSM, the speed information is sent to both PMSM controller and OEWIM controller. A Texas Instrument TMS320F28335 microcontroller mounted on a self-implemented board is used as the controller for OEWIM. The clock frequency of the MCU is 150MHz, the sampling frequency of the speed PI control loop is 1 kHz, and the sampling frequency of the inner control loop is 20 kHz. The conventional PCC is also implemented to

Table 4.4: Computation Time Comparison

Conventional PCC	39.46 μs (5919 clock cycles)
Proposed 3DPCTC	14.11 μs (2117 clock cycles)

provide a comparison with the proposed method. The weighting factor w_0 in (4.16) is set to be 1.

Table 4.4 shows the calculation time of 3DPCTC and conventional PCC. Under a 20 kHz sampling frequency, there are 7500 clock cycles within each sampling period. The conventional PCC uses 5919 clock cycles to finish the calculation, which utilized 78.92% of the sampling period, while the proposed 3DPCTC utilized 28.23% of the sampling period. Compared with conventional PCC, the proposed method reduces the calculation time by 64.24%. It can be drawn that with the proposed 3DPCTC, the controller can work under higher sampling frequency, which means the current ripple and torque ripples can be further reduced.

Figure 4.12 and Figure 4.13 present the steady state performance of OEWIM drive under proposed 3DPCTC and conventional PCC. When the motor is running at low speed ($0.2\text{pu} = 294\text{rpm}$), both control methods provide similar response as shown in Figure 4.12. During this test, the output voltage vector is within the shaded hexagon shown in Figure 4.9, hence the zero-sequence current can be suppressed to around zero. However, when the motor is running at rated speed ($1.0\text{pu} = 1470\text{rpm}$) with 0.8 pu load, the voltage vector exceeds the shaded region, hence the zero-sequence voltage is inevitable, which results in larger zero-sequence current. It can be observed from Figure 4.13, the magnitude of zero-sequence current under 3DPCTC is less than that under conventional PCC. Therefore, the proposed 3DPCTC method can provide stronger zero-sequence current suppression than conventional PCC.

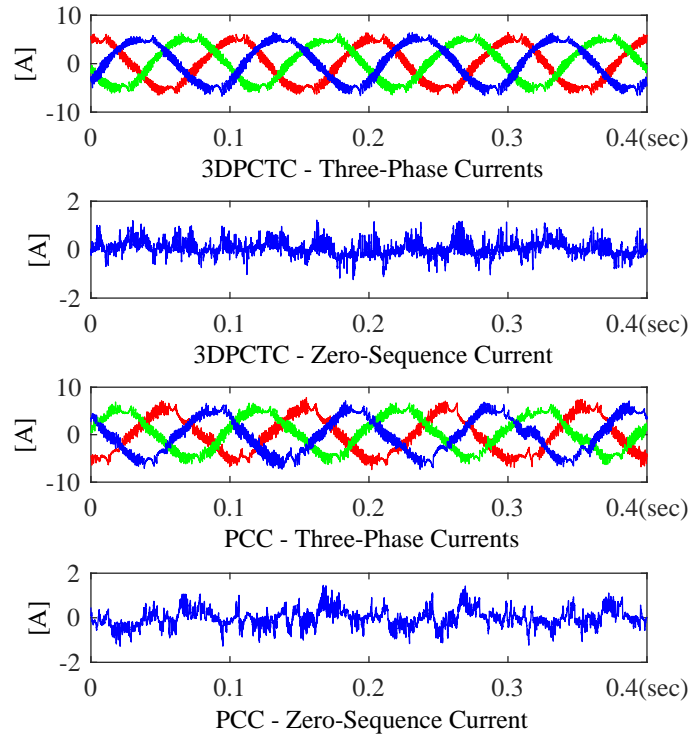


Figure 4.12: Steady State Response at 0.3pu Speed with No Load

To verify the transient state responses, two tests are conducted based on the proposed 3DPCTC and conventional PCC. In Figure 4.14, the motor is initialized at 0.2 pu speed with no load, at $t = 0.1s$, a 1.0 pu speed step is given to the motor. It can be observed that although the response times of 3DPCTC and PCC are similar, 3DPCTC provides better zero-sequence current suppression during the transient state. Also, during a torque step change, 3DPCTC can provide stronger zero-sequence current suppression than conventional PCC, as shown in Figure 4.15. Therefore it can be drawn that 3DPCTC can provide a more stable performance during transient states.

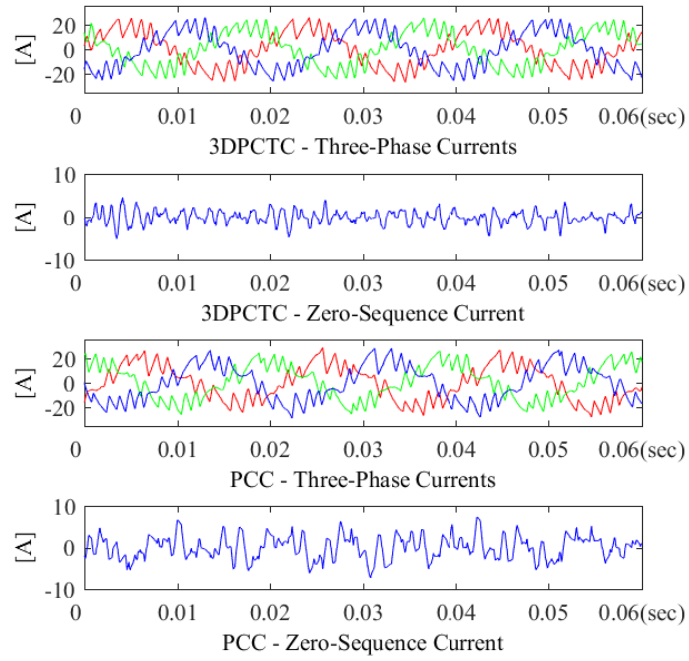


Figure 4.13: Steady State Response at 1.0 pu Speed with 0.8 pu Load

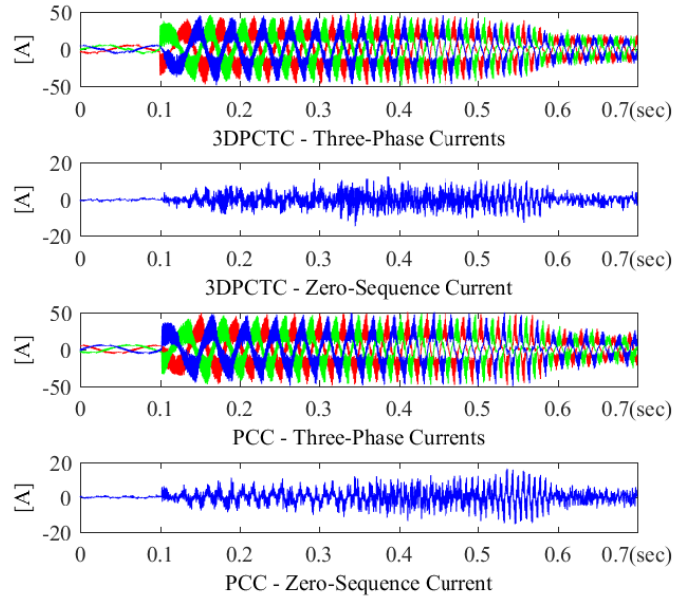


Figure 4.14: Transient State Response 0.2 pu to 1.0 pu Speed Change

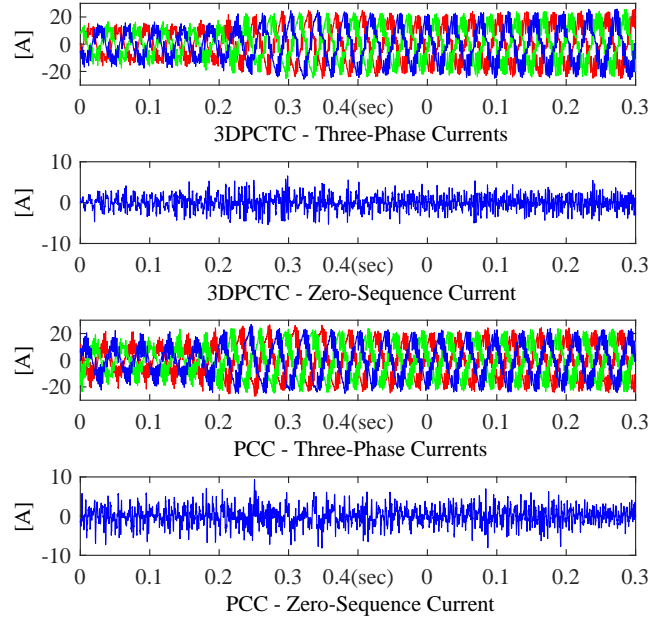


Figure 4.15: Transient State Response 0.8pu Torque Step at 1.0 pu Speed

4.4 Summary

In this chapter, two computation-efficient predictive current control methods, i.e., predictive current control in A-B-C frame (PCC-ABC) and three-dimensional predictive current trajectory control (3DPCTC), are proposed for open-end winding induction motor. Compared with conventional wye-connected induction motor, more voltage vectors and an additional zero-sequence current need to be considered. The proposed methods are compared with conventional PCC method through simulations and experiments. Some of the advantages that can be achieved by using proposed methods can be summarized as follows:

- Complete elimination of weighting factor.
- Better optimization compared with conventional PCC.

- Significant reduction on computation time. The proposed PCC-ABC reduces the calculation time by 61.05%, and the proposed 3DPCTC reduces the computation time by 64.24%.
- Stronger zero-sequence current suppression.

CHAPTER 5

PREDICTIVE CURRENT CONTROL WITH DISTURBANCE OBSERVER AND ZERO STEADY STATE ERROR

A significant characteristic of model predictive control (MPC) is the utilization of system model for determining optimal actuations. One common assumption of MPC is that the system parameter values are accurate and time invariant, which is not the case in real systems. Due to the changing operating environment, the motor parameters cannot remain the same as the nominal values at all the time. These parameter mismatches can affect the controller's optimization process and would result in steady-state error or even deteriorate the system's dynamic response. Considering these issues, this chapter provides a systematic analysis on parameter sensitivities of electrical torque and rotor flux. A deadbeat predictive current control method with disturbance observer (PCC-DO) is proposed to compensate the parameter mismatch, to eliminate the steady-state error, and to provide fast dynamic responses.

5.1 Introduction

Model predictive control (MPC) is known for its intuitive concept, fast dynamic response and good capacity of handling system constraints and non-linearities. However, MPC excessively relies on system mathematical model to predict the future states of the plant. The precision of model parameters directly affect the static and dynamic performances of MPC. In real systems, the plant parameters always change with the environment. As for induction motor, the stator and rotor resistance change with temperature, and the magnetization inductance may vary if the motor enters the saturation zone. In addition to modeled parameters, unconsidered dynamics also introduce disturbances to the controller. Therefore, effective methods need to be developed to compensate the parameter mismatch and unmodeled disturbances.

In non-linear MPC methods, the parameter mismatch and other disturbances are addressed in a cost function [52]. However, the cost function ensures the global optimality, it cannot guarantee local optimality for each variable [89]. In other words, the summation of the errors of all considered control variables can be minimized through cost function, but error in each control variable is not eliminated. Also, due to the fact that non-linear MPC can only output discrete voltage vectors throughout each sampling period, there is always steady-state errors in stator currents.

In comparison, linear MPC methods can achieve similar dynamic performance with their non-linear counterparts, while maintain higher resolution in the output voltage vectors due to the use of pulse width modulation. However, additional steps need to be take to compensate the parameter mismatches and unmodeled disturbances. Researchers have proposed multiple solutions to compensate the disturbances [90–92]. A current-regulated delta modulator is proposed in [90] for current error-correction. In [91], a predictive current control method is presented to compensate the current error resulted from inductance variation. In [92], a predictive control method with parallel integral loop to compensate the motor parameter mismatch is illustrated. However, the fixed integral gain cannot provide satisfactory responses when operating point changes. Another solution is to add a disturbance observer to the predictive controller [93–97]. A non-linear disturbance observer for handling parameter mismatches on non-linear systems is presented in [93]. In [94], the output prediction of a buck converter is regulated by a system error observer. A sliding-mode disturbance observer with a new switching surface is proposed to solve parameter mismatch problems in [95, 96]. And in [98], deadbeat control methods with disturbance observer using different reaching laws are proposed on wye-connected permanent magnet synchronous motor.

The aforementioned methods provide accurate disturbance compensation on power converters and conventional wye-connected induction motors. But for open-end winding configuration studied in this dissertation, the zero-sequence current needs to be considered, and

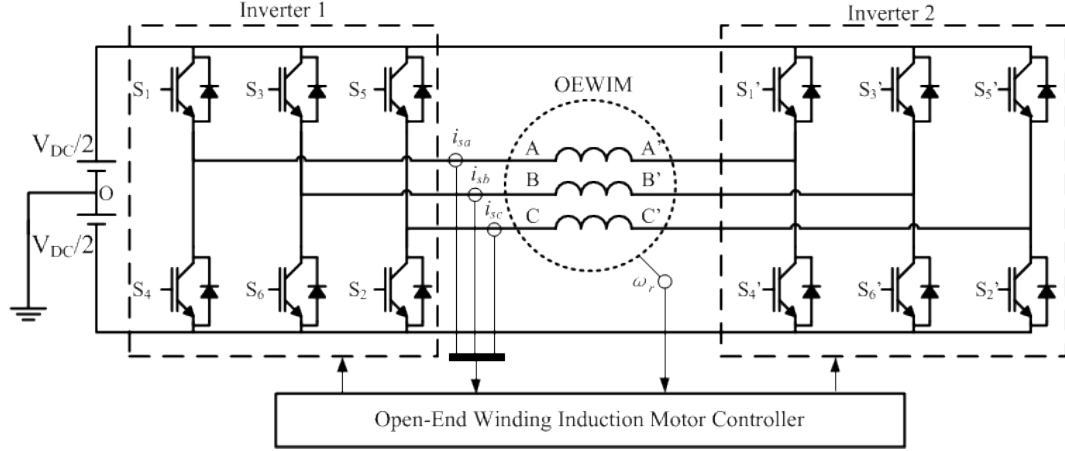


Figure 5.1: An Open-End Winding Induction Motor Drive

the delay described in Section 2.3 needs to be compensated. Hence, a proper control method is required to address these issues. In this chapter, a deadbeat predictive current control method with disturbance observer (PCC-DO) is proposed. The indirect field oriented control (IFOC) is first reviewed. A parameter sensitivity analysis with respect to electrical torque and rotor flux linkage is given. Based on the analysis, a sliding-mode disturbance observer is designed to compensate the parameter mismatches. The stability of the controller is then discussed. To verify the effectiveness of the proposed controller, steady state and transient simulations are performed. The simulation results show that the proposed method can effectively compensate the error resulted from parameter mismatch and eliminate the steady-state error.

5.2 Indirect Field Oriented Control (IFOC)

In open-end winding induction motor fed by two inverters with common DC source shown in Figure 5.1, the electrical model in the arbitrary frame is given by (5.1) to (5.5):

$$\mathbf{v}_s = \mathbf{R}_s \mathbf{i}_s + p\boldsymbol{\psi}_s + \mathbf{j}\omega_a \boldsymbol{\psi}_s \quad (5.1)$$

$$\mathbf{0} = \mathbf{R}_r \mathbf{i}_r + p\boldsymbol{\psi}_r + \mathbf{j}(\omega_a - \omega_r)\boldsymbol{\psi}_r \quad (5.2)$$

$$\boldsymbol{\psi}_s = \mathbf{L}_s \mathbf{i}_s + \mathbf{L}_m \mathbf{i}_r \quad (5.3)$$

$$\boldsymbol{\psi}_r = \mathbf{L}_r \mathbf{i}_r + \mathbf{L}_m \mathbf{i}_s \quad (5.4)$$

$$T_e = \frac{3}{2} P (\psi_{sd} i_{sq} - \psi_{sq} i_{sd}) \quad (5.5)$$

In which $\mathbf{R}_s, \mathbf{R}_r, \mathbf{L}_s, \mathbf{L}_r, \mathbf{L}_m$ are system parameter matrices with zero-sequence components, e.g. $\mathbf{R}_s = \text{diag}[R_s, R_s, R_s]$, $\mathbf{L}_s = \text{diag}[L_s, L_s, L_{ls}]$, $\mathbf{L}_m = \text{diag}[L_m, L_m, 0]$. And $\mathbf{v}_s, \mathbf{i}_s, \mathbf{i}_r, \boldsymbol{\psi}_s, \boldsymbol{\psi}_r$ are state variables with zero-sequence component, e.g. $\mathbf{v}_s = \begin{bmatrix} v_{sd} & v_{sq} & v_{s0} \end{bmatrix}^T$. ω_a is arbitrary speed of the reference frame, ω_r is the rotor electrical angular speed, p is the derivative operator, P is number of pole pairs. \mathbf{j} is the coupling matrix which is given as:

$$\mathbf{j} = \begin{bmatrix} 0 & -1 & 0 \\ 1 & 0 & 0 \\ 0 & 0 & 0 \end{bmatrix}$$

The slip speed is defined as:

$$\omega_{slip} = \omega_a - \omega_r \quad (5.6)$$

In the rotor flux synchronous rotating frame ($\omega_a = \omega_e$) in which the rotor flux is aligned with d axis, the following relationships can be obtained:

$$\psi_{rd} = |\boldsymbol{\psi}_r| \quad (5.7)$$

$$\psi_{rq} = 0 = p\psi_{rq} \quad (5.8)$$

Then the rotor voltage equation (5.2) becomes:

$$R_r i_{rd} + p|\boldsymbol{\psi}_r| = 0 \quad (5.9)$$

$$R_r i_{rq} + \omega_{slip} |\boldsymbol{\psi}_r| = 0 \quad (5.10)$$

Also by using the relationships in (5.7) (5.8), the rotor currents in (5.4) can be expressed as:

$$i_{rd} = \frac{1}{L_r} (|\boldsymbol{\psi}_r| - L_m i_{sd}) \quad (5.11)$$

$$i_{rq} = -\frac{L_m}{L_r} i_{sq} \quad (5.12)$$

Substituting (5.11) (5.12) into (5.9) (5.10) gives

$$p|\boldsymbol{\psi}_r| = -\frac{1}{\tau_r} (|\boldsymbol{\psi}_r| - L_m i_{sd}) \quad (5.13)$$

$$\omega_{slip} = \frac{L_m}{\tau_r} \frac{i_{sq}}{|\boldsymbol{\psi}_r|} \quad (5.14)$$

Where $\tau_r = \frac{L_r}{R_r}$ is the rotor time constant. And the torque equation becomes

$$T_e = \frac{3}{2} P \frac{L_m}{L_r} i_{sq} |\boldsymbol{\psi}_r| \quad (5.15)$$

Let i_{T_e} and i_ψ be the torque-producing and flux producing currents, then i_{T_e} and i_ψ are defined as:

$$i_{T_e}^* = i_{sq}^* = \frac{2P}{3} \frac{T_e^*}{|\boldsymbol{\psi}_r|^*} \frac{L_r}{L_m} \quad (5.16)$$

$$i_\psi^* = i_{sd}^* = \frac{1}{L_m} (1 + \tau_r^* p) |\boldsymbol{\psi}_r|^* \quad (5.17)$$

$$\omega_{slip}^* = \frac{L_m^*}{\tau_r^*} \frac{i_{T_e}^*}{|\boldsymbol{\psi}_r|^*} \quad (5.18)$$

(5.18) can be also written in the form related to the reference torque:

$$\omega_{slip}^* = \frac{2P}{3} \frac{R_r^* T_e^*}{(|\boldsymbol{\psi}_r|^*)^2} \quad (5.19)$$

From (5.17) to (5.19), the IFOC schematic can be obtained, and it is shown in Figure 5.2 and 5.3. Figure 5.2 shows the ω_{slip}^* calculated from (5.18), and Figure 5.3 shows the ω_{slip}^* calculated from (5.19).

Although (5.18) and (5.19) give identical results in steady-state [99], an apparent difference comes in when parameter mismatch happens. Assume the flux command $|\boldsymbol{\psi}_r|^*$ and torque command T_e^* are constant, ω_{slip}^* calculated from (5.18) is affected by rotor constant τ_r , and ω_{slip}^* computed from (5.19) is impacted by rotor resistance R_r . Different variations on τ_r or R_r can result in different i_ψ^* and $i_{T_e}^*$.

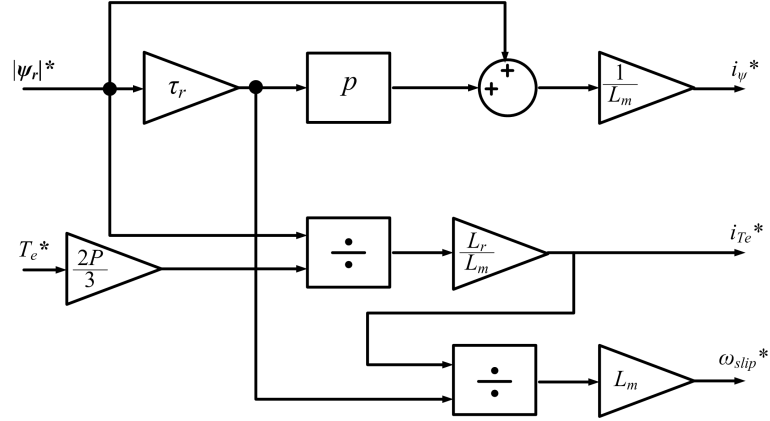


Figure 5.2: IFOC schematic with Slip Calculation 1

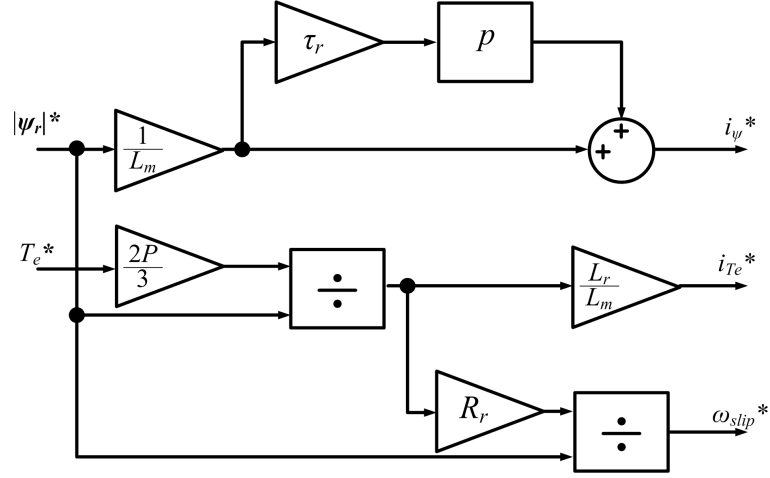


Figure 5.3: IFOC schematic with Slip Calculation 2

Additionally, the zero-sequence current reference i_{s0}^* is always set to be 0, since the zero-sequence current always needs to be suppressed. By transferring the current references from synchronous frame to stationary frame, the current vector $\begin{bmatrix} i_{s\alpha}^* & i_{s\beta}^* & i_{s0}^* \end{bmatrix}^T$ can be obtained as:

$$\begin{bmatrix} i_{s\alpha}^* \\ i_{s\beta}^* \\ i_{s0}^* \end{bmatrix} = \begin{bmatrix} \cos(\theta_\psi) & -\sin(\theta_\psi) & 0 \\ \sin(\theta_\psi) & \cos(\theta_\psi) & 0 \\ 0 & 0 & 1 \end{bmatrix} \begin{bmatrix} i_\psi^* \\ i_{Te}^* \\ i_{s0}^* \end{bmatrix} \quad (5.20)$$

And the rotor flux angle is calculated by:

$$\theta_\psi = \theta_r + \theta_{slip}^* = (\omega_r + \omega_{slip}^*)t \quad (5.21)$$

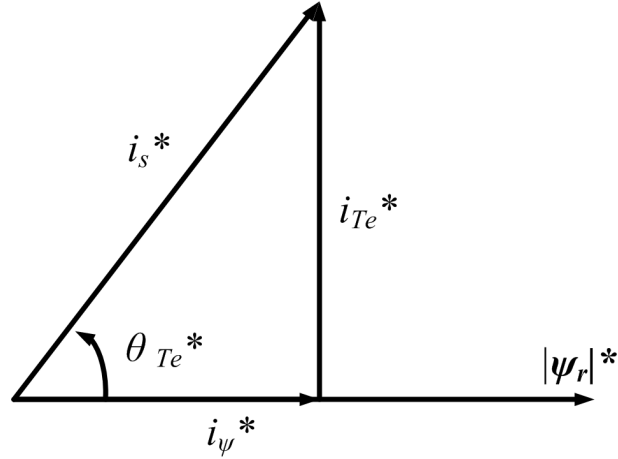


Figure 5.4: Relationship between Flux-Producing Current and Torque-Producing Current

5.3 Parameter Sensitivity Analysis

During the operation of induction motor, the change in parameters can result in steady-state errors on current and torque, hence it is necessary to investigate the effects of parameter mismatches on system performance. In this section, an analysis is given on parameter sensitivity with respect to steady-state torque and flux.

5.3.1 Parameter Sensitivity of Electrical Torque

In the steady state operation, the flux derivative is negligible, substitute $p = 0$ into (5.17), the following relationship is obtained:

$$|\psi_r|^* = L_m^* i_{\psi}^* \quad (5.22)$$

Substitute the above equation into (5.18), the slip speed command becomes

$$\omega_{slip}^* = \frac{1}{\tau_r^*} \frac{i_{Te}^*}{i_{\psi}^*} \quad (5.23)$$

Notice that the torque angle θ_{Te}^* is defined as the angle between i_s^* and ψ_r^* shown in Figure 5.4, and it is given as

$$\theta_{Te}^* = \tan^{-1}\left(\frac{i_{Te}^*}{i_{\psi}^*}\right) \quad (5.24)$$

And the following can be calculated:

$$\sin \theta_{T_e}^* = \frac{\omega_{slip}^* \tau_r^*}{\sqrt{1 + (\omega_{slip}^* \tau_r^*)^2}} \quad (5.25)$$

$$\cos \theta_{T_e}^* = \frac{1}{\sqrt{1 + (\omega_{slip}^* \tau_r^*)^2}} \quad (5.26)$$

Then the torque command can be expressed as a function of current vector magnitude and torque angle

$$T_e^* = \frac{3P}{2} \cdot \frac{(L_m^*)^2}{L_r^*} \cdot (i_s^*)^2 \cdot \cos \theta_{T_e}^* \cdot \sin \theta_{T_e}^* \quad (5.27)$$

With the actual parameters, the electrical torque generated in the motor can be calculated as

$$T_e = \frac{3P}{2} \cdot \frac{(L_m)^2}{L_r} \cdot (i_s)^2 \cdot \cos \theta_{T_e} \cdot \sin \theta_{T_e} \quad (5.28)$$

The ratio between actual torque and its command value can be obtained as

$$\frac{T_e}{T_e^*} = \left(\frac{L_m}{L_m^*} \right)^2 \cdot \frac{L_r^*}{L_r} \cdot \frac{\tau_r}{\tau_r^*} \cdot \left(\frac{1 + (\omega_{slip}^* \tau_r^*)^2}{1 + (\omega_{slip} \tau_r)^2} \right) \quad (5.29)$$

Error in Rotor Resistance R_r

When the rotor resistance R_r of the motor changes due the temperature variation, the rotor time constant also changes. Define g_R is the variation between actual rotor resistance R_r and its nominal value R_r^* , then R_r can be written as:

$$R_r = g_R \cdot R_r^*$$

And assume no changes in mutual inductance and rotor leakage inductance, the following can be obtained:

$$L_m = L_m^*$$

$$L_r = L_r^*$$

$$\tau_r = \frac{1}{g_R} \tau_r^*$$

Then (5.29) becomes

$$\frac{T_e}{T_e^*} = \frac{1}{g_R} \cdot \left(\frac{1 + (\omega_{slip}^* \tau_r^*)^2}{1 + (\frac{1}{g_R} \omega_{slip}^* \tau_r^*)^2} \right) \quad (5.30)$$

Error in Magnetization Inductance L_m

Due to the saturation of the motor, the magnetization inductance varies from its nominal value. Assume the leakage inductance is negligible, and define the ratio between actual inductance L_m and nominal value L_m^* as g_L , the actual magnetization inductance can be written as

$$\begin{aligned} L_m &= g_L \cdot L_m^* \\ \frac{L_r^*}{L_r} &\approx \frac{L_m^*}{L_m} = \frac{1}{g_L} \end{aligned}$$

Substitute the above equations into (5.29), the parameter sensitivity of electrical torque with respect to rotor resistance R_r and magnetization inductance L_m can be expressed as:

$$\frac{T_e}{T_e^*} = \frac{g_L}{g_R} \cdot \left(\frac{1 + (\omega_{slip}^* \tau_r^*)^2}{1 + (\frac{1}{g_R} \omega_{slip}^* \tau_r^*)^2} \right) \quad (5.31)$$

5.3.2 Parameter Sensitivity of Rotor Flux Linkage

During the steady-state operation, the actual rotor flux linkage is:

$$|\psi_r| = L_m i_\psi \quad (5.32)$$

Then the ratio of actual flux linkage and its command value is

$$\frac{|\psi_r|}{|\psi_r^*|} = \frac{L_m i_\psi}{L_m^* i_\psi^*} \quad (5.33)$$

Substitute (5.26) into (5.33), assume the rotor resistance variation $R_r = g_R \cdot R_r^*$ and inductance variation $L_m = g_L \cdot L_m^*$, the parameter sensitivity of flux linkage can be obtained as:

$$\frac{\psi_r}{\psi_r^*} = g_L \sqrt{\frac{1 + (\omega_{slip}^* \tau_r^*)^2}{1 + (\frac{1}{g_R} \omega_{slip}^* \tau_r^*)^2}} \quad (5.34)$$

5.4 Proposed Deadbeat Predictive Current Control with Disturbance Observer (PCC-DO)

It can be drawn from Section 5.3 that the parameter mismatches can introduce steady-state errors in electrical torque and rotor flux. Effective methods need to be developed to compensate the mismatch and eliminate the errors. In this section, a deadbeat predictive current control method with disturbance observer (PCC-DO) is introduced.

From Section 2.1, the stator voltage vector equation with respect to stator current \mathbf{i}_s and rotor flux $\boldsymbol{\psi}_r$ in synchronous frame can be expressed as:

$$p\mathbf{i}_s = \frac{\mathbf{I}}{\mathbf{L}_s\boldsymbol{\sigma}}\mathbf{v}_s + \left(-\frac{\mathbf{I}}{\mathbf{L}_s\boldsymbol{\sigma}}(\mathbf{R}_s + \frac{\mathbf{L}_m^2}{\mathbf{L}_r^2}\mathbf{R}_r) - \mathbf{j}\omega_e\right)\mathbf{i}_s + \left(\frac{\mathbf{L}_m\mathbf{R}_r}{\mathbf{L}_r^2\mathbf{L}_s\boldsymbol{\sigma}} - \mathbf{j}\omega_r\right)\frac{\mathbf{L}_m}{\mathbf{L}_r\mathbf{L}_s\boldsymbol{\sigma}}\boldsymbol{\psi}_r \quad (5.35)$$

Denote $R = R_s + \frac{L_m^2}{L_r^2}R_r$, $L = L_s\sigma$, $k_r = \frac{L_m}{L_r}$, $\tau_r = \frac{L_r}{R_r}$, the above equation in $d-q-0$ rotor flux reference frame ($\psi_{rd} = |\boldsymbol{\psi}_r|, \psi_{rq} = 0$) can be written as

$$v_{sd} = Lp i_{sd} + R i_{sd} - \omega_e L i_{sq} - \frac{k_r}{\tau_r} \psi_{rd} \quad (5.36)$$

$$v_{sq} = Lp i_{sq} + R i_{sq} + \omega_e L i_{sd} + k_r \omega_r \psi_{rd} \quad (5.37)$$

$$v_{s0} = L_{l_s} p i_{s0} + R_s i_{s0} \quad (5.38)$$

Write (5.36)(5.37) in state-space form, one can get

$$p \begin{bmatrix} i_{sd} \\ i_{sq} \end{bmatrix} = \begin{bmatrix} -\frac{R}{L} & \omega_e \\ -\omega_e & -\frac{R}{L} \end{bmatrix} \begin{bmatrix} i_{sd} \\ i_{sq} \end{bmatrix} + \begin{bmatrix} \frac{1}{L} \\ \frac{1}{L} \end{bmatrix} \begin{bmatrix} v_{sd} \\ v_{sq} \end{bmatrix} + \begin{bmatrix} \frac{k_r}{\tau_r L} & \frac{k_r}{L} \omega_r \\ -\frac{k_r}{L} \omega_r & \frac{k_r}{\tau_r L} \end{bmatrix} \begin{bmatrix} \psi_{rd} \\ \psi_{rq} \end{bmatrix} \quad (5.39)$$

Discretize (5.39) using forward Euler method, the stator d-axis and q-axis currents can be predicted as

$$p \begin{bmatrix} i_{sd,k+1} \\ i_{sq,k+1} \end{bmatrix} = \begin{bmatrix} 1 - \frac{R}{L}T_s & \omega_e T_s \\ -\omega_e T_s & 1 - \frac{R}{L}T_s \end{bmatrix} \begin{bmatrix} i_{sd,k} \\ i_{sq,k} \end{bmatrix} + \begin{bmatrix} \frac{T_s}{L} \\ \frac{T_s}{L} \end{bmatrix} \begin{bmatrix} v_{sd,k} \\ v_{sq,k} \end{bmatrix} + \begin{bmatrix} \frac{k_r T_s}{\tau_r L} & \frac{k_r}{L} \omega_r T_s \\ -\frac{k_r}{L} \omega_r T_s & \frac{k_r T_s}{\tau_r L} \end{bmatrix} \begin{bmatrix} \psi_{rd,k} \\ \psi_{rq,k} \end{bmatrix} \quad (5.40)$$

Let the following denotes the discrete domain parameter matrices:

$$\mathbf{A} = \begin{bmatrix} 1 - \frac{R}{L}T_s & \omega_e T_s \\ -\omega_e T_s & 1 - \frac{R}{L}T_s \end{bmatrix} \quad \mathbf{B} = \begin{bmatrix} \frac{T_s}{L} \\ \frac{T_s}{L} \end{bmatrix} \quad \mathbf{F} = \begin{bmatrix} \frac{k_r T_s}{\tau_r L} & \frac{k_r \omega_r T_s}{L} \\ -\frac{k_r \omega_r T_s}{L} & \frac{k_r T_s}{\tau_r L} \end{bmatrix}$$

Then (5.40) becomes

$$\mathbf{i}_{s,k+1} = \mathbf{A}\mathbf{i}_{s,k} + \mathbf{B}\mathbf{v}_{s,k} + \mathbf{F}\psi_{r,k} \quad (5.41)$$

Due to the delay effect described in Section 2.3, one more step extrapolation is required to compensate the delay, and (5.41) becomes

$$\mathbf{i}_{s,k+2} = \mathbf{A}\mathbf{i}_{s,k+1} + \mathbf{B}\mathbf{v}_{s,k+1} + \mathbf{F}\psi_{r,k+1} \quad (5.42)$$

Apply the deadbeat control rule to (5.42), the $\mathbf{i}_{s,k+2}$ is replaced by the current reference \mathbf{i}_s^* , and substitute (5.41) into (5.42), the following equation can be obtained:

$$\mathbf{i}_s^* = \mathbf{A}(\mathbf{A}\mathbf{i}_{s,k} + \mathbf{B}\mathbf{v}_{s,k} + \mathbf{F}\psi_{r,k}) + \mathbf{B}\mathbf{v}_{s,k+1} + \mathbf{F}\psi_{r,k+1} \quad (5.43)$$

And the voltage vector to be applied at time instant $k + 1$ can be calculated as

$$\mathbf{v}_{s,k+1} = \mathbf{B}^{-1}(\mathbf{i}_s^* - \mathbf{A}((\mathbf{A}\mathbf{i}_{s,k} + \mathbf{B}\mathbf{v}_{s,k} + \mathbf{F}\psi_{r,k}) - \mathbf{F}\psi_{r,k+1})) \quad (5.44)$$

The block diagram of the proposed controller is shown in Figure 5.5.

5.5 Design of Disturbance Observer

Include the parameter variations in (5.36) (5.37), the augmented motor model becomes

$$\begin{cases} v_{sd} = L \frac{d}{dt} i_{sd} + R i_{sd} - \omega_e L i_{sq} - \frac{k_r}{\tau_r} \psi_{rd} + f_d \\ \frac{d}{dt} f_d = F_d \end{cases} \quad (5.45)$$

$$\begin{cases} v_{sq} = L \frac{d}{dt} i_{sq} + R i_{sq} + \omega_e L i_{sd} + k_r \omega_r \psi_{rd} + f_q \\ \frac{d}{dt} f_q = F_q \end{cases} \quad (5.46)$$

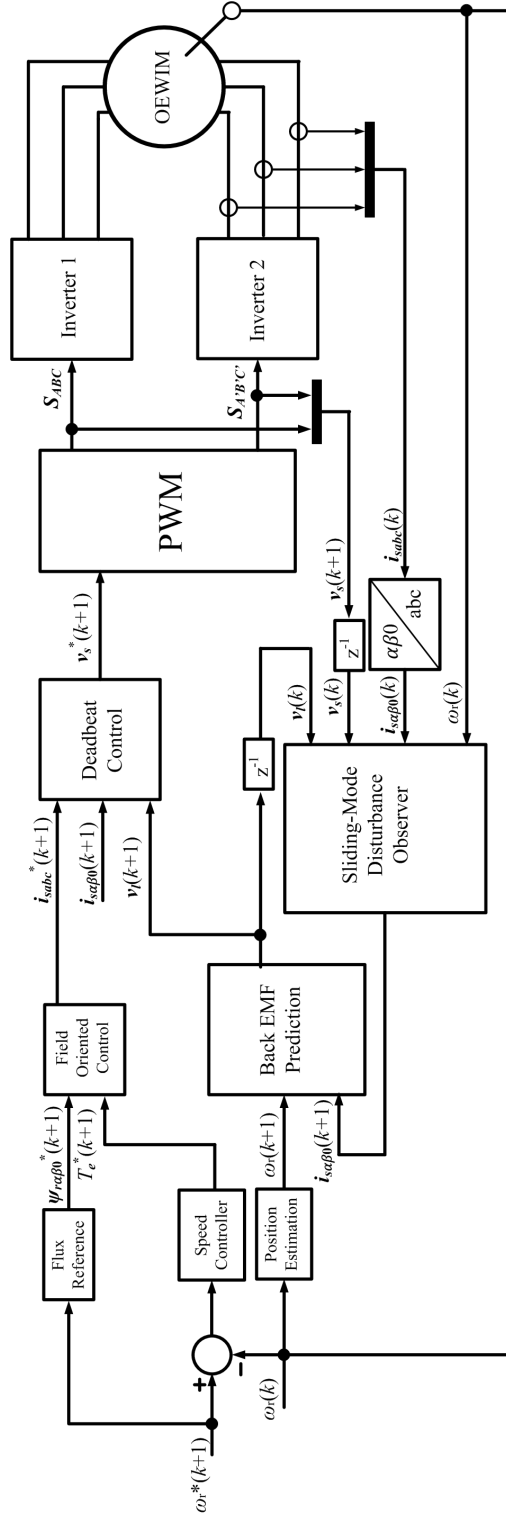


Figure 5.5: Block Diagram of Proposed Linear Predictive Current Control with Disturbance Observer

Where f_d, f_q denote the disturbance introduced from parameter mismatch, and are defined as

$$f_d = \Delta L \frac{d}{dt} i_{sd} + \Delta R i_{sd} - \Delta L \omega_e i_{sq} \quad (5.47)$$

$$f_d = \Delta L \frac{d}{dt} i_{sq} + \Delta R i_{sq} + \Delta L \omega_e i_{sd} \quad (5.48)$$

In order to estimate the disturbances due to parameter mismatches and to predict the stator currents, an observer can be designed from (5.45)(5.46):

$$\begin{cases} v_{sd} = L \frac{d}{dt} \hat{i}_{sd} + R \hat{i}_{sd} - \omega_e L i_{sq} - \frac{k_r}{\tau_r} \psi_{rd} + \hat{f}_d + U_{dsmo} \\ \frac{d}{dt} \hat{f}_d = g_d U_{dsmo} \end{cases} \quad (5.49)$$

$$\begin{cases} v_{sq} = L \frac{d}{dt} \hat{i}_{sq} + R \hat{i}_{sq} + \omega_e L i_{sd} + k_r \omega_r \psi_{rd} + \hat{f}_q + U_{qsmo} \\ \frac{d}{dt} \hat{f}_q = g_q U_{qsmo} \end{cases} \quad (5.50)$$

Where \hat{f}_d and \hat{f}_q are estimations of parameter mismatch disturbances f_d and f_q , \hat{i}_{sd} and \hat{i}_{sq} are estimated stator currents, v_{sd} and v_{sq} are measured voltages, U_{dsmo} and U_{qsmo} are sliding-mode control functions, g_d and g_q are gains in sliding-mode controller. Perform subtraction (5.49) – (5.45), (5.50) – (5.46), and the following equations can be obtained:

$$\begin{cases} 0 = L \frac{d}{dt} (\hat{i}_{sd} - i_{sd}) + R (\hat{i}_{sd} - i_{sd}) + (\hat{f}_d - f_d) + U_{dsmo} \\ \frac{d}{dt} (\hat{f}_d - f_d) = g_d U_{dsmo} - F_d \end{cases} \quad (5.51)$$

$$\begin{cases} 0 = L \frac{d}{dt} (\hat{i}_{sq} - i_{sq}) + R (\hat{i}_{sq} - i_{sq}) + (\hat{f}_q - f_q) + U_{qsmo} \\ \frac{d}{dt} (\hat{f}_q - f_q) = g_q U_{qsmo} - F_q \end{cases} \quad (5.52)$$

Define the estimated current errors e_{sd} , e_{sq} , and the estimated disturbance errors e_{fd} , e_{fq} , which are given by:

$$e_{sd} = \hat{i}_{sd} - i_{sd}$$

$$e_{sq} = \hat{i}_{sq} - i_{sq}$$

$$e_{fd} = \hat{f}_d - f_d$$

$$e_{fq} = \hat{f}_q - f_q$$

Then (5.51) and (5.52) become:

$$\begin{cases} \frac{d}{dt}e_{sd} = -\frac{R}{L}e_{sd} - \frac{1}{L}e_{fd} - \frac{1}{L}U_{dsmo} \\ \frac{d}{dt}e_{fd} = g_d U_{dsmo} - F_d \end{cases} \quad (5.53)$$

$$\begin{cases} \frac{d}{dt}e_{sq} = -\frac{R}{L}e_{sq} - \frac{1}{L}e_{fq} - \frac{1}{L}U_{qsmo} \\ \frac{d}{dt}e_{fq} = g_q U_{qsmo} - F_q \end{cases} \quad (5.54)$$

To design the sliding-mode control, a switching surface and a reaching law need to be selected.

In the proposed method, the linear switching surface is chosen, which is given as:

$$s_d = \hat{i}_{sd} - i_{sd} \quad (5.55)$$

$$s_q = \hat{i}_{sq} - i_{sq} \quad (5.56)$$

And the reaching law is selected as:

$$\frac{d}{dt}s = -k_1 \operatorname{sgn}(s) - \lambda s \quad (5.57)$$

Substitute (5.55) into (5.57):

$$\frac{d}{dt}e_{sd} = -k_1 \operatorname{sgn}(e_{sd}) - \lambda e_{sd} \quad (5.58)$$

$$\frac{d}{dt}e_{sq} = -k_1 \operatorname{sgn}(e_{sq}) - \lambda e_{sq} \quad (5.59)$$

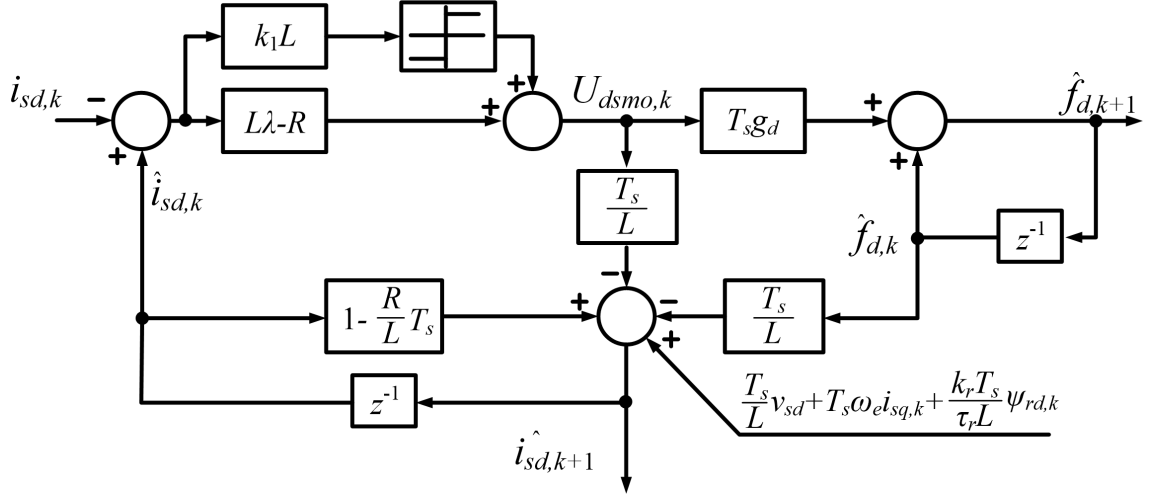


Figure 5.6: Proposed Sliding-Mode Disturbance Observer in d-axis

Replace the derivative terms in (5.53) (5.54) using (5.58) (5.59):

$$-\frac{R}{L}e_{sd} - \frac{1}{L}e_{fd} - \frac{1}{L}U_{dsmo} = -k_1 \text{sgn}(e_{sd}) - \lambda e_{sd} \quad (5.60)$$

$$-\frac{R}{L}e_{sq} - \frac{1}{L}e_{fq} - \frac{1}{L}U_{qsmo} = -k_1 \text{sgn}(e_{sq}) - \lambda e_{sq} \quad (5.61)$$

Then the compensated voltage U_{dsmo} and U_{qsmo} can be calculated as:

$$U_{dsmo} = (L\lambda - R)e_{sd} + k_1 L \text{sgn}(e_{sd}) \quad (5.62)$$

$$U_{qsmo} = (L\lambda - R)e_{sq} + k_1 L \text{sgn}(e_{sq}) \quad (5.63)$$

Discretize (5.49) (5.50) using forward Euler method, the stator current and parameter disturbance can be predicted as:

$$\hat{i}_{sd,k+1} = \left(1 - \frac{RT_s}{L}\right)\hat{i}_{sd,k} + \frac{T_s}{L}v_{sd,k} + \omega_e T_s i_{sq,k} + \frac{k_r T_s}{\tau_r L}\psi_{rd,k} - \frac{T_s}{L}\hat{f}_{d,k} - \frac{T_s}{L}U_{dsmo,k} \quad (5.64)$$

$$\hat{f}_{d,k+1} = \hat{f}_{d,k} + T_s g_d U_{dsmo,k} \quad (5.65)$$

$$\hat{i}_{sq,k+1} = \left(1 - \frac{RT_s}{L}\right)\hat{i}_{sq,k} + \frac{T_s}{L}v_{sq,k} - \omega_e T_s i_{sd,k} - \frac{k_r T_s}{L}\omega_r \psi_{rd,k} - \frac{T_s}{L}\hat{f}_{q,k} - \frac{T_s}{L}U_{qsmo,k} \quad (5.66)$$

$$\hat{f}_{q,k+1} = \hat{f}_{q,k} + T_s g_q U_{qsmo,k} \quad (5.67)$$

The schematic of the proposed disturbance observer is shown in Figure 5.6 and 5.7.

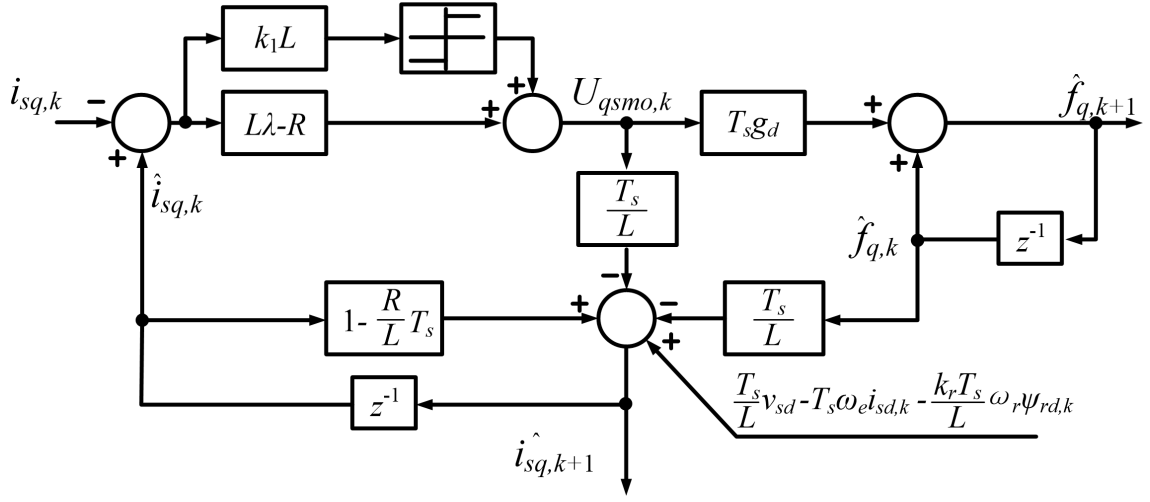


Figure 5.7: Proposed Sliding-Mode Disturbance Observer in q-axis

5.6 Stability Analysis of the Controller

It is necessary to investigate the stability of the proposed observer. Based on Lyapunov's stability criterion, the following condition must be satisfied:

$$e_{sd} \cdot \dot{e}_{sd} \leq 0 \quad (5.68)$$

$$e_{sq} \cdot \dot{e}_{sq} \leq 0 \quad (5.69)$$

As the derivatives of e_{sd} and e_{sq} are defined in (5.58) (5.59), substitution of (5.58) into (5.68) yields

$$\begin{aligned}
e_{sd} \cdot \dot{e}_{sd} &= -\frac{1}{L}e_{sd}(Re_{sd} + e_{fd} + U_{dsmo}) \\
&= -\frac{1}{L}e_{sd}(Re_{sd} + e_{fd} + (L\lambda - R)e_{sd} + k_1L\text{sgn}(e_{sd})) \\
&= -\frac{1}{L}(L\lambda e_{sd}^2 + e_{sd}(e_{fd} + k_1L\text{sgn}(e_{sd}))) \\
&= -\frac{1}{L}\left(L\lambda e_{sd}^2 + e_{sd}\text{sgn}(e_{sd})\left(k_1L + \frac{e_{fd}}{\text{sgn}(e_{sd})}\right)\right) \\
&= -\frac{1}{L}\left(L\lambda e_{sd}^2 + |e_{sd}|\left(k_1L + \frac{e_{fd}}{\text{sgn}(e_{sd})}\right)\right) \leq 0
\end{aligned}$$

Table 5.1: Motor Ratings and Parameters

Power(kW)	5.5
Poles	4
Rating Speed (rpm)	1470
Line to Line Voltage (V)	200
Stator Resistance ($m\Omega$)	834
Rotor Resistance ($m\Omega$)	654
Stator Leakage Inductance (mH)	3.2
Rotor Leakage Inductance (mH)	3.2
Mutual Inductance (mH)	138.1

To ensure the above equation, it requires

$$k_1 L + \frac{e_{fd}}{\text{sgn}(e_{sd})} \geq 0 \quad (5.70)$$

Therefore,

$$k_1 > \frac{e_{fd}}{L} \quad (5.71)$$

Same derivation can be performed on q-axis, and it results in

$$k_1 > \frac{e_{fq}}{L} \quad (5.72)$$

From (5.71) (5.72), the condition for k_1 such that the observer will always be stable can be given as

$$k_1 > \frac{1}{L} \max(e_{fd}, e_{fq}) \quad (5.73)$$

5.7 Simulation Results

To verify the effectiveness of proposed method, simulation is performed using Matlab/Simulink software. The motor parameters are listed in Table 4.1. The PWM carrier frequency is 10 kHz, and the sampling frequency of the controller is set to be 20 kHz. The sliding-mode observer gains are selected to be $k_1 = 0.2, g_d = g_q = 1, \lambda = 3$. A conventional linear predictive current control is also implemented to provide comparison with the proposed method.

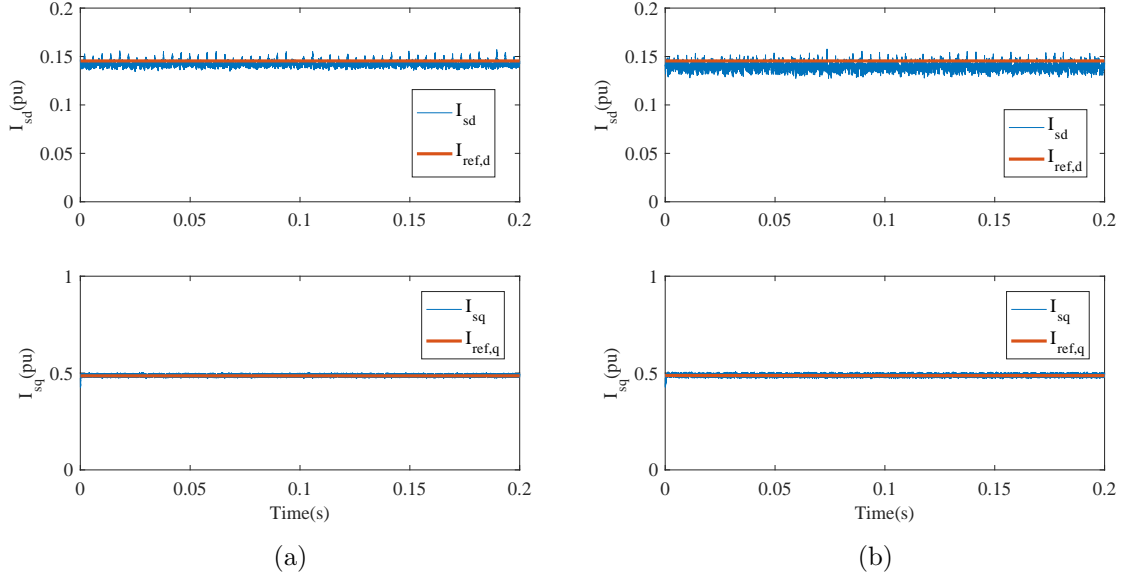


Figure 5.8: Steady-State Response with No Disturbance
(a) Conventional Linear PCC
(b) Proposed PCC-DO

5.7.1 Steady State Performance

In the steady-state test, the motor is controlled at 0.8 pu speed (1176 rpm) and with 0.8 pu load torque. At time instant $t = 0.1s$, a parameter disturbance is added to the motor.

Figure 5.8 shows the responses when there is no disturbance on the stator resistance R_s . It can be observed that the proposed method and conventional method both provide accurate track of the reference currents. Figure 5.9 to 5.11 shows the responses when the stator resistance R_s varies. It can be observed that when R_s varies from its nominal values R_s^* , the conventional PCC presents large steady-state errors, while the proposed method can compensate the parameter mismatch and maintain zero steady errors on d-axis and q-axis currents.

Figure 5.12 and 5.13 shows the responses when the magnetization inductance L_m varies. It can be observed that when L_m varies from its nominal values L_m^* , both methods show transient fluctuations on the d-axis and q-axis currents. But the conventional PCC still

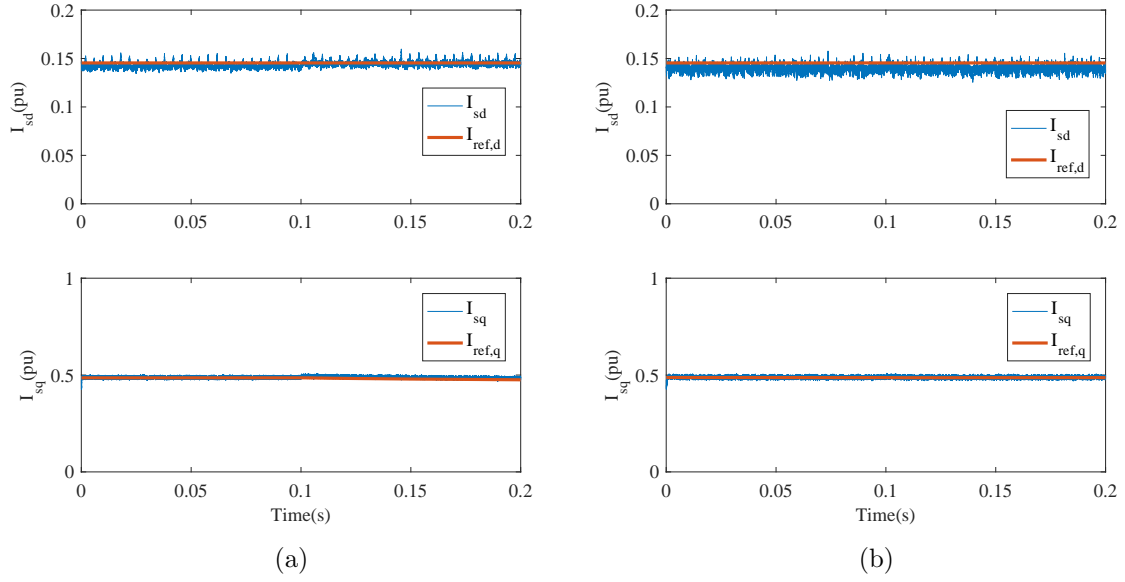


Figure 5.9: Steady-State Response with Disturbance $R_s = 0.5R_s^*$
 (a) Conventional Linear PCC
 (b) Proposed PCC-DO

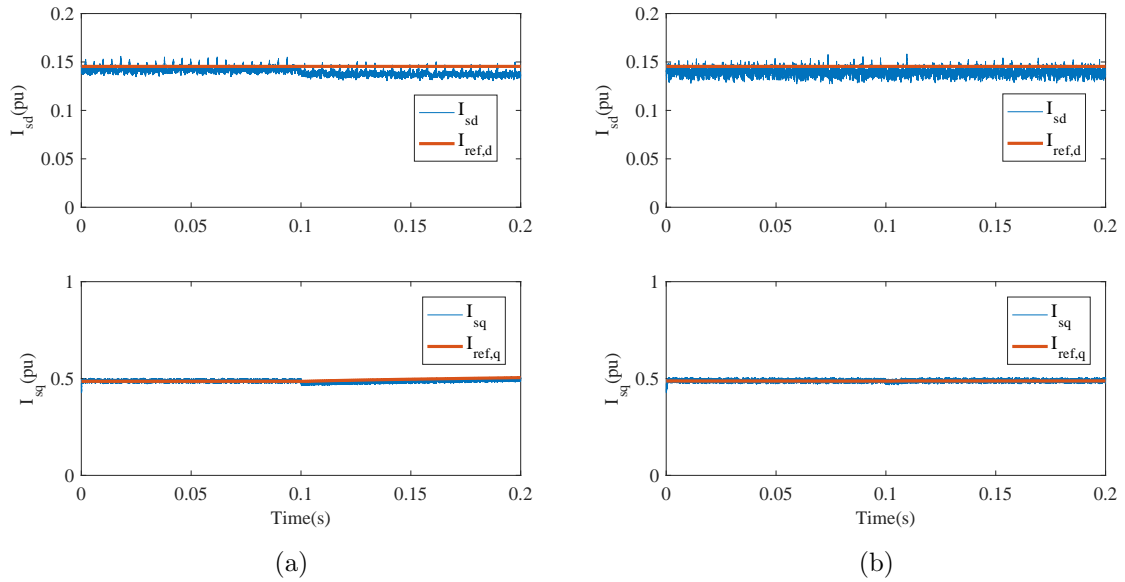


Figure 5.10: Steady-State Response with Disturbance $R_s = 2R_s^*$
 (a) Conventional Linear PCC
 (b) Proposed PCC-DO

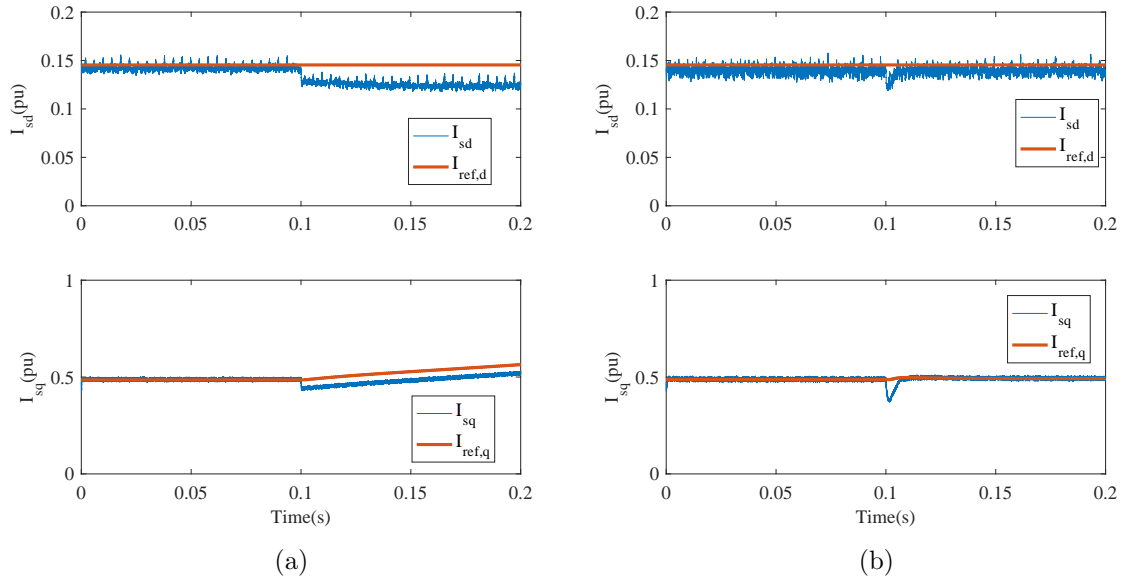


Figure 5.11: Steady-State Response with Disturbance $R_s = 5R_s^*$
 (a) Conventional Linear PCC
 (b) Proposed PCC-DO

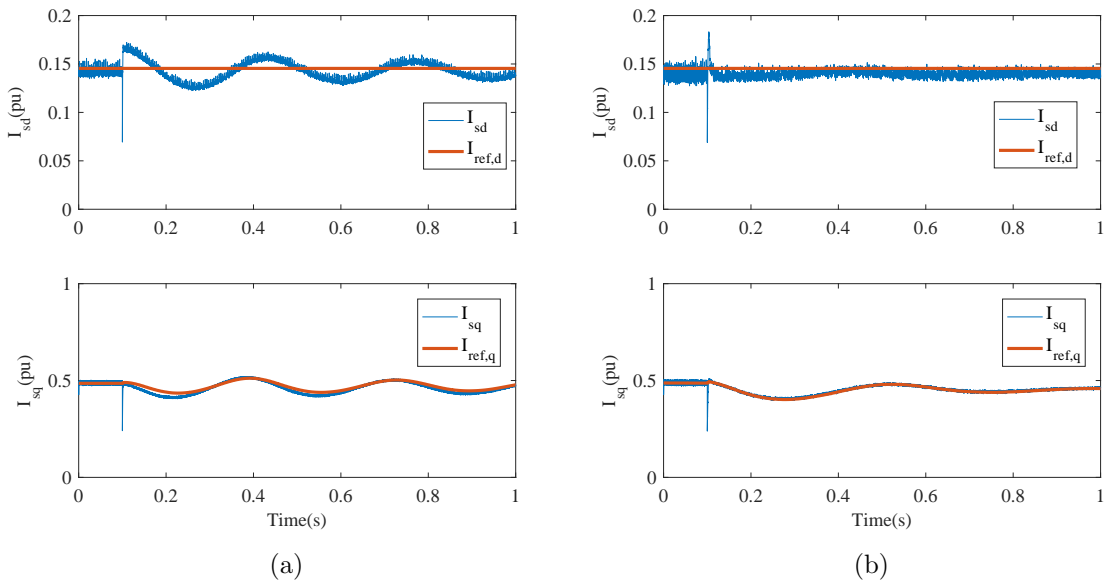


Figure 5.12: Steady-State Response with Disturbance $L_m = 0.5L_m^*$
 (a) Conventional Linear PCC
 (b) Proposed PCC-DO

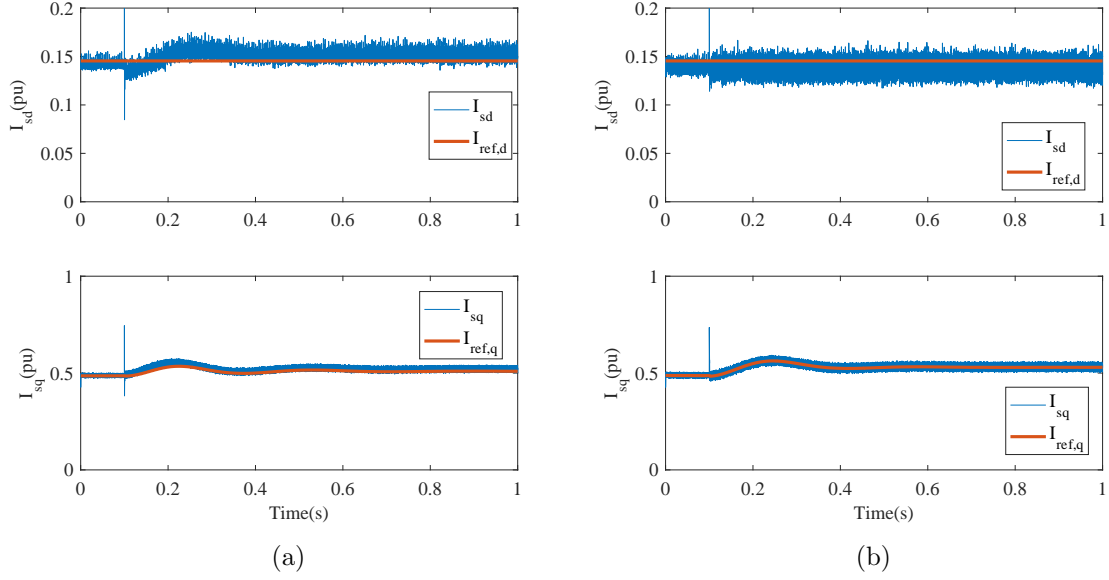


Figure 5.13: Steady-State Response with Disturbance $L_m = 1.5L_m^*$
(a) Conventional Linear PCC
(b) Proposed PCC-DO

present steady-state errors after the transients, while the proposed method can eliminate steady errors and precisely follow the reference d-axis and q-axis currents.

5.7.2 Transient State Performance

To verify the dynamic performance of proposed method, the motor is initialized at 0.2 pu speed (296 rpm) with no load, at time instant $t = 0.1s$, a 1.0 pu speed step command is given to the controller. Figure 5.14 shows the step response when no disturbances are added to the motor. From Figure 5.14 (a) and (b), it can be observed that both conventional PCC and proposed PCC-DO can provide precise dynamic responses.

Figure 5.15 to 5.18 show the transient responses under different parameter mismatches. Figure 5.15 and 5.16 show the dynamic responses under the stator resistance mismatch. When R_s changes, steady-state error occurs in conventional PCC, while proposed PCC-DO can still track the reference and eliminate the steady-state error. Figure 5.17 and 5.18 show

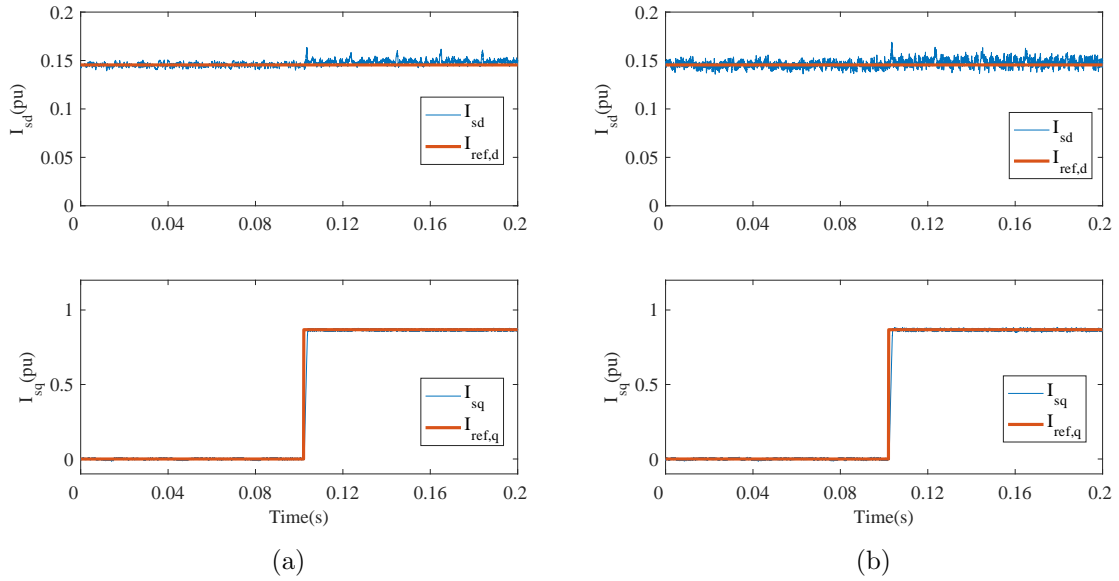


Figure 5.14: Transient Response with No Disturbance
 (a) Conventional Linear PCC
 (b) Proposed PCC-DO

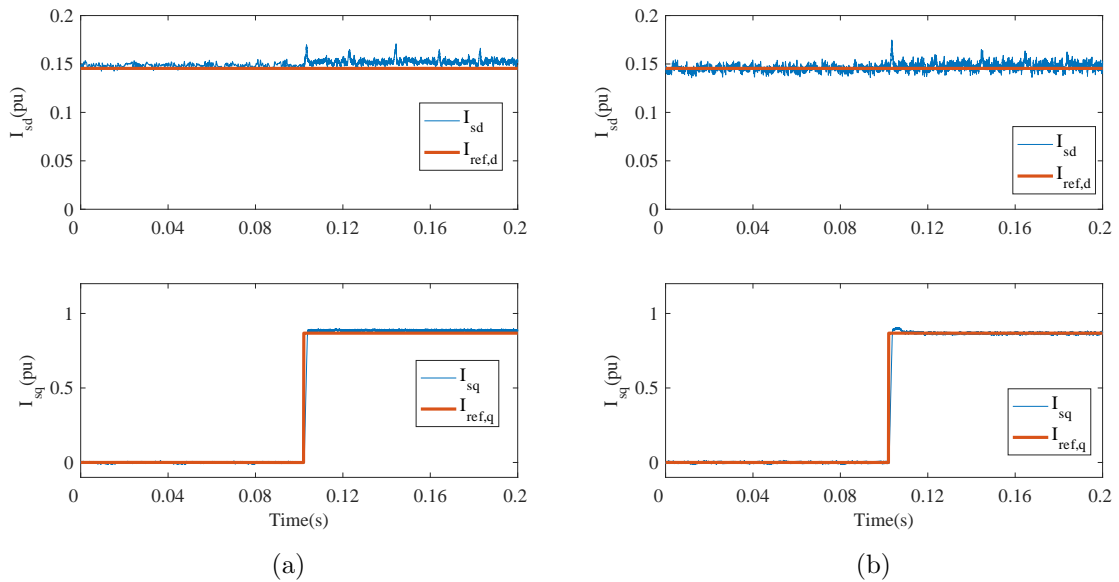


Figure 5.15: Transient Response with Disturbance $R_s = 0.1R_s^*$
 (a) Conventional Linear PCC
 (b) Proposed PCC-DO

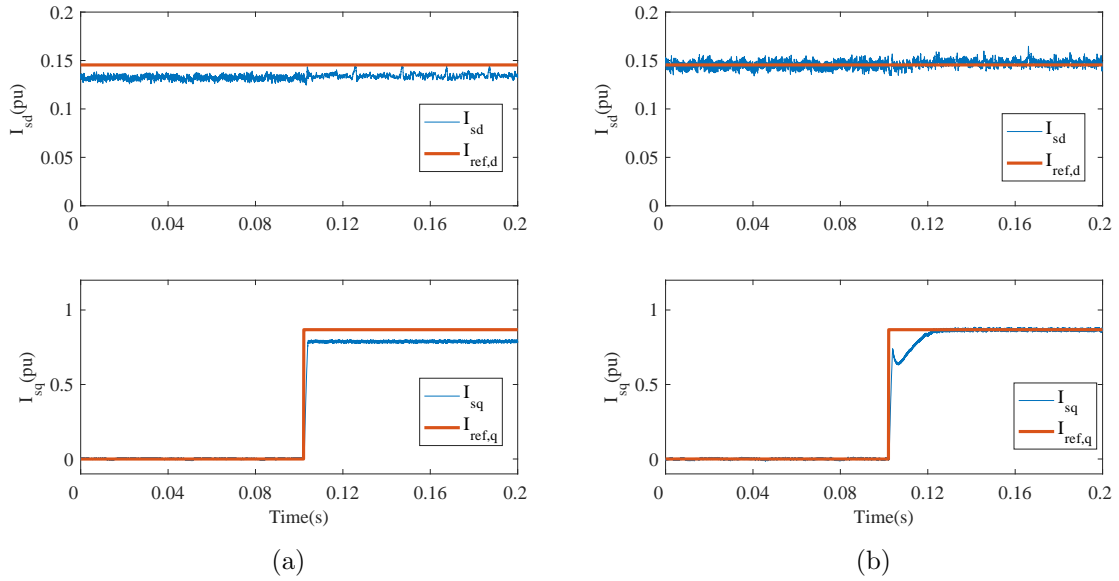


Figure 5.16: Transient Response with Disturbance $R_s = 10R_s^*$
 (a) Conventional Linear PCC
 (b) Proposed PCC-DO

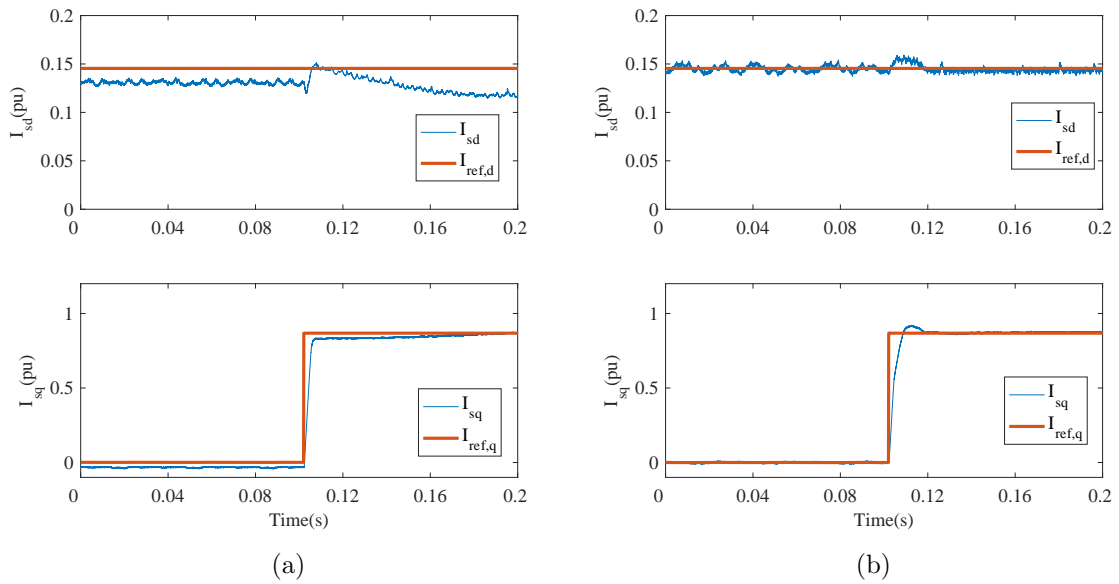


Figure 5.17: Transient Response with Disturbance $L_m = 0.5L_m^*$
 (a) Conventional Linear PCC
 (b) Proposed PCC-DO

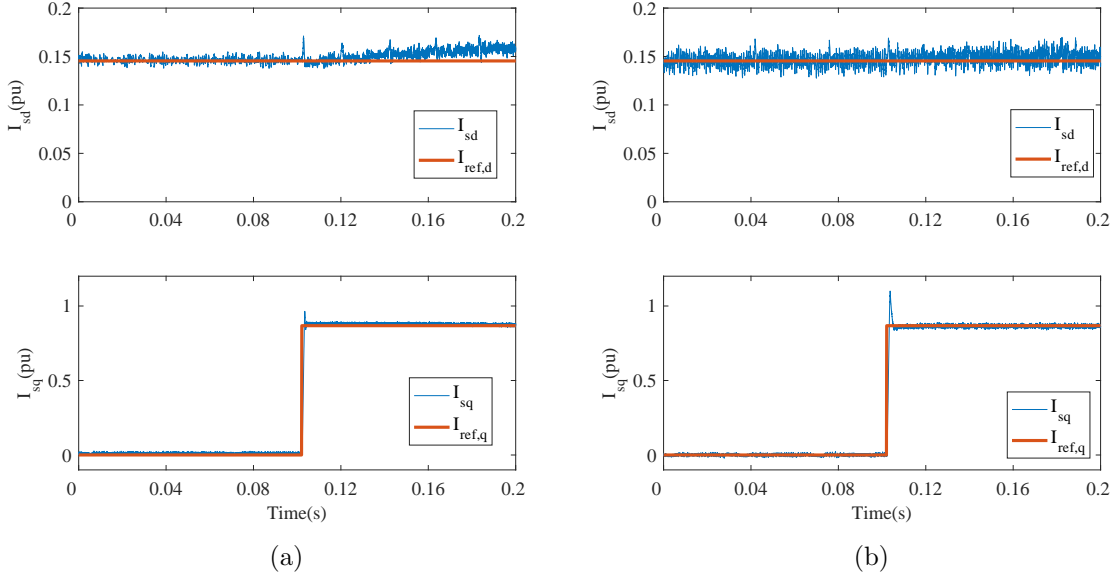


Figure 5.18: Transient Response with Disturbance $L_m = 1.5L_m^*$
(a) Conventional Linear PCC
(b) Proposed PCC-DO

the d-q axes current waveforms under L_m variances. When the motor is over-magnetized or under-magnetized, the proposed PCC-DO can compensate the disturbance and track the reference value, while conventional PCC present non-negligible errors against the reference values.

5.8 Summary

In this chapter, the parameter sensitivity of open-end winding induction motor is analyzed. Base on the analysis, a deadbeat predictive current control with disturbance observer (PCC-DO) is proposed. Simulation is done to verify the effectiveness of proposed method. During the steady state operation, the proposed method can effectively respond to sudden parameter changes, and eliminate the resultant steady state error. During the transient operations, the proposed methods are tested under different parameter mismatch circumstances. The

simulation results show that the proposed method can correctly compensate the disturbances introduced by stator resistance and magnetization inductance variances.

CHAPTER 6

CONCLUSIONS AND RECOMMENDATIONS FOR FUTURE WORK

In automotive testing system, fast current/torque response is required to provide accurate emulation of combustion engine and to minimize the measurement errors. Model predictive control is ideal for the electrical drives used in automotive testing system due to its intuitive concept, fast dynamic response, and excellent inclusion of system constraints and non-linearities. Successful commercialization of medium voltage drives has been reported. However, MPC has not yet been applied on open-end winding induction motor drives. Also, problems of MPC such as heavy computation burden and parameter sensitivity still remain to be solved. In this dissertation, a comprehensive study of fast response model predictive control methods for open-end winding induction motor drive is established. Considering the above problems with conventional MPC, new control algorithms are proposed, implemented and verified.

6.1 Contributions of the Work

The key contributions of this dissertation are summarized as follow:

- For open-end winding induction motor drive, four fast response model predictive control methods, i.e., linear predictive current control (LPCC), non-linear predictive current control (NLPC), linear predictive torque control (LPTC), and non-linear predictive torque control (NLPTC) are proposed. The four proposed methods are verified in simulation and experiments. The results show that compared with conventional PI control method, the proposed methods have higher controller bandwidth as well as stronger zero-sequence current suppression.
- Considering the heavy computation burden in conventional MPC methods, two computationally efficient MPC methods are proposed, i.e., predictive current control in A-B-C

frame (PCC-ABC) and three-dimensional predictive current trajectory control (3DPCTC). Compared with conventional methods, the proposed strategies reduce the calculation time by 61.05% and 64.24% respectively. Meanwhile, fast dynamic response is maintained, and the zero-sequence current is suppressed.

- For the parameter sensitivity issue in MPC methods, a deadbeat predictive current control with disturbance observer (PCC-DO) is proposed. Different tests have been executed to examine the performances of the motor in steady state and transient state. The results show that the proposed method can compensate the parameter mismatches, eliminate steady-state errors, as well as maintaining fast dynamic responses.

6.2 Recommendations for Future Work

This dissertation studies the open-end winding induction motor drive with two 2L-VSI sharing the same DC-link. Multiple model-predictive control methods are proposed to provide fast dynamic response, to suppress the zero-sequence current, to reduce computation burden, and to provide better immunity to parameter mismatches and disturbances. The work in this dissertation provides a physical insight of applying MPC to electrical systems with more than one converter and with multiple voltage levels. Due to the presence of zero-sequence current, this dissertation also presents a practical way of employing MPC on unbalanced systems. Taking these into consideration, the work illustrated in this dissertation can lay the basis for the following research work, which could be addressed in the future.

- Computationally-efficient model predictive control methods for multi-level converters.
- Model predictive control methods for different open-end winding topologies, such as OEWIM fed by 2L-VSI and diode bridges.
- Model predictive control for unbalanced systems.

REFERENCES

- [1] Jyotindra S Killedar. *Dynamometer: theory and application to engine testing*. Xlibris Corporation, 2012.
- [2] S Figarado, K Sivakumar, R Ramchand, A Das, C Patel, and K Gopakumar. Five-level inverter scheme for an open-end winding induction machine with less number of switches. *IET Power Electronics*, 3(4):637–647, 2010.
- [3] Gopal Mondal, Krishnamoorthy Sivakumar, Rijil Ramchand, K Gopakumar, and Emil Levi. A dual seven-level inverter supply for an open-end winding induction motor drive. *IEEE Transactions on Industrial Electronics*, 56(5):1665–1673, 2009.
- [4] PP Rajeevan, K Sivakumar, K Gopakumar, Chintan Patel, and Haitham Abu-Rub. A nine-level inverter topology for medium-voltage induction motor drive with open-end stator winding. *IEEE transactions on industrial electronics*, 60(9):3627–3636, 2013.
- [5] Makoto Hagiwara and Hirofumi Akagi. Control and experiment of pulsewidth-modulated modular multilevel converters. *IEEE Transactions on Power Electronics*, 24(7):1737–1746, 2009.
- [6] Hirofumi Akagi. Classification, terminology, and application of the modular multilevel cascade converter (mmcc). *IEEE Transactions on Power Electronics*, 26(11):3119–3130, 2011.
- [7] Jun Mei, Bailu Xiao, Ke Shen, Leon M Tolbert, and Jian Yong Zheng. Modular multilevel inverter with new modulation method and its application to photovoltaic grid-connected generator. *IEEE Transactions on Power Electronics*, 28(11):5063–5073, 2013.
- [8] Yifeng Wu, Matt Jacob-Mitos, Marcia L Moore, and Sten Heikman. A 97.8% efficient gan hemt boost converter with 300-w output power at 1 mhz. *IEEE Electron Device Letters*, 29(8):824–826, 2008.
- [9] Juergen Biela, Mario Schweizer, Stefan Waffler, and Johann W Kolar. Sic versus sievaluation of potentials for performance improvement of inverter and dc–dc converter systems by sic power semiconductors. *IEEE transactions on industrial electronics*, 58(7):2872–2882, 2011.
- [10] Jose Millan, Philippe Godignon, Xavier Perpina, Amador Pérez-Tomás, and José Rebollo. A survey of wide bandgap power semiconductor devices. *IEEE transactions on Power Electronics*, 29(5):2155–2163, 2014.
- [11] Xiucheng Huang, Zhengyang Liu, Qiang Li, and Fred C Lee. Evaluation and application of 600 v gan hemt in cascode structure. *IEEE Transactions on Power Electronics*, 29(5):2453–2461, 2014.

- [12] Radoslava Mitova, Rajesh Ghosh, Uday Mhaskar, Damir Klikic, Miao-Xin Wang, and Alain Dentella. Investigations of 600-v gan hemt and gan diode for power converter applications. *IEEE Transactions on Power Electronics*, 29(5):2441–2452, 2014.
- [13] Zhen-Yu Zhao, Masayoshi Tomizuka, and Satoru Isaka. Fuzzy gain scheduling of pid controllers. *IEEE transactions on systems, man, and cybernetics*, 23(5):1392–1398, 1993.
- [14] Jawad Talaq and Fadel Al-Basri. Adaptive fuzzy gain scheduling for load frequency control. *IEEE Transactions on power systems*, 14(1):145–150, 1999.
- [15] Yodyium Tipsuwan and Mo-Yuen Chow. On the gain scheduling for networked pi controller over ip network. *IEEE/ASME Transactions On Mechatronics*, 9(3):491–498, 2004.
- [16] Isao Takahashi and Toshihiko Noguchi. A new quick-response and high-efficiency control strategy of an induction motor. *IEEE Transactions on Industry applications*, (5):820–827, 1986.
- [17] Bimal K Bose. An adaptive hysteresis-band current control technique of a voltage-fed pwm inverter for machine drive system. *IEEE Transactions on industrial electronics*, 37(5):402–408, 1990.
- [18] Gilberto CD Sousa, Bimal K Bose, and John G Cleland. Fuzzy logic based on-line efficiency optimization control of an indirect vector-controlled induction motor drive. *IEEE Transactions on Industrial Electronics*, 42(2):192–198, 1995.
- [19] Faa-Jeng Lin, Chih-Hong Lin, and Po-Hung Shen. Self-constructing fuzzy neural network speed controller for permanent-magnet synchronous motor drive. *IEEE transactions on fuzzy systems*, 9(5):751–759, 2001.
- [20] Shady M Gadoue, Damian Giaouris, and John W Finch. Mras sensorless vector control of an induction motor using new sliding-mode and fuzzy-logic adaptation mechanisms. *IEEE Transactions on Energy Conversion*, 25(2):394–402, 2010.
- [21] K.S.Rajashekara and J.Vithayathil. Microcomputer based symmetrical sinusoidal pulse width modulated inverter. In *IEEE IECI Proceedings*, 1981.
- [22] K.S. Rajashekara and V. Rajagopalan. Simulation of sspwm inverter-fed induction motor. In *International Symposium on Modeling and Simulation of Electrical Machines, Converters and Power Systems*, 1987.
- [23] E.G. Shivakumar, K. Gopakumar, S.K. Sinha, A. Pittet, and V.T. Ranganathan. Space vector pwm control of dual inverter fed open-end winding induction motor drive. In *Applied Power Electronics Conference and Exposition (APEC)*, 2001.

- [24] MR Baiju, KK Mohapatra, RS Kanchan, and K Gopakumar. A dual two-level inverter scheme with common mode voltage elimination for an induction motor drive. *IEEE Transactions on Power Electronics*, 19(3):794–805, 2004.
- [25] VT Somasekhar, K Gopakumar, and MR Baiju. Dual two-level inverter scheme for an open-end winding induction motor drive with a single dc power supply and improved dc bus utilisation. *IEE Proceedings-Electric Power Applications*, 151(2):230–238, 2004.
- [26] Jose Rodriguez and Patricio Cortes. *Predictive control of power converters and electrical drives*, volume 40. John Wiley & Sons, 2012.
- [27] Karel Jezernik, Jože Korelič, and Robert Horvat. Pmsm sliding mode fpga-based control for torque ripple reduction. *IEEE Transactions on Power Electronics*, 28(7):3549–3556, 2013.
- [28] Yasser Abdel-Rady Ibrahim Mohamed and Ehab F El-Saadany. An improved deadbeat current control scheme with a novel adaptive self-tuning load model for a three-phase pwm voltage-source inverter. *IEEE Transactions on Industrial Electronics*, 54(2):747–759, 2007.
- [29] Timothy R Obermann, Zachary D Hurst, and Robert D Lorenz. Deadbeat-direct torque & flux control motor drive over a wide speed, torque and flux operating space using a single control law. In *Energy Conversion Congress and Exposition (ECCE), 2010 IEEE*, pages 215–222. IEEE, 2010.
- [30] Sergio Vazquez, Jose I Leon, Leopoldo G Franquelo, Jose Rodriguez, Hector A Young, Abraham Marquez, and Pericle Zanchetta. Model predictive control: A review of its applications in power electronics. *IEEE Industrial Electronics Magazine*, 8(1):16–31, 2014.
- [31] Carlos E Garcia, David M Prett, and Manfred Morari. Model predictive control: theory and practice survey. *Automatica*, 25(3):335–348, 1989.
- [32] J Holtz. A predictive controller for the stator current vector of ac machines fed from a switched voltage source. *Proc. of IEE of Japan IPEC-Tokyo’83*, pages 1665–1675, 1983.
- [33] Eduardo F Camacho and Carlos Bordons. *Model Predictive Control*. Springer, 1999.
- [34] Tobias Geyer and Daniel E Quevedo. Multistep direct model predictive control for power electronics part 1: Algorithm. In *Energy Conversion Congress and Exposition (ECCE), 2013 IEEE*, pages 1154–1161. IEEE, 2013.
- [35] PETrOS KaraMaNaKOS, Tobias Geyer, Nikolaos Oikonomou, FrEDErIcK D KIEFErN-DOrF, and STEFaNOS MaNIaS. Direct model predictive control: A review of strategies that achieve long prediction intervals for power electronics. *IEEE Industrial Electronics Magazine*, 8(1):32–43, 2014.

- [36] Tobias Geyer and Daniel E Quevedo. Multistep direct model predictive control for power electronics part 2: Analysis. In *Energy Conversion Congress and Exposition (ECCE), 2013 IEEE*, pages 1162–1169. IEEE, 2013.
- [37] Tobias Geyer. Model predictive direct current control: Formulation of the stator current bounds and the concept of the switching horizon. *IEEE Industry Applications Magazine*, 18(2):47–59, 2012.
- [38] R.K. Gupta, A. Somani, K.K. Mohapatra, and N. Mohan. Space vector pwm for a direct matrix converter based open-end winding ac drives with enhanced capabilities. In *Applied Power Electronics Conference and Exposition (APEC)*, 2010.
- [39] H. Stemmler and P. Guggenbach. Configurations of high-power voltage source inverter drives. In *Proceedings of European Power Electronics Application Conference*, 1993.
- [40] A. Somani, R.K. Gupta, K.K. Mohapatra, Kaushik Basu, and N. Mohan. Modulation strategies for direct-link drive for open-end winding ac machines. In *Electric Machines and Drives Conference 2009*, 2009.
- [41] Yang Wang, Debiprasad Panda, Thomas A Lipo, and Di Pan. Open-winding power conversion systems fed by half-controlled converters. *IEEE Transactions on Power Electronics*, 28(5):2427–2436, 2013.
- [42] K Gopakumar, VT Ranganathan, and SR Bhat. Split-phase induction motor operation from pwm voltage source inverter. *IEEE Transactions on Industry Applications*, 29(5): 927–932, 1993.
- [43] Emil Levi, Nandor Bodo, Obrad Dordevic, and Martin Jones. Recent advances in power electronic converter control for multiphase drive systems. In *Electrical Machines Design Control and Diagnosis (WEMDCD), 2013 IEEE Workshop on*, pages 158–167. IEEE, 2013.
- [44] T.A. Lipo. New open winding machine concepts, 2013.
- [45] Patricio Cortes, Jose Rodriguez, Cesar Silva, and Alexis Flores. Delay compensation in model predictive current control of a three-phase inverter. *IEEE Transactions on Industrial Electronics*, 59(2):1323–1325, 2012.
- [46] Hernán Miranda, Patricio Cortés, Juan I Yuz, and José Rodríguez. Predictive torque control of induction machines based on state-space models. *IEEE Transactions on Industrial Electronics*, 56(6):1916–1924, 2009.
- [47] Patricio Cortés, Gabriel Ortiz, Juan I Yuz, José Rodríguez, Sergio Vazquez, and Leopoldo G Franquelo. Model predictive control of an inverter with output lc filter for ups applications. *IEEE Transactions on Industrial Electronics*, 56(6):1875–1883, 2009.

- [48] Patricio Cortés, José Rodríguez, Daniel E Quevedo, and Cesar Silva. Predictive current control strategy with imposed load current spectrum. *IEEE Transactions on Power Electronics*, 23(2):612–618, 2008.
- [49] Patricio Cortes, José Rodriguez, Patrycjusz Antoniewicz, and Marian Kazmierkowski. Direct power control of an afe using predictive control. *IEEE Transactions on Power Electronics*, 23(5):2516–2523, 2008.
- [50] MR Arahal, F Barrero, S Toral, M Duran, and R Gregor. Multi-phase current control using finite-state model-predictive control. *Control Engineering Practice*, 17(5):579–587, 2009.
- [51] Bohang Zhu, Kaushik Rajashekara, and Hajime Kubo. Predictive torque control with zero-sequence current suppression for open-end winding induction machine. In *Industry Applications Society Annual Meeting, 2015 IEEE*, pages 1–7. IEEE, 2015.
- [52] Bohang Zhu, Kaushik Rajashekara, and Hajime Kubo. A comparison between current based and flux/torque based model predictive control methods for open-end winding induction motor drives. *IET Electric Power Applications*, 2017.
- [53] Hajime Kubo, Yasuhiro Yamamoto, Takeshi Kondo, Kaushik Rajashekara, and Bohang Zhu. High bandwidth current control for open-end winding induction motor. In *Industrial Electronics Society, IECON 2014-40th Annual Conference of the IEEE*, pages 607–613. IEEE, 2014.
- [54] René Vargas, José Rodríguez, Ulrich Ammann, and Patrick W Wheeler. Predictive current control of an induction machine fed by a matrix converter with reactive power control. *IEEE Transactions on Industrial Electronics*, 55(12):4362–4371, 2008.
- [55] Jos Rodriguez, Jorge Pontt, Csar A Silva, Pablo Correa, Pablo Lezana, Patricio Cortés, and Ulrich Ammann. Predictive current control of a voltage source inverter. *IEEE Transactions on Industrial Electronics*, 54(1):495–503, 2007.
- [56] Federico Barrero, Joel Prieto, Emil Levi, Raúl Gregor, Sergio Toral, Mario J Durán, and Martin Jones. An enhanced predictive current control method for asymmetrical six-phase motor drives. *IEEE Transactions on Industrial Electronics*, 58(8):3242–3252, 2011.
- [57] Chee Shen Lim, Nasrudin Abd Rahim, Wooi Ping Hew, and Emil Levi. Model predictive control of a two-motor drive with five-leg-inverter supply. *IEEE Transactions on Industrial Electronics*, 60(1):54–65, 2013.
- [58] Barbara H Kenny and Robert D Lorenz. Stator and rotor flux based deadbeat direct torque control of induction machines. *IEEE Transactions on Industry Applications*, 39(4):1093–1101, July 2003.

- [59] Nathan T West and Robert D Lorenz. Digital implementation of stator and rotor flux-linkage observers and a stator-current observer for deadbeat direct torque control of induction machines. *IEEE Transactions on Industry Applications*, 45(2):729–736, 2009.
- [60] Jae Suk Lee and Robert D Lorenz. Deadbeat direct torque and flux control of ipmsm drives using a minimum time ramp trajectory method at voltage and current limits. *IEEE Transactions on Industry Applications*, 50(6):3795–3804, 2014.
- [61] Rene Vargas, Jose Rodriguez, Christian A Rojas, and Marco Rivera. Predictive control of an induction machine fed by a matrix converter with increased efficiency and reduced common-mode voltage. *IEEE Transactions on Energy Conversion*, 29(2):473–485, 2014.
- [62] Jose Rodriguez, Patricio Cortes, Ralph Kennel, and Marian P Kazmierkowski. Model predictive control—a simple and powerful method to control power converters. In *Power Electronics and Motion Control Conference, 2009. IPEMC'09. IEEE 6th International*, pages 41–49. IEEE, 2009.
- [63] Christian A Rojas, Jose Rodriguez, Felipe Villarroel, José R Espinoza, César A Silva, and Mauricio Trincado. Predictive torque and flux control without weighting factors. *IEEE Transactions on Industrial Electronics*, 60(2):681–690, 2013.
- [64] Fengxiang Wang, Shihua Li, Xuezhu Mei, Wei Xie, José Rodríguez, and Ralph M Kennel. Model-based predictive direct control strategies for electrical drives: An experimental evaluation of ptc and pcc methods. *IEEE Transactions on Industrial Informatics*, 11(3):671–681, 2015.
- [65] Tobias Geyer, Georgios Papafotiou, and Manfred Morari. Model predictive direct torque control part i: Concept, algorithm, and analysis. *IEEE Transactions on Industrial Electronics*, 56(6):1894–1905, 2009.
- [66] Baljit S Riar, Tobias Geyer, and Udaya K Madawala. Model predictive direct current control of modular multilevel converters: Modeling, analysis, and experimental evaluation. *IEEE Transactions on Power Electronics*, 30(1):431–439, 2015.
- [67] Tobias Geyer, Nikolaos Oikonomou, Georgios Papafotiou, and Frederick D Kieferndorf. Model predictive pulse pattern control. *IEEE Transactions on Industry Applications*, 48(2):663–676, 2012.
- [68] Bohang Zhu, Kaushik Rajashekara, and Hajime Kubo. A novel predictive current control for open-end winding induction motor drive with reduced computation burden and enhanced zero sequence current suppression. In *Applied Power Electronics Conference and Exposition (APEC), 2017 IEEE*, pages 552–557. IEEE, 2017.
- [69] Bohang Zhu and Kaushik Rajashekara. A three-dimensional predictive current trajectory control method for open-end winding induction motor. In *Energy Conversion Congress and Exposition (ECCE), 2017 ECCE*, 2017.

- [70] Giuseppe S Buja and Marian P Kazmierkowski. Direct torque control of pwm inverter-fed ac motors-a survey. *IEEE Transactions on industrial electronics*, 51(4):744–757, 2004.
- [71] KH John Chong and R-D Klug. High power medium voltage drives. In *Power System Technology, 2004. PowerCon 2004. 2004 International Conference on*, volume 1, pages 658–664. IEEE, 2004.
- [72] Tobias Geyer. Computationally efficient model predictive direct torque control. *IEEE Transactions on Power Electronics*, 26(10):2804–2816, 2011.
- [73] Zhixun Ma, Saeid Saeidi, and Ralph Kennel. Fpga implementation of model predictive control with constant switching frequency for pmsm drives. *IEEE Transactions on Industrial Informatics*, 10(4):2055–2063, 2014.
- [74] Zhenbin Zhang, Fengxiang Wang, Tongjing Sun, Jose Rodriguez, and Ralph Kennel. Fpga-based experimental investigation of a quasi-centralized model predictive control for back-to-back converters. *IEEE Transactions on Power Electronics*, 31(1):662–674, 2016.
- [75] Fang Xu, Hong Chen, Xun Gong, and Qin Mei. Fast nonlinear model predictive control on fpga using particle swarm optimization. *IEEE Transactions on Industrial Electronics*, 63(1):310–321, 2016.
- [76] Tobias Geyer. A comparison of control and modulation schemes for medium-voltage drives: Emerging predictive control concepts versus pwm-based schemes. *IEEE Transactions on Industry Applications*, 47(3):1380–1389, 2011.
- [77] Georgios Papafotiou, Jonas Kley, Kostas G Papadopoulos, Patrick Bohren, and Manfred Morari. Model predictive direct torque control part ii: Implementation and experimental evaluation. *IEEE Transactions on Industrial Electronics*, 56(6):1906–1915, 2009.
- [78] Yalin Zhang and Hua Lin. Simplified model predictive current control method of voltage-source inverter. In *Power Electronics and ECCE Asia (ICPE & ECCE), 2011 IEEE 8th International Conference on*, pages 1726–1733. IEEE, 2011.
- [79] Atif Iqbal, Haitham Abu-Rub, SK Moin Ahmed, Patricio Cortes, and Jose Rodriguez. Model predictive current control of a three-level five-phase npc vsi using simplified computational approach. In *Applied Power Electronics Conference and Exposition (APEC), 2014 Twenty-Ninth Annual IEEE*, pages 2323–2330. IEEE, 2014.
- [80] Yongchang Zhang and Wei Xie. Low complexity model predictive control single vector-based approach. *IEEE Transactions on Power Electronics*, 29(10):5532–5541, 2014.

- [81] Yongchang Zhang, Wei Xie, Zhengxi Li, and Yingchao Zhang. Low-complexity model predictive power control: Double-vector-based approach. *IEEE Transactions on Industrial Electronics*, 61(11):5871–5880, 2014.
- [82] Jiefeng Hu, Jianguo Zhu, Gang Lei, Glenn Platt, and David G Dorrell. Multi-objective model-predictive control for high-power converters. *IEEE Transactions on energy conversion*, 28(3):652–663, 2013.
- [83] Changliang Xia, Tao Liu, Tingna Shi, and Zhanfeng Song. A simplified finite-control-set model-predictive control for power converters. *IEEE Transactions on Industrial Informatics*, 10(2):991–1002, 2014.
- [84] Wei Xie, Xiaocan Wang, Fengxiang Wang, Wei Xu, Ralph M Kennel, Dieter Gerling, and Robert D Lorenz. Finite-control-set model predictive torque control with a deadbeat solution for pmsm drives. *IEEE Transactions on Industrial Electronics*, 62(9):5402–5410, 2015.
- [85] Md Habibullah, Dylan Dah-Chuan Lu, Dan Xiao, and Muhammed Fazlur Rahman. A simplified finite-state predictive direct torque control for induction motor drive. *IEEE Transactions on Industrial Electronics*, 63(6):3964–3975, 2016.
- [86] Haitao Yang, Yongchang Zhang, Paul D Walker, Jiejunyi Liang, Nong Zhang, and Bo Xia. Speed sensorless model predictive current control with ability to start a free running induction motor. *IET Electric Power Applications*, 11(5):893–901, 2017.
- [87] So-young Park and Sangshin Kwak. Comparative study of three model predictive current control methods with two vectors for three-phase dc/ac vsis. *IET Electric Power Applications*, 2017.
- [88] Yongchang Zhang, Donglin Xu, Jiali Liu, Suyu Gao, and Wei Xu. Performance improvement of model predictive current control of permanent magnet synchronous motor drives. *IEEE Transactions on Industry Applications*, 2017.
- [89] Tobias Geyer. *Low complexity model predictive control in power electronics and power systems*. Cuvillier Verlag, 2005.
- [90] P Wipasuramonton, ZQ Zhu, and David Howe. Predictive current control with current-error correction for pm brushless ac drives. *IEEE Transactions on Industry Applications*, 42(4):1071–1079, 2006.
- [91] Niu Li, Yang Ming, and Xu Dianguo. An adaptive robust predictive current control for pmsm with online inductance identification. *International Review of Electrical Engineering*, 7(2), 2012.

- [92] Hoang Le-Huy, Karim Slimani, and Philippe Viarouge. Analysis and implementation of a real-time predictive current controller for permanent-magnet synchronous servo drives. *IEEE Transactions on Industrial Electronics*, 41(1):110–117, 1994.
- [93] W-H Chen, Donald J Ballance, Peter J Gawthrop, Jenny J Gribble, and John O’Reilly. Nonlinear pid predictive controller. *IEE Proceedings-Control Theory and Applications*, 146(6):603–611, 1999.
- [94] Jun Yang, Wei Xing Zheng, Shihua Li, Bin Wu, and Ming Cheng. Design of a prediction-accuracy-enhanced continuous-time mpc for disturbed systems via a disturbance observer. *IEEE Transactions on Industrial Electronics*, 62(9):5807–5816, 2015.
- [95] Jun Yang, Shihua Li, and Xinghuo Yu. Sliding-mode control for systems with mismatched uncertainties via a disturbance observer. *IEEE Transactions on Industrial Electronics*, 60(1):160–169, 2013.
- [96] Jun Yang and Wei Xing Zheng. Offset-free nonlinear mpc for mismatched disturbance attenuation with application to a static var compensator. *IEEE Transactions on Circuits and Systems II: Express Briefs*, 61(1):49–53, 2014.
- [97] Jun Yang, Jinya Su, Shihua Li, and Xinghuo Yu. High-order mismatched disturbance compensation for motion control systems via a continuous dynamic sliding-mode approach. *IEEE Transactions on Industrial Informatics*, 10(1):604–614, 2014.
- [98] Xiaoguang Zhang, Benshuai Hou, and Yang Mei. Deadbeat predictive current control of permanent-magnet synchronous motors with stator current and disturbance observer. *IEEE Transactions on Power Electronics*, 32(5):3818–3834, 2017.
- [99] R Krishnan and Frank C Doran. Study of parameter sensitivity in high-performance inverter-fed induction motor drive systems. *IEEE Transactions on Industry Applications*, (4):623–635, 1987.

BIOGRAPHICAL SKETCH

Bohang Zhu received his BS degree in Electrical Engineering and Automation from Wuhan University, Wuhan, China P. R. in 2012 and his MS degree in Electrical Engineering from The University of Texas at Dallas, Richardson in 2014. He worked as an Research Assistant in the Power Electronics and Drives Lab from 2013 to 2014. He is currently pursuing his PhD degree at The University of Texas at Dallas. His research interests include model predictive control for open-end winding induction motors and PWM strategies for multi-level converters.

CURRICULUM VITAE

Bohang Zhu

October 15, 2017

Contact Information:

Department of Electrical Engineering
The University of Texas at Dallas
800 W. Campbell Rd.
Richardson, TX 75080-3021, U.S.A.

Voice: (972) 375-8757
Email: Bohang.Zhu@utdallas.edu

Educational History:

B.S., Electrical Engineering and Automation, Wuhan University, 2012
M.S., Electrical Engineering, The University of Texas at Dallas, 2014
Ph.D., Electrical Engineering, The University of Texas at Dallas, 2017

Fast Response Model Predictive Control for Open-End Winding Induction Motors
Ph.D. Dissertation

Electrical Engineering Department, The University of Texas at Dallas
Advisor: Dr. Kaushik Rajashekara

PWM Strategies for Open-End Winding Induction Motor Drives
Master Thesis

Electrical Engineering Department, The University of Texas at Dallas
Advisor: Dr. Kaushik Rajashekara

Employment History:

Teaching/Research Assistant, The University of Texas at Dallas, September 2013 – present

Professional Memberships:

Institute of Electrical and Electronics Engineers (IEEE), 2014–present